Absorption of Solar Radiation by Heterogeneous Atmospheres: A New Approach to Monte Carlo Modeling

By
Philip T. Partain and Graeme L. Stephens

Department of Atmospheric Science
Colorado State University
Fort Collins, Colorado

Research supported by Department of Energy contracts #DE-FG-03-94ER61748, DE-FG-03-95ER61985 and DE-FG-03-97ER62357
PI: G. Stephens

Colorado State University

Department of Atmospheric Science

Paper No. 648

ABSORPTION OF SOLAR RADIATION BY HETEROGENEOUS ATMOSPHERES: A NEW APPROACH TO MONTE CARLO MODELING

Philip T. Partain and Graeme L. Stephens

Research supported by Department of Energy contracts #DE-FG-03-94ER61748 , #DE-FG-03-95ER61985 , and #DE-FG-03-97ER62357

Principal Investigator: Graeme L. Stephens

Department of Atmospheric Science

Colorado State University

Fort Collins, Colorado

February, 1998

Atmospheric Science Paper No.

ABSORPTION OF SOLAR RADIATION BY HETEROGENEOUS ATMOSPHERES: A NEW APPROACH TO MONTE CARLO MODELING

Philip T. Partain and Graeme L. Stephens

Research supported by Department of Energy contracts #DE-FG-03-94ER61748 , #DE-FG-03-95ER61985 , and #DE-FG-03-97ER62357

Principal Investigator: Graeme L. Stephens

Department of Atmospheric Science

Colorado State University

Fort Collins, Colorado

February, 1998

Atmospheric Science Paper No. 648

ABSTRACT OF THESIS

ABSORPTION OF SOLAR RADIATION BY HETEROGENEOUS ATMOSPHERES: A NEW APPROACH TO MONTE CARLO MODELING

The debate involving the observation of solar radiation absorption in the atmosphere in excess of model prediction has plagued the atmospheric science community for over forty years. If true, this discrepancy has major implications on our understanding of solar radiative transfer, remote sensing, atmospheric dynamics, and global climate. Past comparisons between theory and observations of atmospheric absorption have primarily shown results ranging from model underestimation of absorption to good agreement, however model overestimation has also been presented.

To reconcile the magnitude and cause of the absorption discrepancy, the Department of Energy Atmospheric Radiation Measurement (ARM) Program implemented the ARM Enhanced Shortwave Experiment (ARESE) in northern Oklahoma. Recent results from this experiment published by Zender et al. (1997) and Valero et al. (1997) report not only that absorption in the atmosphere is in excess of model prediction, but is larger than indicated by the studies which first introduced the problem.

Throughout the literature, many possible causes for this discrepancy have been proposed. These include, (1) instrument error or inadequate measurement technique, (2) inaccurate specification of the observed atmosphere in radiative transfer models, (3) inaccurate absorption theory for aerosol, gas, or cloud, and (4) the unresolved effect of cloud heterogeneity. Of all possible causes, the least well understood is the effect of cloud heterogeneity. This study investigated the effect of cloud heterogeneity on gas and cloud absorption of solar radiation. This was accomplished with a three-dimensional, broadband

Monte Carlo model with 287 spectral bands. The theory behind this high resolution model was derived from the Equivalence Theorem as introduced by Irvine (1964) and represents a new and major advancement in the power and utility of the Monte Carlo method.

Results from experiments showed that, for the cloud situations modeled, the effect of cloud heterogeneity on absorption is too small to explain ARESE observations but could be important for applications such as general circulation modeling where cloud fields are assumed to be plane-parallel. Two ARESE cases are revisited to try and determine the nature of the observed excess absorption. Using spectral simulations from the Monte Carlo model and what was learned from the cloud heterogeneity experiments, it was discovered that an inconsistency exists between the broadband and spectral instruments used to measure radiative fluxes. Using the spectral instruments in conjunction with model results decreased the absorption discrepancy between theory and observations from 16% to 5% on the overcast day.

Philip T. Partain
Department of Atmospheric Science
Colorado State University
Fort Collins, Colorado 80523
Spring 1998

ACKNOWLEDGEMENTS

We are indebted to several people who have helped make this research possible. We would first like to thank Dr. David Randall and Dr. Richard Eykholt for their review of the manuscript. Andrew Heidinger started work in the application of the Equivalence Theorem to problems such as those investigated in this work and assisted in its implementation. He provided invaluable help in constructing the Monte Carlo model and also created the 32-stream adding-doubling model which was used to validate the Monte Carlo/Equivalence Theorem model. Many discussions were held with Philip Gabriel who helped with Monte Carlo modeling issues and statistical probability along with many other questions and concerns. Paul Stackhouse created a two-stream model from which the k-distribution data and its implementation were obtained.

Discussions held with other colleagues here at Colorado State University also aided in the completion of this work. In particular, Steve Miller, Charles Drummond, and Ian Wittmeyer contributed many ideas and/or support. We are also grateful to Sue Lini and Angie Narum who helped with a variety of administrative concerns.

Funding for this research was provided by Department of Energy contracts #DE-FG-03-94ER61748, #DE-FG-03-95ER61985, and #DE-FG-03-97ER62357. Data were obtained from the Atmospheric Radiation Measurement (ARM) Program sponsored by the U.S. Department of Energy, Office of Energy Research, Office of Health and Environmental Research, Environmental Sciences Division.

CONTENTS

LIST OF FIGURES

LIST OF TABLES

Chapter 1

INTRODUCTION

Are these large absorptances real, or are they caused by instrumental deficiencies, or a three-dimensional effect? The ideal plane-parallel and homogeneous conditions are seldom realized, and hemispheric pyranometers may perhaps be somewhat inadequate for accurately determining fluxes in complicated cloud situations. Clearly, more sophisticated radiometric techniques are required to resolve the cloud absorptance question.

—Herman (1977)

1.1 The Nature of the Problem

For more than four decades, a discrepancy between measured and simulated atmospheric absorption in the shortwave solar part of the electromagnetic spectrum has been observed in the presence of clouds. Studies have questioned to some degree every aspect of measurement uncertainty and theoretical inaccuracy, however the discrepancy still remains unresolved. If measured radiative fluxes are interpreted as truth, many simulations result in an underestimation of atmospheric absorption. This discrepancy, termed "anomalous absorption", has major implications on our understanding of radiative transfer in the Earth's atmosphere and all atmospheric processes that are affected by solar absorption. For example, about 70% of the globally averaged solar radiation incident on the top of the atmosphere (TOA) is absorbed by the surface and atmosphere. Small errors in partitioning this absorption between surface and atmosphere can lead to large errors in our understanding of dynamic and climate processes. Roughly 80% of the solar radiation that is absorbed in the tropics is used to heat the surface and drive oceanic circulations. This

implies that the remaining 20% goes toward driving atmospheric circulations. Inaccurate specification of solar absorption leads to large errors in the ocean and atmosphere dynamics in climate models. This has implications on heat and energy budgets and, therefore, the state of the simulated equilibrium climate.

On a smaller scale, incorrect cloud absorption theory can have an effect on modeled cloud dynamics. Davis et al. (1979) note that inaccurate vertical profiles of solar absorption in modeled cloud systems have implications on cloud droplet growth and the static stability of the cloud layer.

In addition to atmospheric dynamics, incorrect absorption theory can lead to problems in remote sensing. Retrievals are dependent on forward model simulations which involve perturbing the optical properties of atmospheric constituents and calculating resulting flux or radiance. Inaccurate absorption theory can lead to a misrepresentation of the state of physical and optical properties of any given scene.

Ramanathan et al. (1995) refer to the problem concerning anomalous absorption as "a missing physics" that is not accounted for in present theory. This is a position that has gained much support in recent years in studies like Cess et al. (1995) and Pilewski and Valero (1995) which observe absorption in the presence of clouds in excess of both model results and the results presented by earlier studies which first introduced the discrepancy.

However, the physical cause of increased solar absorption in the atmosphere is only part of the controversy. Adding to the confusion are the many studies that have presented findings which agree with model simulations. Hence, it is unclear if the anomaly really exists. There are several factors which may be the cause of the discrepancy:

- Operational Errors
  - instrument error or inadequate measurement technique
  - inaccurate parameterization of observed atmospheric constituents used for model input
- Theoretical Errors
  - inaccurate absorption theory (aerosol, gas, cloud)

– unresolved effect of cloud heterogeneity

The goal of this study is to provide insight into the last item on the above list: the effect of cloud heterogeneity. Most simulations of observed fluxes are performed with a plane-parallel radiative transfer model. Under the plane-parallel approximation, cloud fields are horizontally homogeneous and infinite in extent. However, the horizontal homogeneity of an actual cloud field rarely occurs on scales large enough to make this assumption valid. Stephens and Tsay (1990) note that the relevance of plane-parallel theory is "much less developed" than the other possible causes of anomalous absorption. Though several studies have been published in the literature which have investigated the role of cloud heterogeneity on the reflection of radiation from clouds (usually though the use of a Monte Carlo model), few have investigated its effect on atmospheric absorption. Also, as a result of limited radiative transfer theory, none have investigated absorption at high spectral resolution across the shortwave solar spectrum. As Hignett and Taylor (1996) state, "greater spectral resolution in the broad-band Monte Carlo model will be necessary to compare with better spectrally resolved observations."

In this study, the development of a Monte Carlo model with unlimited spectral resolution for atmospheric absorption properties is discussed. The model is then used to provide further insight into the role of cloud heterogeneity on the redistribution of solar radiation. Even if cloud heterogeneity does not solve the anomalous absorption issue, it still has many implications on the remote sensing (McKee and Cox, 1974; Stephens and Preisendorfer, 1984) and climate modeling communities (Harshvardhan and Randall, 1985).

1.2 The Shortwave Solar Spectrum and the Measurement of Atmospheric Absorption

Shortwave solar radiation is defined as the electromagnetic radiation emitted from the sun that is incident on the top of the atmosphere (TOA) between the wavelengths of .2 and 4 μm. The spectral emission of the sun can be approximated by the Planck

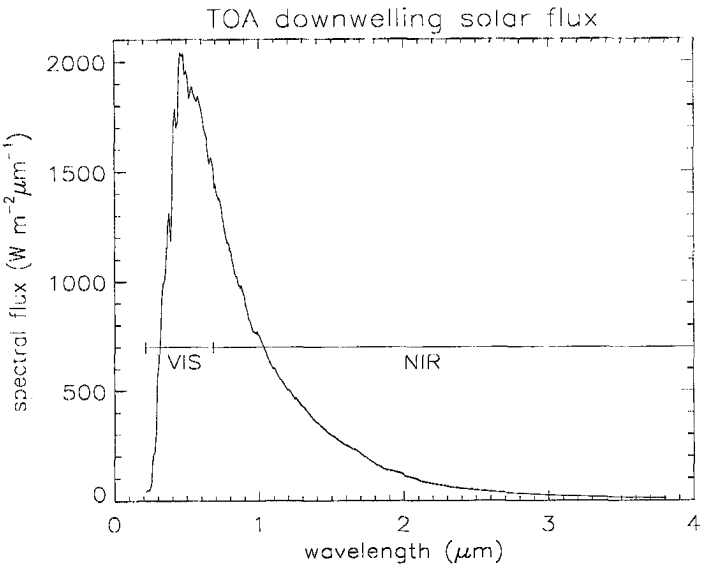

Figure 1.1: Downwelling solar spectral flux at TOA and the ranges of the VIS and NIR portions of the spectrum.

function:

$$F_\nu = \frac{2\pi hc^2}{\nu^5(e^{hc/k\nu T} - 1)} \tag{1.1}$$

where ν is the wavelength (the character λ is reserved for use later in this study), h is Planck's constant, T is the temperature of the emitter, c is the speed of light, and k is Boltzmann's constant. The temperature of the sun is near 6000 K. The solar spectral flux that reaches TOA is shown in Fig. 1.1. The spectral radiation curve shown differs from that of a true blackbody described by the above equation as a result of absorption features in the sun's atmosphere.

The shortwave solar spectrum is divided into the visible (VIS) region which ranges from .2 to .68 μm and the near infrared region (NIR) which ranges from .68 to 4 μm. The spectral ranges of the VIS and NIR regions are also shown in Fig. 1.1. The spectral flux is expressed in $Wm^{-2}\mu m^{-1}$. The integration of spectral flux between two wavelengths provides the broadband flux which is expressed in Wm^{-2}. Hence, integration of the spectrum between .2 and 4 μm results in the total shortwave broadband flux whereas integration over the VIS or NIR regions result in VIS or NIR broadband flux.

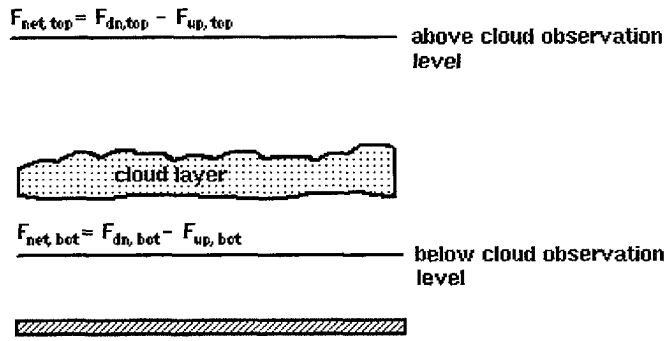

Figure 1.2: A common method of observing column absorption involves differencing the net flux above and below cloud.

Solar radiation that enters the atmosphere can be absorbed or scattered by clouds, gas, aerosol, and the Earth's surface. As seen in the first section of this chapter, the amount of atmospheric absorption that occurs is controversial. The most common method of estimating absorption from observations or model simulations is derived from an energy conservation relationship. Namely, for a conservatively scattering atmospheric column (no absorption) the flux in must equal the flux out. This is to say that the net fluxes at the top and base of the column must be equivalent. If absorption is present in the atmosphere, the amount is equal to the difference of the net fluxes:

$$A = \frac{(F_{dn,top} - F_{up,top}) - (F_{dn,bot} - F_{up,bot})}{F_{dn,top}} \tag{1.2}$$

This difference is normalized by the downwelling flux at TOA so that absorption is expressed as a percentage of the incoming solar flux. For theoretical simulations, the fluxes at the required levels are produced by a model. For field observations, this requires measurements at the bottom of the column from surface or airborne instruments and measurements at the top of the column from airborne or space borne instruments. The geometric setup for obtaining the measurements important for estimating absorption is shown in Fig. 1.2.

Observations of atmospheric absorption in the field suffer from a problem not encountered in model simulations. While the formulation for observing column absorption from a model or field observations in (1.2) is accurate for a plane-parallel cloud, sampling

issues arise when clouds become heterogeneous. These sampling issues are not a problem for simulations because clouds are approximated as plane-parallel. However, model error is created by this approximation and will be discussed later. When clouds become broken, flux measurements change depending upon where the measurements are made. Thus, to get a representative measurement of the area average fluxes for a single layer cloud field, the field must be sampled until it is determined that all scales of horizontal variability have been observed and that more measurements would be redundant. This determination is almost impossible to perform while measurements are being made and very difficult to perform when analyzing data. Therefore, most measurements of absorption are said to be representative of the cloud field when the time series of absorption converges to a steady value. Of course, the accuracy of this method is variable and dependent on large scale cloud morphology. This is made increasingly difficult by the non-stationarity of cloud statistics. That is, clouds grow, move, and dissipate as measurements are being performed. Thus, averages and deviations change in time and space. For this reason, it may be impossible to adequately sample a cloud field.

To try and reduce errors created by cloud heterogeneity, Ackerman and Cox (1982) introduce a correction to (1.2). This correction accounts for leakage of solar radiation out the sides of broken clouds that is not measured by instruments above and below the cloud:

$$A = \frac{(F_{dn,top} - F_{up,top}) - (F_{dn,bot} - F_{up,bot}) - \sum F_s}{F_{dn,top}} \tag{1.3}$$

where $\sum F_s$ is the unmeasured flux through the side of the cloud. To get an estimate of the flux through cloud side, absorption calculations are performed at a wavelength where absorption does not occur. If a positive or negative absorption results from this calculation, then it is attributed to "apparent" absorption and subtracted from or added to the total absorption. In addition to providing a better estimate of atmospheric absorption, this technique decreases the sampling time required for fluxes to converge.

Other observation techniques can be used to infer atmospheric absorption. Among these is the use of column albedo. Albedo (R) is simply:

$$R = \frac{F_{up,top}}{F_{dn,top}} \tag{1.4}$$

measured at the top of the atmospheric column. Along with discrepancies in absorption, several studies have reported an overestimation of albedo by models. Assuming that surface albedo was properly assigned and downwelling flux at the top of the column is easily derived, a low observed albedo implies that the atmosphere absorbed more and reflected less solar radiation than theory describes. Albedo is a measurement that is inherently more reliable than net flux differencing because observations are made simultaneously in time and location.

Directional reflectance or vertical radiance is a measurement that is similar to albedo observation except that only upwelling radiation that enters the instrument from directly below in a vertical path is seen. This measurement can be compared to simulations, however this technique suffers greatly from sampling issues and cloud heterogeneity effects as noted by Foot (1988).

The parameter β has been created to provide information about atmospheric absorption. This parameter is the slope of the line fit to a plot of observed or calculated TOA albedo versus normalized surface insolation:

$$\beta = \frac{dR}{dT} = \frac{d(F_{up,top}/F_{dn,top})}{d(F_{dn,bot}/F_{dn,top})} \tag{1.5}$$

where T is the "transmission" of the atmosphere. The theory behind this procedure is that albedo plus transmission plus absorption is equal to one. Thus, the change in the slope of an albedo versus transmission plot should be due to changes in atmospheric absorption. Typical model values of β are around .8, whereas observations produce β near .55 (Cess et al., 1995).

A similar parameter, f_s, has also been used to infer the existence of anomalous absorption. This parameter is the ratio of shortwave cloud forcing at the surface to that at TOA:

$$f_s = \frac{C_{s,bot}}{C_{s,top}} = \frac{F_{net,bot}(cloud) - F_{net,bot}(clear)}{F_{net,top}(cloud) - F_{net,top}(clear)} \tag{1.6}$$

Cloud forcing C_s at the top or bottom of the atmosphere is the difference between the all sky (cloudy) net flux and clear sky net flux. Model values are typically less than 1.2, whereas observations place this value closer to 1.5 (Ramanathan et al., 1995).

1.3 The ARM Program and the ARESE IOP

To investigate the interactions between solar radiation and the Earth's atmosphere, the United States Department of Energy (DOE) started the Atmospheric Radiation Measurement (ARM) Program. As described in the *ARM Program Plan* (U. S. DOE 1990), the main objectives of this endeavor are to:

- describe the radiative flux profile of the clear and cloudy atmosphere,
- understand the processes determining the flux profile,
- parameterize the processes determining the flux profile for incorporation into general circulation models (GCMs).

Several Cloud and Radiation Testbed (CART) sites around the world were dedicated for observational research in support of the above objectives. These sites include the North Slope of Alaska (NSA), the Southern Great Plains (SGP) in northern Oklahoma, and the Tropical Western Pacific (TWP). Each CART site consists of a high concentration of instrumentation which provide data to the research community.

As a result of the recent intensification of the debate involving the role of clouds in absorption of solar radiation, the DOE organized an intensive observation period (IOP) to add understanding to the issue. This IOP, called the ARM Enhanced Shortwave Experiment (ARESE) was implemented in the fall of 1995 at the SGP field site. The primary objectives of the ARESE program[1] were to:

- directly measure the absorption of solar radiation by clear and cloudy atmospheres and place uncertainty bounds on these measurements,
- investigate the possible causes of absorption in excess of model predictions.

Using instrumented platforms on the ground and on board aircraft and satellites, radiometric flux data were obtained for a variety of atmospheric conditions between 25 September

[1] from the ARM web site: http://www.arm.gov/docs/index.html

and 1 November, 1995. In support of the radiometric measurements, cloud radar, lidar, and radiosondes provided more observations of cloud structure and atmospheric quantities to help accomplish the objectives mentioned above.

The procedure used to obtain radiometric measurements used to study atmospheric absorption involved aircraft colocation. To measure net flux above and below cloud level as described in the previous section, two aircraft flew in a "stacked" formation to obtain net flux information: the Twin Otter at an altitude near 3 km and the Egrett near 13 km. The two aircraft flew in patterns that would periodically result in a colocation between them and the ARM CART site to provide further information about the column flux profile.

For the present study, the measurements of greatest interest are the radiometric data obtained by the instruments on board the two aircraft. Both aircraft carried a set of upward and downward looking RAMS radiometers to measure broadband solar flux. These included the Total Solar Broadband Radiometer (TSBR) which measured total flux in the .26 to 4.0 μm range and the Fractional Solar Broadband Radiometer (FSBR) which measured NIR flux in the .69 to 2.9 μm range. Subtracting the FSBR data from the TSBR data provides a measurement of VIS flux (.26 to .69 μm).

In addition to the RAMS radiometers, each aircraft carried upward and downward looking Total Direct Diffuse Radiometers (TDDR) which measure spectral flux at seven wavelengths in the solar spectrum. These wavelengths are .5, .862, 1.064, 1.25, 1.5, 1.65, and 1.75 μm. The RAMS and TDDR instruments were provided by Scripps Institution of Oceanography at the University of California, San Diego.

The Egrett also carried a radiometric instrument called the Scanning Spectral Polarimeter (SSP) provided by Colorado State University. This instrument measured spectral flux at 40 wavelengths in the solar spectrum. The SSP was only mounted on the Egrett and was downward looking to measure upwelling or reflected spectral flux and radiance. A graphical representation of the spectral ranges of the above instruments is shown in Fig. 1.3 overlayed on a plot of the incoming spectral flux at the top of the atmosphere.

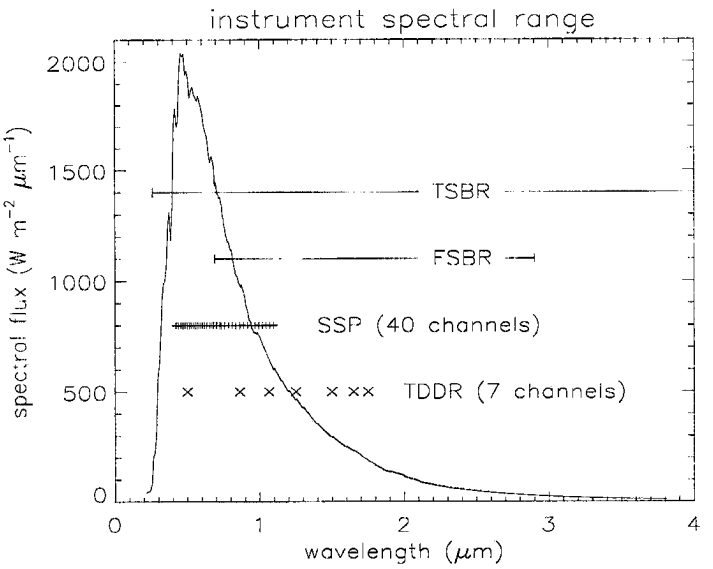

Figure 1.3: Spectral ranges or measurement wavelengths of the TSBR, FSBR, SSP, and TDDR instruments.

Spectral and broadband flux datasets produced by these instruments during the ARESE IOP as well as derived albedo and absorption observations will be analyzed and compared to model simulations in this study.

1.4 Scientific Objectives

The first objective of this study is the development of a Monte Carlo model that can simulate broadband and high resolution spectral fluxes over the shortwave solar spectrum for heterogeneous atmospheres. In the past, Monte Carlo broadband simulations, though accurate, were limited in the spectral information they provide largely due to the computational burden required for these simulations. In this study, modifications to the Equivalence Theorem as introduced by Irvine (1964) overcome most of these problems when run in concert with a Monte Carlo model. Using this method, any spectral resolution of gas, cloud, and surface absorption can be used in a simulation that covers the entire shortwave solar spectrum. This is a new application of this theorem and a major development in expanding the power and utility of the Monte Carlo technique for solving radiative transfer problems in complex heterogeneous atmospheres. Because this new

method is theoretically exact, it is proposed that a model using the same theory be used to perform benchmark line by line calculations for complex cloud situations.

Once formulated for use in this study, the model will be used to provide insight into the effect of cloud heterogeneity on radiative fluxes, absorption, and albedo. The first experiment involves the effect of the spatial distribution of cuboidal clouds in the form of cloud fraction and compares the results with those obtained from the plane-parallel parameterization. The second experiment compares results from a cloud field that is internally heterogeneous but unbroken against those from the plane-parallel approximation. Hence, the notion of cloud fraction no longer applies. This is performed to show errors that might be incurred by a general circulation model that only accounts for heterogeneity in terms of cloud fraction.

The model is then used to try and reproduce observed flux, albedo, and absorption observed during the ARESE IOP. Because cloud macrophysical and microphysical properties were not recorded during the IOP, this exercise is not a direct simulation of the state of the radiative fluxes that were present during the field observations. Using knowledge gained from the cloud heterogeneity experiments listed above, this exercise does, on the other hand, act as a consistency check between observations above and below cloud level and between comparable instruments measuring the same quantities.

1.5 Plan Of This Research

This thesis begins with a summary of the history of absorption and albedo observations which have both supported and refuted the existence of anomalous absorption. In addition, the possible errors that may produce the discrepancy as studied by previous researchers is discussed.

Next, the development of the Monte Carlo model and the theory behind the extension of this technique to high resolution spectral simulations necessary for this study will be presented. This begins with a review of applicable radiative transfer parameters and theory.

Finally, the model will be used in simple experiments to determine the effect of cloud heterogeneity on cloud, gas, and total atmospheric absorption. The broadband and spectral results will be compared to those obtained when the plane-parallel approximation is invoked. It is discovered that although cloud heterogeneity affects atmospheric absorption in ways that are explainable in terms of photon path lengths and cloud amount, the amount of absorption change is not sufficient to explain the differences between theory and observation.

Using what is learned about the effect of cloud heterogeneity from these experiments, model simulations are performed and results are compared to selected ARESE observations. It is shown that the most probable source of the absorption discrepancy between theory and observations made during this field experiment is instrument error, a result which has implications on results published by other researchers.

Chapter 2

A HISTORY OF MODEL AND OBSERVATION DISCREPANCY

2.1 Introduction

Since the turn of the century, experiments and simulations have been performed to try and improve our knowledge and understanding of the mechanisms governing the reflection, transmission, and absorption of radiation by the Earth's atmosphere. However, controversy has hindered this process. For over forty years, scientists have been unable to precisely define the atmosphere's role in the absorption of solar radiation. Theoretical model simulations have been performed using the most current knowledge of cloud microphysics and gas absorption characteristics, yet comparisons of those simulations to atmospheric observations do not reveal whether or not that knowledge is correct. Comparisons made between theoretical and observed absorption have shown results ranging from good agreement to a gross underestimate of absorption by atmospheric models. The disagreement has been termed anomalous absorption. The discrepancy between theory and measurements is not limited to absorption. Many studies which only compare simulated and observed albedo also show disagreement. This, however is to be expected because albedo, like absorption, is calculated using the upwelling and downwelling fluxes at the top of the atmospheric column in question.

This chapter gives a brief synopsis of past work in this arena. First, studies which show anomalous absorption or albedo discrepancy and studies which show good agreement between simulations and observations will be reviewed. Second, past results showing the theoretical affect of aerosol, gas, and cloud particles on absorption and albedo will be discussed. Finally, the results of the 1995 ARESE IOP will be presented.

2.2 Observations of Anomalous Absorption

Anomalous absorption has been observed to varying degrees in past research. Herman and Curry (1984) report fair agreement for the total solar and NIR portions of the spectrum, but terrible agreement in the VIS portion where the model underestimates visible absorption. This result appears even though the modeled and observed reflectances and transmissions agree to within 10%. Of course, a systematic trend in a particular direction for each flux measurement can result in too much or too little absorption. This study speculates that several uncertainties may have played a large role in the results. It states that cloud inhomogeneity including temporal and spatial variations can lead to errors. Also, it mentions a caveat related to the technique of net flux differencing above and below cloud level. There exists a substantial amount of observational uncertainty resulting from this method because absorption is computed as the residual of four large fluxes which nearly cancel. Thus, Herman and Curry conclude that it does not appear possible to measure absorptances in regions of the spectrum where absorption is small due to the uncertainties resulting from cloud inhomogeneity.

Foot (1988) observe twice as much absorption in the cloudy atmosphere as is obtained in model simulations. Attempts to force the model to match the observations failed. The model simulations show a lack of absorption change due to a $\pm 25\%$ change in cloud optical depth and cloud particle effective radius (r_e). Also, the aerosol absorption coefficient observed is one order of magnitude smaller than that required to model the observed absorption. It is stated that cloud top structure plays a role in decreasing the vertical radiance reflected off the cloud. Shadows due to cloud top structure are shown to bring model and observed radiances into agreement, however reflected hemispheric flux shows little change. Therefore, cloud albedo and absorption are not functions of cloud top structure.

A study performed by Twomey and Cocks (1982) compares observed cloud albedos to modeled ones and finds that neither the absolute nor relative magnitudes of the reflectances agree very well. The measured cloud droplet effective radius was 8 μm. In or-

der to force the model to match the observations, an effective radius of .5 μm and droplet density of 2 million drops per cm^3 must be used. These are clearly non-physical values considering typical cloud droplet densities range from 72 to 440 $drops/cm^3$ (Stephens, 1979). A physical absorption is ruled out because the difference between the observed bulk absorption coefficient and that needed to bring the model into agreement with the observations is smallest in optically deep regions of the cloud and largest in optically thin regions. If the enhanced absorption was related to clouds, this should work in the opposite direction. Twomey and Cocks note that lateral inhomogeneity evident in the observations and not accounted for in the model may pose a problem. However, introducing cloud heterogeneity seemed to work in the wrong direction as well.

Stephens et al. (1978) show an increase in solar absorption beyond theoretical prediction and, unlike Twomey and Cocks (1982), it is correlated with an increase in cloud thickness and density. However, it is noted that these measurements are within the expected error of experimental uncertainty so the existence of anomalous absorption cannot be concluded.

Reynolds et al. (1975) conclude cloudy sky absorption is 2-3 times higher than that for clear air. This is compared to results obtained by London (1957) and Drummond and Hickey (1971) to show that observed absorptions vary from 12 to 36%. However, there is no mention of the disagreement between the upper end of this observed range and model calculations.

In a study of vertical radiance reflected off a stratocumulus cloud deck, Stephens and Platt (1987) show good agreement in the VIS portion of the spectrum between observations and model, but an overestimate of radiance by the model in the NIR. It is speculated that this may indicate more absorption in the NIR than theory can predict. This is contrary to the study by Herman and Curry (1984) which suggested the anomaly occurs in the VIS portion of the spectrum. The results of Stephens and Platt (1987) are shown in Fig. 2.1. As noted by Foot (1988), cloud top heterogeneity plays a role in lowering reflected radiance. However, it does not appear this process is occurring here because the model and observed VIS radiances seem to agree. It may be possible that heterogeneity has a

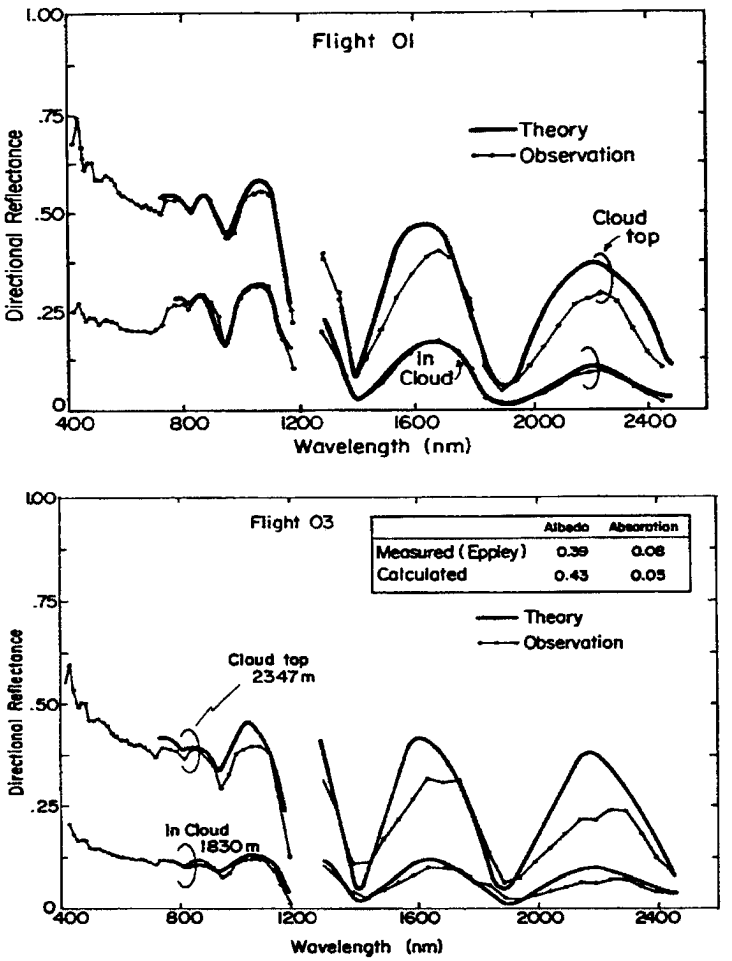

Figure 2.1: Comparison of the calculated (heavy curves) and measured (light curves) spectral reflectances for two Sc cases. The comparisons are shown for cloud top and some level approximately in the middle of the cloud. Also included in the lower panel are the measured and theoretically derived broadband albedos and shortwave absorption estimates. (from Stephens and Platt, 1987)

spectral signature and is more pronounced in the NIR. The lower observed radiances in Fig. 2.1 seem to support the results of others which conclude anomalous absorption is a NIR phenomenon. Stephens and Platt discount the effects of the absence of large cloud droplets which may have been missed by microphysical observations. Included in the Fig. the measured and calculated solar albedo and absorption which also show discrepancy. This paper also notes that the angular distribution of reflected energy is more anisotropic for cumulus clouds than for stratiform clouds, a property which may be important and will be discussed later in this chapter in terms of instrument error.

Hignett (1987) compares measured and simulated marine stratus cloud albedo and finds that model simulations tended to overestimate albedo in the NIR and underestimate the albedo in the VIS. This is similar to the results obtained by Stephens and Platt (1987) discussed above. However, Hignett states that better agreement between model and observations is possible if more computational effort is put forth. When the optical properties of cloud droplets are obtained from Mie theory instead of a parameterization scheme, better agreement is obtained for all cases even though the issue is still not completely resolved.

A study by King et al. (1990) also shows evidence of anomalous absorption. However, the observational techniques employed differ from those of previous studies. The procedure involves obtaining the angular distribution of radiance deep within a cloud where the direct solar beam has been completely attenuated and the remaining radiation is completely diffuse. Here, absorption properties can be inferred from the radiance information by way of a technique called the diffusion domain method (King, 1981). Fig. 2.2 shows their results for a flight through a stratocumulus cloud off the California coast. Plotted are the observed and simulated similarity parameter (s) as a function of wavelength. The similarity parameter is related to cloud absorption through the single scattering albedo. Absorption is zero for $s = 0$ and increases with increasing s. As seen in the plot, the measured values (dots) indicate a consistently larger absorption than theory predicts (dashed line). The authors note that this is the result of only one case study, but based on the bias conclude that this is evidence for anomalous absorption.

Within the past several years, several studies have been published which unambiguously claim anomalous absorption is real and systematically measurable. Cess et al. (1995) compare model and observed absorptance for several locations around the globe using a surface pyranometer colocated with satellite observations of outgoing flux at the top of the atmosphere. Two indicators of absorption are used in this study. First, the ratio (f_s) of surface to TOA cloud radiative forcing (CRF) is computed from measured and simulated results for two regions: one surrounding the National Oceanic and Atmospheric Administration (NOAA) Boulder Atmospheric Observatory (BAO) tower in Colorado, and the other located in the tropical western Pacific. The model atmospheres used in the study

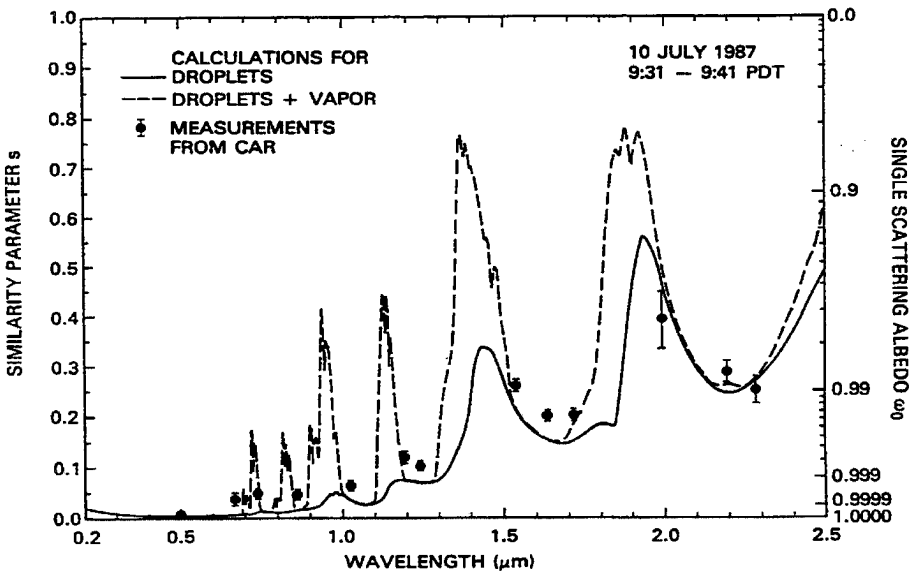

Figure 2.2: Calculations of the similarity parameter as a function of wavelength for water droplets alone (solid line) and drops plus vapor (dashed line) for a cloud droplet size distribution and water vapor conditions of the marine stratocumulus cloud of 10 July 1987. The single scattering albedo scale is valid at 0.754 μm, where the cloud asymmetry factor $g = 0.848$. The measurements derived from the cloud absorption radiometer (solid circles with error bars) are averages of the similarity parameter derived by applying the diffusion domain method to a 50 km section of the cloud. (from King et al., 1987)

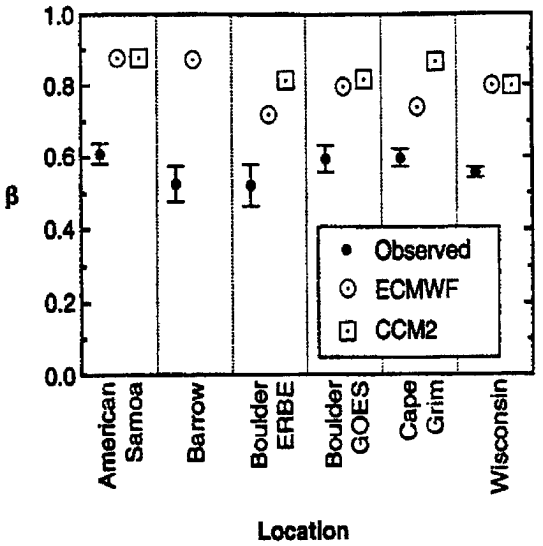

Figure 2.3: Comparison of values of β (determined from the ECMWF GCM and CCM2) with the observed values. The vertical bars denote the 95% confidence intervals of the observations. (from Cess et al., 1995)

produced f_s near 1.5 whereas model simulations produce f_s closer to 1.0. Second, the derivative of TOA albedo with respect to the cloud forcing ratio β was computed for five locations around the globe. Similarly, the theoretical β calculated is around .8 as seen in Fig. 2.3, yet the observations at each location are clustered around .6. Both of these results are interpreted as the underestimation of atmospheric absorption by the model. The authors discount the effects of aerosol and note that increased water vapor associated with increased cloudiness is not the cause of the measured anomalous absorption. Error associated with the surface measurements was discussed and was limited to the typical errors associated with commercial pyranometers. This error is within the linearity of the pyranometers ($\pm 0.5\%$). The measured absorption is significant and would reduce the globally averaged surface insolation by 25 W/m^2.

Atmospheric absorption measurements were made by Pilewski and Valero (1995) in the tropics during the Tropical Ocean Global Atmosphere – Couple Ocean Atmosphere Response Experiment (TOGA-COARE). Here, 20 flights were made above and below cloud layers with identical instrumentation to record net fluxes. The results presented are consistent with Cess et al. (1995), however the magnitude of the derived cloud forcings

were different. Pilewski and Valero did make an attempt to lessen the effects of cloud inhomogeneity by filtering the data. This did result in a reduced "cluster of lower albedo cases" but it is unclear whether or not this can be interpreted as the effect of cloud inhomogeneity on absorption. They conclude that the absorption characteristics are water-like and that there is still a need to investigate its spectral characteristics, especially in the NIR.

Observations of anomalous absorption are not only linked to cloud effects. In a paper by Arking (1996), surface flux measurements from the Global Energy Balance Archive (GEBA) and satellite flux observations from the Earth Radiation Budget Experiment (ERBE) were used to calculate globally averaged atmospheric absorption for comparison with model results. It is concluded that the model underestimates the magnitude of atmospheric absorption by 25 to 30 W/m^2. However, this increased absorption is attributed to clear sky effects rather than cloud effects. No correlation between atmospheric absorption and cloud amount is seen, whereas a correlation does exists with water vapor amount. These results are contrary to those quoted by Cess et al. (1995).

2.3 Observations of No Anomalous Absorption

Several studies have presented results of comparisons between observations and model simulations which did not result in any evidence of anomalous absorption. In an experiment performed over the Arabian Sea in 1979, Ackerman and Cox (1981) measured column absorptance between stacked aircraft in a stratocumulus cloud field. Actually, the raw measurements show considerable absorption in both the NIR and VIS regions of the solar spectrum. However, because cloud absorption in the visible region is negligible, the apparent absorption measured is assumed to be a measure of the leakage of radiation out the sides of the clouds that the pyranometers cannot see. By subtracting this apparent absorption from the NIR measurement, the observations and model predictions agree very well. This correction method brought the observed absorption for the total broadband down to 9.3 % from 17.8 %. This technique also decreased the averaging distance necessary from 24 to 3 km to allow the measured net fluxes to converge.

Slingo et al. (1982) present results from the Joint Air-Sea Interaction (JASIN) experiment which show no evidence of anomalous absorption. This conclusion is made even though they recognize the difficulty in making absorption observations. Two models are used for comparison with the measurements. Even though the models disagree on the amount of absorption by 15 %, both simulated results fall within the error of the measurements. Observed absorptance was $52 \pm 20\ W/m^2$.

By employing the correction method described by Ackerman and Cox (1982), Rawlins (1989) measured absorptances over a 1.5 km flight track in the presence of cloud at 8 to 12 ± 4 %. In clear air, the values are 2 to 4 ± 2 %. Because the measured cloudy sky absorptions are similar to measurements made by others who saw no evidence of anomalous absorption, the conclusion is made that excess absorption is not seen here either. However, these values are only compared to clear sky model simulations in this study.

Hasayaka et al. (1995), using the Ackerman and Cox (1981) correction method, also report no evidence of anomalous absorption. Using this method, fluxes measured from broken cloud fields are corrected and the resulting absorptances match theoretical predictions made using the plane-parallel approximation. Hasayaka et al. note the importance of water vapor and cloud LWC to atmospheric absorption and state that the cloud droplet size distribution is not as important.

Like the study performed by Cess et al. (1995), Li and Moreau (1996) obtain global values for the ratio of surface to TOA cloud forcing (f_s). Data used for the research consists of four years of ERBE satellite flux measurements and GEBA surface flux measurements similar to the dataset used by Arking (1996). This study performs an extensive sensitivity analysis for f_s and the results of the global observations are interpreted in the context of that analysis. While conventional radiative transfer models generally produce $f_s = 1$, as seen earlier, Cess et al. (1995) and Pilewski and Valero (1995) report f_s for the real atmosphere around 1.5 or greater. The average cloud forcing ratio found by Li and Moreau is around 1.1, which is very close to the model values. However, there appears to be a large dependence of f_s on latitude. In the tropics, values of 1.5 are calculated which is consistent with the afore mentioned studies. On the other hand, the values of f_s for midlatitudes

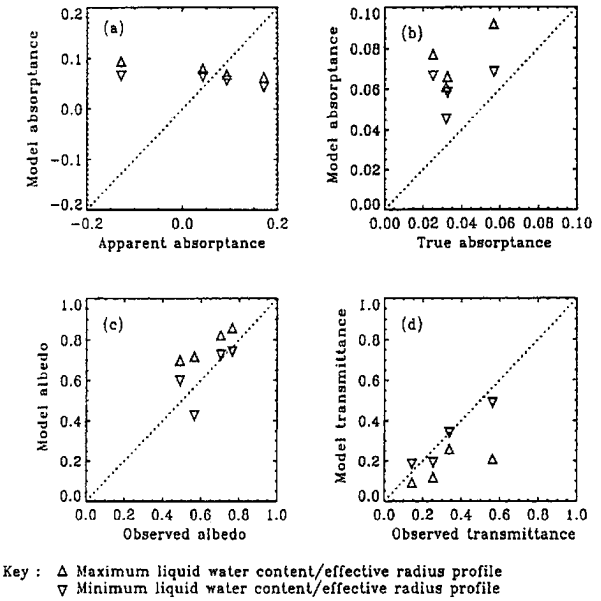

Figure 2.4: Scatter plots of the modeled and (a) observed absorptance, (b) true absorptance, (c) observed albedo, and (d) observed transmittance for four cloud cases. The model results are those initialized with the minimum and maximum profiles of LWC/r_e as explained in the key. (from Taylor et al., 1996)

and polar regions drop to 1.1 and less than 1, respectively. Possible explanations for these variations include changes in mean cloud structure and solar zenith angle. In addition, the high values calculated in the tropics are less reliable than in other regions as a result of large amounts of aerosol introduced by biomass burning, sparsely located observation sites, and datasets of short time duration. The conclusion presented by Li and Moreau is that if a cloud absorption anomaly exists, it is "neither as common nor as large, as indicated from some recent studies".

In addition to studies which show no discrepancy between theory and measurements, Taylor et al. (1996) present a result which shows model overestimation of absorption. This overestimation occurs for all realistic LWC and r_e profiles. Their results for model absorptance, albedo, and transmittance versus the observations are plotted in Fig. 2.4. The difference between the apparent absorptance and the true absorptance indicates the importance of the term $\sum F_s$ in the Ackerman and Cox (1982) correction. The albedo and transmittance between theory and measurements are in closer agreement.

2.4 Operational Error Sources

Operational error is defined as error that could cause differences between observed and simulated radiative quantities assuming the theory behind the simulation is correct. This covers error in model input from which simulated quantities are obtained and error in the instruments which provide the observed quantities for comparison.

2.4.1 Model Input Error

Errors in model input usually result from a lack or inadequate quality of detailed observations of the atmosphere which is to be simulated. Errors can be present in all parameters, the most important including the surface albedo, gas profile, cloud and aerosol microphysics, and cloud position and morphology.

The error in land albedo can be large due to the potentially great variability of mineral or vegetation present. There are several methods of obtaining the albedo including measuring the net flux at the surface, measuring the net flux over a flight track with a low flying aircraft, and satellite retrievals. However, surface measurements may be vastly different from the actual albedo averaged over a large area, aircraft measurements only capture part of the variability, and satellite retrievals depend on models of atmospheric transmission and absorption which are the theories that simulations are trying to test. Ocean albedo, though much more uniform, suffers from specular characteristics under clear or partly cloudy conditions. It is also sometimes neglected because it is low.

The accuracy of gas profiles is important because gas absorption can account for a large fraction of the total solar absorption. Also, gas absorption creates many spectral features in simulated flux which need to be compared to spectral observations. Thus, the accuracy of radiosondes or other methods of retrieving gas profiles plays an important role in model accuracy. In many situations, gas profiles are not available. In this case, a profile obtained from the standard atmosphere (McClatchey et al., 1971) is used. Using a standard profile as an estimate of the actual gas profile also introduces errors.

Like gas profiles, information about cloud and aerosol microphysics is limited by quantity and quality. Ideally, the cloud droplet size distribution and liquid water path

(LWP) should be obtained from in situ measurements. When these observations can be made, instrument error in deriving these quantities is present. This instrument error is compounded by sampling error. In the case of an instrument mounted on an aircraft like the FSSP (which is used to measure drop size distribution), only a "tube" of air a few centimeters in diameter along the flight track can be sampled. Extrapolation to the entire cloud can be difficult. When in situ observations are not present, an assumed droplet distribution and LWP must be used. Though horizontally more homogeneous, aerosol observations suffer from similar errors.

Cloud position and morphology can be the largest sources of uncertainty in model input. It is well established that cloud heterogeneity changes reflected and transmitted flux through a cloud layer (see McKee and Cox, 1974; Davies, 1978; Weinman and Harshvardhan, 1982; Stephens and Priesendorfer, 1984; Stephens, 1988a; Stephens and Tsay, 1990; Taylor et al., 1996; and Hignett and Taylor, 1996). Even if cloud structure data is obtained from satellite or radar observations, most radiative transfer models cannot account for it beyond a simple cloud fraction parameterization. This is true because most models assume a one-dimensional or plane-parallel atmosphere. Stephens and Platt (1987) note the lack of adequate multidimensional radiative transfer theories.

In short, model input is limited by what is available or what can be accommodated. According to Li and Moreau (1996), "it is likely that the errors resulting from inaccurate input parameters are comparable to, or even larger than, the discrepancies reported thus far between observed and computed cloud absorption". If this is true, the task becomes one of determining which parameters are the cause of the discrepancy.

2.4.2 Observation Error

The radiative fluxes that are observed and compared to model output are also subject to error. This error is a result of instrument inaccuracies or inadequate measurement technique.

Instrument error usually pertains to calibration and the knowledge of known biases and offsets throughout an experiment. This error is instrument dependent. For example,

pyranometers used for net flux differencing above and below cloud have cosine response functions that are indicative of the relative amount of radiation entering the detector at different angles. For an ideal instrument, this function would match a cosine curve. However, pyranometers rarely exhibit an ideal cosine response function. Though variations in this function are accounted for during calibration, it is done so assuming reflection from an isotropic surface. Radiation reflected from or transmitted through clouds is seldom isotropic. Therefore, cloud heterogeneity introduces measurement error. Foot (1988) states that errors resulting from a non-ideal cosine response could be ± 2 to ± 10 Wm^2, altering albedo by $\pm 2\%$. Multiple pyranometers used in conjunction also suffer from relative calibration errors between instruments.

As noted by Herman and Curry (1984), the method of net flux differencing has been criticized as a means of measuring atmospheric absorption. This method calculates absorption as the residual of four large fluxes which nearly cancel. Thus, the relative error is large. This method often results in negative absorption in the presence of cloud inhomogeneity as seen by Herman (1977).

As stated in the quote from Herman (1977) at the beginning of Chapter 1, "clearly, more sophisticated radiometric techniques are required to resolve the cloud absorptance question."

2.5 Absorption Theory

In addition to observational or model error in the parameterization of observed atmospheric states, it is possible that the cause of the measured anomalous absorption lies in a physical misunderstanding of the effects of aerosol, gas, and/or cloud. The purpose of this section is to review past research into these effects and to determine their theoretical magnitude.

2.5.1 Aerosol Absorption

Even in the most pristine atmospheres, aerosol plays a role in the absorption of solar radiation. As a first order statement about the effects of aerosol on atmospheric

absorption, Liou and Sasamori (1975) show an increase with aerosol load and solar zenith angle increase. This is straightforward: more absorbers in the atmosphere and longer path lengths associated with a large solar zenith angle results in more attenuation. Liou and Sasamori conclude that aerosol enhances clear sky absorption by 3 to 8%. Likewise, in a cloudy atmosphere, Herman and Curry (1984) show that aerosol can enhance absorption by approximately 1 to 5% over that due solely to cloud droplets and water vapor.

Grassl (1975) addresses the issue that aerosol can be incorporated into cloud drops as a mixture and/or remain interstitial in the air between the drops. It is concluded that there is almost no difference between the two states of aerosol in terms of absorption and that within clouds the effectiveness of aerosol is increased. This is evidenced by observations of lower cloud albedo in polluted industrial areas compared to areas where the aerosol load is much smaller. However, it is also concluded that the vertical distribution of aerosol also plays a role. For example, a dense aerosol layer underlying a thick cloud can only absorb a small fraction of the solar flux as a result of the low transmissivity of the cloud.

Twomey (1972) performed a modeling study that investigated the effects of aerosol embedded in a non-absorbing cloud. He finds that aerosol absorption decreases with increasing solar zenith angle when the aerosol is embedded in thick clouds. At large solar zenith angles, photons tend to escape from the cloud top relatively sooner than they would for normal incidence. It is stated that the effect of aerosol is large enough that it must be accounted for in modeling studies, but too small to explain the cloud absorption anomaly.

2.5.2 Gas Absorption

The gas that absorbs the largest percentage of incoming solar radiation is water vapor. The importance of water vapor absorption has been reported to various degrees in the literature. For example, Stephens (1978a) presents results which show that water vapor absorption is of the same order of or greater than cloud absorption depending on cloud location and LWC. However, Welch et al. (1980), Slingo and Schrecker (1982), and Herman and Curry (1984) present results which show weak water vapor absorption relative

to cloud absorption. Slingo and Schrecker (1982) point out that the differences between these results are due to different relative amounts of water vapor and cloud liquid water.

In addition to gas amount, gas absorption is dependent on the path lengths of photons through the atmosphere. Hence, anything that changes photon path lengths will change gas absorption. For instance, cloud and aerosol scattering redistributes radiation in such a way that photon path lengths are changed. Lacis and Hansen (1974) show higher water vapor absorption in cloudy sky than in clear sky as a result of increased path lengths caused by multiple scattering in the cloud. However, Slingo and Schrecker (1982) point out that increased path lengths due to multiple scattering in cloud may not be sufficient to counteract the loss of a large fraction of the solar beam due to reflection off cloud top. Hence, they show less gas absorption in cloudy sky.

In reference to the anomalous absorption controversy, Hignett (1987) show that water vapor must be increased by a factor of three and ozone must be removed from the atmosphere for the simulation to match the observations. This is far outside of the uncertainty bounds of the gas amount.

2.5.3 Cloud Absorption

The absorption of cloud droplets is described by the solution of the electromagnetic wave equation. This is also known as Mie theory. The absorption of cloud drops is wavelength dependent and varies with droplet size and purity. The ensemble absorption of cloud droplets in a cloud and resulting cloud albedo are strong function of LWP and solar zenith angle (Liou and Whitman, 1979). In addition, Slingo and Schrecker (1982) note that absorption and albedo are only weakly dependent on the drop size distribution.

Although the dependence of absorption and albedo on drop size distribution is weak, the dependence on r_e seems to be more important. Because the presence of large drops can be missed by instruments, Wiscombe et al. (1984) questioned the omission of large drops from model cloud distributions. Several studies show that increasing r_e leads to lower albedo and increased absorption (see Twomey, 1976; Stephens, 1978a; Liou and

Whitman, 1979; Welch et al., 1980). Ackerman and Stephens (1987) also note that the inclusion of large drops in thin clouds has the reverse effect.

2.5.4 The Effect of Cloud Heterogeneity

The most common speculation as to the source of anomalous absorption is the effect of cloud heterogeneity (i.e. Twomey and Cocks, 1982; Herman and Curry, 1984; Foot, 1988). This speculation is valid because, as mentioned in the model input error discussion above, several studies have shown the importance of cloud morphology on reflected and transmitted flux through a cloud layer. However, the effect on solar absorption is less well known. This results from the lack of high spectral resolution models and, until recent years, broadband multidimensional radiative transfer theories. Davies (1978) uses an analytical model to simulate flux and absorption in an atmosphere containing an isolated cuboidal cloud. It is noted that flux out the cloud sides may significantly deplete flux out cloud top and base leading to spurious absorption. This is the problem that the correction method of Ackerman and Cox (1982) tries to solve. Davies (1978) also finds that ignoring the illumination of cloud sides leads to errors which can be large even for small width to height ratios. These errors increase with increasing solar zenith angle.

In a study by Davis et al. (1979), it is shown that total column absorption is nearly independent of cloud type if fractional cloud cover is accounted for properly. Because cloud cover projected onto the normal to the direct solar beam is larger than actual cloud cover, it is determined that fractional cloud cover should be increased by $(1+tan\Theta)$ where Θ is the solar zenith angle. However, this approximation is only valid when cloud height to width ratios are near one and clouds are spaced far enough apart so that cloud to cloud interactions are negligible.

Apart from total atmospheric absorption, Stephens (1988a) shows a change in cloud absorption with changes in cloud morphology. Using a semi-analytical radiative transfer theory, it is shown that a Gaussian cloud absorbs less than a plane-parallel cloud with the same total optical depth. He notes that the effect of cloud heterogeneity can be large and more important than the effects of microphysics.

Cloud heterogeneity also has an effect on indirect methods of inferring anomalous absorption. Byrne et al. (1996) finds that half of the discrepancy between observed and calculated surface to TOA cloud forcing ratio f_s and slope of transmission versus albedo β can be explained by broken clouds. Thus, the inability of general circulation models to account for cloud heterogeneity is responsible for a portion of this discrepancy, not an unknown absorption process.

If cloud heterogeneity is the cause of anomalous absorption, Stephens and Platt (1987) and Stephens and Tsay (1990) note that its effect must vary with wavelength and be more pronounced at wavelengths where absorption is strong.

2.6 Results From the ARESE IOP

Two studies have recently been published presenting results from the ARESE IOP. The first, Zender et al. (1997), use radiometric measurements at the ARM CART site and periodic colocations with the Egrett aircraft to compare observed and simulated surface insolation, column albedo, and column absorption. The results of this comparison are shown in Fig. 2.5 for the cloudy sky case on 30 October 1995. While simulations of the clear sky cases on 11 and 15 October are near observed values, model results show an overestimation of surface insolation and albedo and a corresponding underestimation of atmospheric absorption for the overcast case. It is stated that the albedo and surface insolation results alone provide indirect evidence of anomalous absorption. First, an overestimation of albedo implies the model cloud is too thick. Thinning the cloud to match the observed albedo would decrease cloud particle absorption and increase the absorption discrepancy. Second, thinning the cloud would cause modeled surface insolation to increase. However, the modeled surface insolation is already too high as indicated in Fig. 2.5. Third, because both albedo and transmission are too high for cloudy conditions, this implies that there is a deficit of absorption in the model atmosphere.

Zender et al. also use the slope of transmission versus albedo β and shortwave cloud forcing ratio f_s to infer excess atmospheric absorption. Their results for colocation events

are listed in Table 2.1. These differences are consistent with those presented by Cess et al. (1995) and Ramanathan et al. (1995).

Table 2.1: Summary of modeled and observed β and f_s (adapted from Zender et al., 1997).

	observation	model
β	0.58	0.71-0.73
f_s	1.46-1.50	1.12-1.14

A second study performed by Valero et al. (1997) shows similar increases in column absorption under cloudy conditions. They present results for clear sky (11 October), scattered clouds (19 October), broken clouds (13 October), and overcast (30 October). All calculations were made using Egrett and Otter aircraft data flying above and below cloud, respectively. The observed and simulated absorptions for each day calculated using the net flux differencing technique are shown in Fig. 2.6. Whereas modeled absorptions range only from about 13% to 16%, observed absorptions range from 15% for clear sky to 36% for overcast sky. Sampling errors are said to be non-existent because spectral measurements of absorption at 0.5 μm converge to 5% for all cases. Therefore, the correction method of Ackerman and Cox (1982) is not needed.

2.7 Summary

This chapter has presented a brief history of absorption and albedo discrepancy between observations and simulations. This discrepancy has been reported to various degrees including model overestimation of atmospheric absorption. The main conclusion to be drawn from these results is that there appears to be no systematic trend in the occurrence of excess absorption. However, recent results from the ARESE IOP indicate that cloudy atmospheres do absorb more solar radiation than present models can predict and that this absorption is proportional to cloud amount.

Reasons for absorption and albedo discrepancy and, perhaps, the non-existence of a trend in past research was discussed in terms of instrument error, model input error, inaccurate absorption theory for aerosol, gas, and cloud, and the unresolved effect of

cloud heterogeneity. Of all these possibilities, the effect of cloud heterogeneity is the least well understood. Though several studies have investigated the reflection and transmission of solar radiation through heterogeneous clouds, they have not looked at the effect of heterogeneity on absorption. Furthermore, they have been confined to a few wavelengths or been limited to a calculation of broadband flux without spectral resolution. The rest of this study is devoted to the creation of a three-dimensional model which has high spectral resolution across the shortwave solar spectrum and its use in providing more information about how heterogeneous atmospheres redistribute radiation. In addition, the ARESE case studies will be revisited to determine if the new information provided by this model aids in the understanding of the observations.

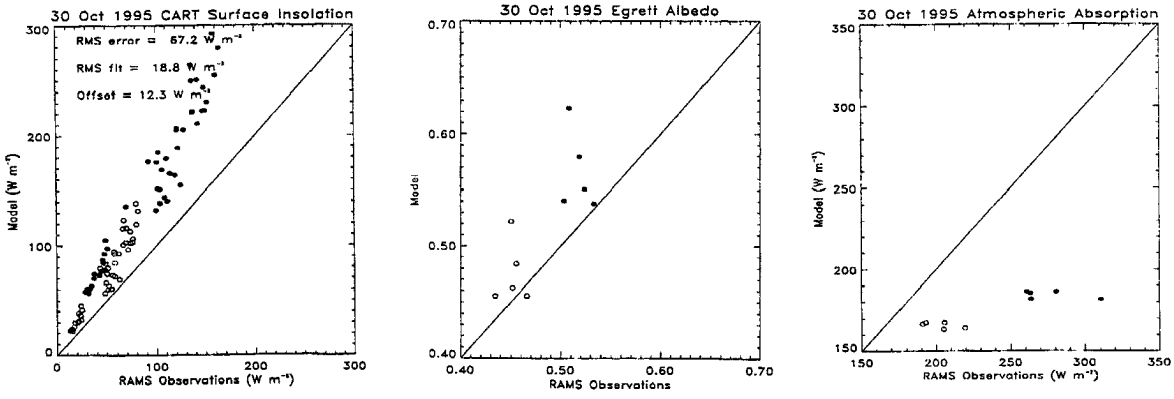

Figure 2.5: Observed and modeled instantaneous surface insolation, albedo, and absorption for 30 October 1995. Solid circles indicate total shortwave and open cirles indicate NIR (adapted from Zender et al., 1997).

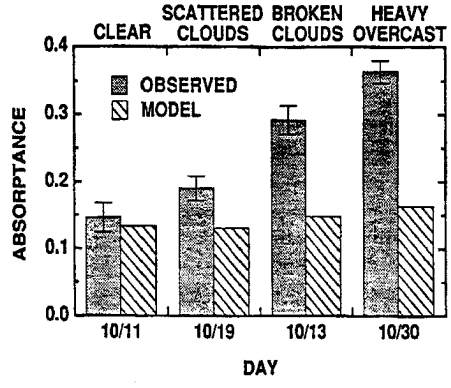

Figure 2.6: Comparison of the observed and modeled column absorptance for 4 days (from Valero et al., 1997)

Chapter 3

REQUIRED ATMOSPHERIC RADIATIVE TRANSFER THEORY

3.1 Introduction

In this chapter, the principles of atmospheric radiative transfer pertinent to this study are discussed. To begin, the optical parameters which describe the physical interactions between photons and atmospheric constituents are introduced. Next, the radiative transfer equation as it applies to horizontally homogeneous scattering atmospheres in the shortwave solar region of the spectrum is described.

3.2 Basic Optical Properties

The atmosphere consists of several general constituents which scatter and/or absorb radiation. These constituents include aerosol, gas, and cloud particles. For this research, the effects of aerosol are neglected so that the redistribution of solar radiation due to cloud heterogeneity in a gas atmosphere can be concentrated on. Both gas and cloud absorb and scatter radiation and their properties are combined for use in plane-parallel models. However, as will be discussed later, the Monte Carlo model used for this study keeps the bulk parameters that describe these constituents separate.

3.2.1 The Gaseous Atmosphere

At solar wavelengths, the most radiometrically important gases in the earth's atmosphere are water vapor (H_2O), ozone (O_3), carbon dioxide (CO_2), and oxygen (O_2). The mixing ratio q of H_2O and O_3 for the standard mid-latitude summer atmosphere are shown in Fig. 3.1. The units are in g/g (the ratio of the mass of the individual gas to that of dry air). The mixing ratio for CO_2 and O_2 are constant throughout the atmosphere at 5.013×10^{-4} and $.2314\, g/g$, respectively. Gas is considered to be horizontally homogeneous

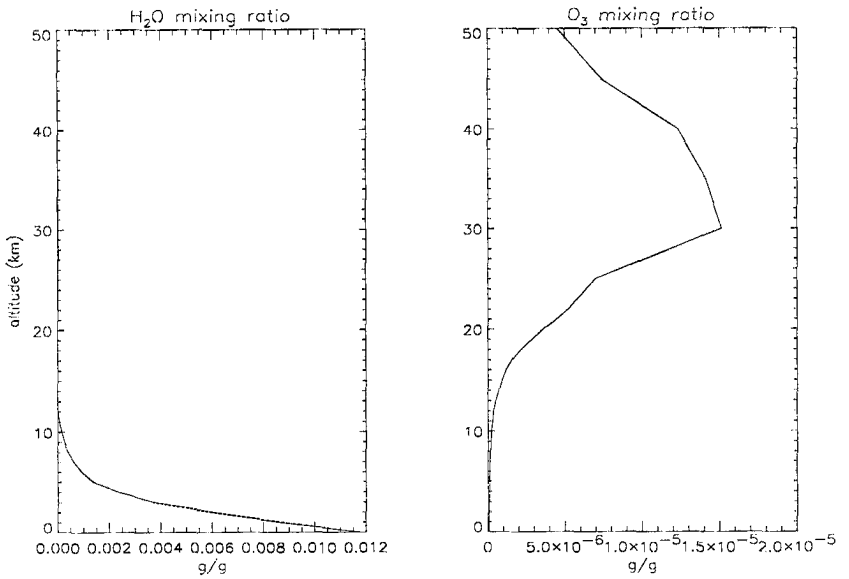

Figure 3.1: Mixing ratios for H_2O and O_3 for the standard mid-latitude summer atmosphere.

or plane-parallel, but as seen in Fig. 3.1 can be vertically inhomogeneous. For most model applications, gas profiles are divided into layers of constant gas mixing ratio.

Molecules in the atmosphere scatter and absorb radiation. Rayleigh scattering describes scattering by N_2 and O_2 and is reasonably represented by the following empirical function from Paltridge and Platt (1976):

$$\tau_{ray} = .0088\nu^{(-4.15+0.2\nu)}e^{(-0.1188H-0.00116H^2)} \tag{3.1}$$

which calculates Rayleigh optical depth. Here, ν is wavelength and H is altitude in km. Rayleigh optical depth is actually the integration of the Rayleigh scattering coefficient $\sigma_{ray,sca}$ (km^{-1}) from TOA to the altitude H. The scattering coefficient determines the mean path length of a photon $(1/\sigma_{sca,ray})$ before it is scattered. The Rayleigh scattering coefficient, and therefore optical depth, varies in a well known way with wavelength as shown in Fig. 3.2. After a photon scatters, its new direction is governed by the phase function $P(cos\theta)$ where θ is the scattering angle. The phase function is normalized over the range of $cos\theta$ from -1 to 1:

$$\frac{1}{2}\int_{-1}^{1} P(cos\theta)d\cos\theta = 1 \tag{3.2}$$

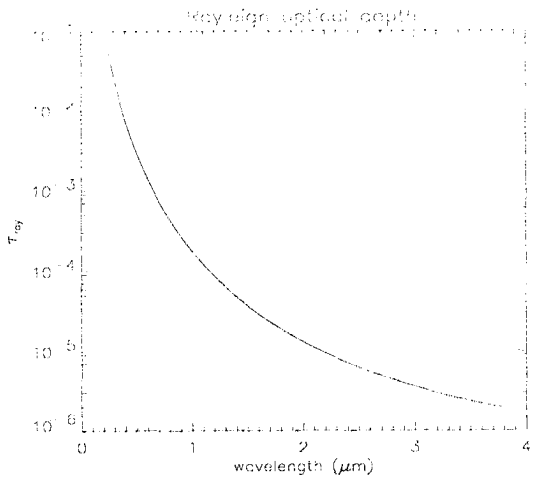

Figure 3.2: Rayleigh optical depth for the atmosphere layer between 50 and 0 km as a function of wavelength

The phase function can be partially described by the asymmetry factor g:

$$g = \frac{1}{2}\int_{-1}^{1} cos\theta P(cos\theta) d\cos\theta \tag{3.3}$$

This is a measure of the probability that a photon will be scattered into the forward or backward hemispheres. A value of 1 means complete forward scatter and a value of -1 complete backscatter. The parameter g is also referred to as the effective asymmetry factor g_{eff}. The Rayleigh phase function is analytic and described by the relation:

$$P(cos\theta) = \frac{3}{4}(1 + cos\theta^2) \tag{3.4}$$

For Rayleigh scattering, g_{eff} is 0 because a photon has an equal probability of being scattered in the backward or forward hemisphere.

Attenuation of radiation due to gas is defined by the gas absorption coefficient k which has units km^{-1}. Here, k depends on the pressure, temperature, and amount of gas in the layer. The amount of absorption that takes place as a beam of radiation or a packet of photons travels through a gas is determined by Beer's law of transmission:

$$T = e^{-kl} \tag{3.5}$$

where T is the transmission and l is the geometric path length (km) of the radiation. The quantity kl is often referred to as the gas optical path λ_{gas}. The integrated absorption

coefficient for a vertical path length from the top of the gas atmosphere to the bottom is the gas optical depth τ_{gas}. For a homogeneous layer of gas, $\tau_{gas} = k\Delta z$.

In practice, the absorption coefficient k is defined at a reference pressure and temperature for a particular gas and does not depend on the amount of that gas in the atmosphere. In this case, k has the units $cm^2 \cdot g^{-1}$. The density of the gas (ρ_{gas}) is accounted for in the optical mass u which has units $g \cdot cm^{-2}$. Here, $u = \rho_{gas} l$. Beer's law is rewritten in terms of the optical mass and k. Because geometric path length information will be obtained from the Monte Carlo model described in the next chapter, u is expressed in terms of its the geometric path length, l. In this case, the transmission of radiation through a gas atmosphere becomes:

$$T = e^{-ku} = e^{-k\rho_{gas} l} \tag{3.6}$$

There are many methods available to determine the value of k. For this study, the k-distribution approach is employed and will be explained in Chapter 5.

3.2.2 Cloud Particles

Like gas extinction, σ_{ext} describes the loss of the direct beam of radiation due to absorption and scattering along the beam's path. The cloud extinction coefficient is defined as:

$$\sigma_{ext} = \sigma_{abs} + \sigma_{sca} \tag{3.7}$$

where σ_{abs} is the cloud absorption coefficient and σ_{sca} is the cloud scattering coefficient. All have units of km^{-1}. The cloud optical depth τ_{cld} is then the integration of σ_{ext} along a vertical path from the top to the bottom of the cloud. For a homogeneous cloud layer, $\tau_{cld} = \sigma_{ext}\Delta z$.

The amount of radiation a cloud particle scatters is described by the ratio of σ_{sca} to σ_{ext}:

$$\omega_o = \frac{\sigma_{sca}}{\sigma_{ext}} = \frac{\sigma_{sca}}{\sigma_{sca} + \sigma_{abs}} \tag{3.8}$$

ω_o is referred to as the single scatter albedo. The single scatter albedo can also be described as the probability that a photon will scatter off a cloud particle rather than being absorbed. The absorption of the cloud droplet is therefore $(1 - \omega_o)$.

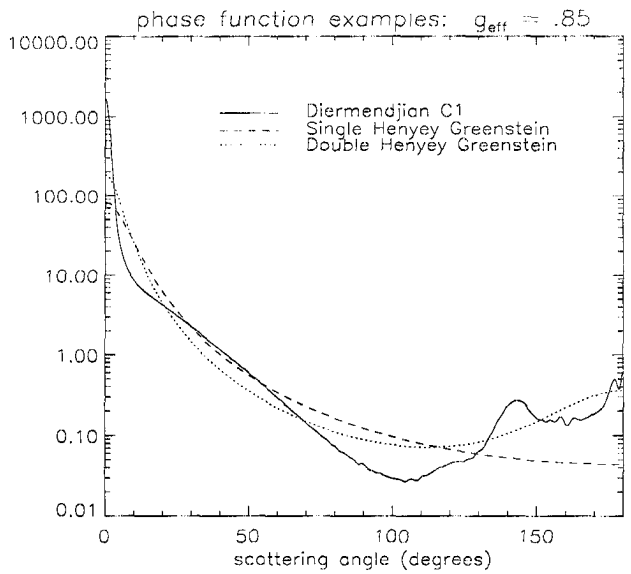

Figure 3.3: Phase function examples including the Diermendjian C1, single and double Henyey-Greenstein. All have an effective asymmetry parameter $g_{eff} = .85$

Like Rayleigh scattering, the direction of a photon after collision with a cloud droplet is governed by a phase function $P(cos\theta)$. The Deirmendjian C1 phase function, typical for a water droplet and derived from Mie particle scattering theory, is shown in Fig. 3.3 (solid curve). The large forward peak indicates a high probability of a photon being scattered directly ahead. For use in models, the phase function is usually parameterized. Parameterizations are employed because they are easily incorporated into radiative transfer models. In addition, radiative flux is not very sensitive to details of the phase function, so a simpler phase function can be used without sacrificing accuracy. The most common parameterization is the Henyey-Greenstein (HG) formulation:

$$P_{HG}(cos\theta) = \frac{1-g^2}{(1+g^2+gcos\theta)^{3/2}} \tag{3.9}$$

An example is shown by the dashed curve in Fig. 3.3. This is called a single Henyey-Greenstein phase function because it has a single peak in the forward direction. As will be seen later, the Monte Carlo model used in this study can accommodate a highly detailed phase function like the Diermendjian C1, however use of the Henyey-Greenstein formulation increases flexibility as it is easily derived for any g_{eff}. One modification to the single Henyey-Greenstein phase function to more closely represent a real phase function is

the inclusion of the backscatter peak. This is called the double Henyey-Greenstein (DHG) phase function and is created using the following relation:

$$P_{DHG}(cos\theta) = b \cdot P_{HG}(cos\theta, g_1) + (1-b) \cdot P_{HG}(cos\theta, g_2) \tag{3.10}$$

where $g_1 = g_{eff} + 0.05$ and $g_2 = -0.6$. The parameters g_{eff}, g_1, g_2, and b are related in the following way:

$$g_{eff} = b \cdot g_1 + (1-b) \cdot g_2 \tag{3.11}$$

An example of the DHG phase function is also shown in Fig. 3.3 (dotted curve). The Diermendjian C1, single and double Henyey-Greenstein phase functions have the same $g_{eff} = 0.85$.

The optical properties σ_{ext}, g_{eff}, and ω_o are all cloud type specific because they are determined from the phase, size, and concentration of cloud particles. The above properties are also wavelength dependent as can be seen in Fig. 3.4. Plotted are the extinction coefficient, asymmetry parameter, and single scattering albedo for a Stratocumulus I (ScI) cloud which has a liquid water content of 0.14 gm^{-3}, a droplet concentration of 350 drops per cm^3, and a mode radius of 3.5 μm. These optical properties were calculated using Mie theory and are listed for several water cloud types in Stephens (1979). This is the primary cloud type used in this study.

3.3 The One-Dimensional Radiative Transfer Equation

For most applications including general circulation modeling, the one dimensional radiative transfer equation is used because it is relatively simple and computationally faster than other theories while still retaining a physical basis. The one dimensional aspect of the model assumes that the model atmosphere is plane-parallel and azimuthally independent. Vertical inhomogeneity, however, is accounted for. The radiative transfer equation using the above assumptions can be formulated as:

$$\mu \frac{dI(\tau,\mu)}{d\tau} = -I(\tau,\mu) + \frac{\omega_o}{2} \int_{-1}^{1} P(\mu,\mu') I(\tau,\mu') d\mu' + S_{sw}(\tau) \tag{3.12}$$

where $I(\tau,\mu)$ is the radiance at a level τ in the atmosphere in a direction μ. The first term on the right hand side is the loss of energy through the atmosphere boundaries and the

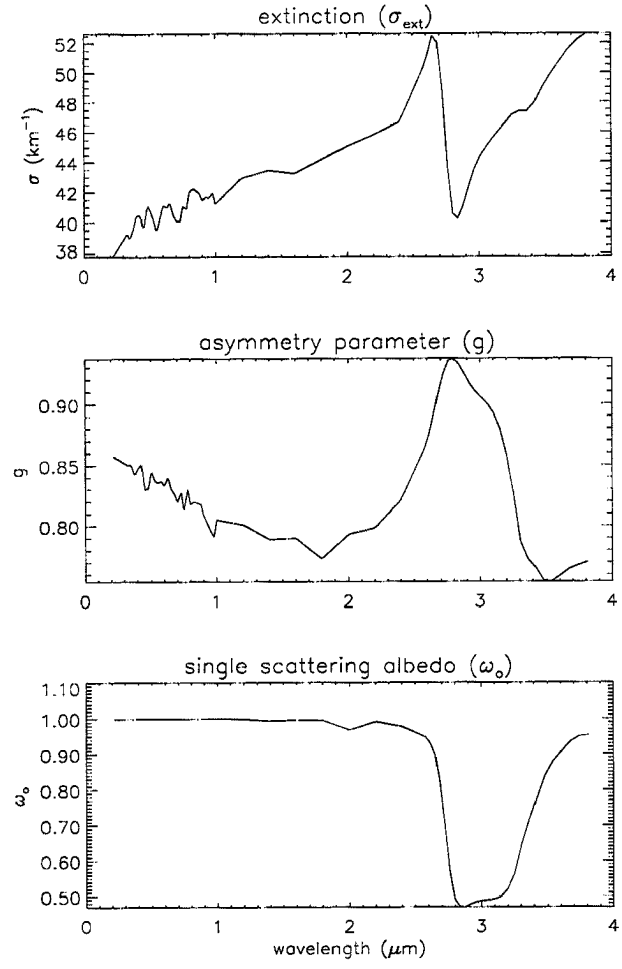

Figure 3.4: Optical properties of a stratocumulus I (ScI) cloud as computed by Stephens (1979).

second term represents contribution to the radiance from multiple scattering processes. The cosine of the scattering angle $cos\theta$ is related to the photon zenith angles μ and μ' by:

$$cos\theta = \mu\mu' + (1-\mu^2)^{\frac{1}{2}}(1-\mu'^2)^{\frac{1}{2}} \tag{3.13}$$

where μ' is the cosine of the angle of the incoming photon and μ is the cosine of the angle of the emergent direction. $S_{sw}(\tau)$ is referred to as the "pseudo source" term and describes the contribution to the radiance by the single scatter of the direct beam at a location τ in the atmosphere:

$$S_{sw}(\tau) = \frac{\omega_o}{4\pi} F_o P(\mu, \mu_o) e^{\frac{-\tau}{\mu_o}} \tag{3.14}$$

Here, F_o is the incident solar flux at TOA and μ_o is the cosine of the solar zenith angle.

There are several methods of solving or approximating the solution to the one-dimensional radiative transfer equation. As noted in Chapter 1, this study employs the Monte Carlo method for computing radiative quantities in a model atmosphere. As validation, test results from this model are compared to those from a model that solves the radiative transfer equation using the adding-doubling method. This method of solution is well described in Stephens and Greenwald (1988) and Liou (1992). The adding-doubling model employed is also referred to as a 32-stream model because it computes radiances for 16 directions in the upwelling and downwelling hemispheres. These radiances are converted to flux for each hemisphere using the relation:

$$F(\tau) = 2\pi \int_0^1 I(\tau, \mu)\mu d\mu \tag{3.15}$$

3.4 Summary

In this chapter, the optical properties which determine the transfer of solar radiation through the atmosphere have been discussed. For this study, the absorption of radiation by gas and cloud is considered. This is described by the parameters k and $(1-\omega_o)$, respectively. The absorption of the surface was not discussed but is analogous to ω_o. The surface albedo α describes the amount of radiation that is reflected by the surface. Therefore, the amount of radiation absorbed by the surface is $(1-\alpha)$.

If radiation is not absorbed, scattering occurs. The direction of scatter is described by the Rayleigh or cloud phase function. Scattering off the surface is assumed to be isotropic, i.e. all directions of scatter in the upwelling hemisphere have equal probability of occurring. All of the above parameters are functions of wavelength.

In the next chapter, the use of these optical properties in the Monte Carlo method will be presented.

Chapter 4

THE MONTE CARLO MODEL

4.1 Introduction

As the scattering properties of a model atmosphere become increasingly complex, traditional approaches to solving the radiative transfer equation become less practical. This study investigates the effects of cloud heterogeneity, a property of the scattering atmosphere that is not easily accounted for in analytical and numerical plane-parallel models. One such way of dealing with this in a plane-parallel model is to use average cloud properties (such as optical depth) while still using a plane-parallel framework. A second method is to use a parameterization involving cloud fraction. The model is run twice, once for the homogeneous cloudy sky condition and a second time for the clear sky condition. The two results are then combined depending on the desired percent cloudiness. These methods, however, do not simulate the complex paths that photons take when interacting with a three-dimensional or heterogeneous cloud. This can lead to errors in reflection, transmission and absorption of solar radiation. Other methods of accounting for cloud heterogeneity including extending the radiative transfer equation to three dimensions exist, but these are computationally demanding and often speak to certain kinds of geometry.

The most straightforward method of modeling radiation that interacts with such a complex medium is to actually trace the path of each individual photon. This is the Monte Carlo approach to radiation modeling. By firing thousands of model photons into a medium and observing their paths and destinations, a Monte Carlo model returns a statistical result for the quantity of interest: radiative flux. This type of modeling has been used for radiation field investigations in oceanography, nuclear physics, and atmospheric

science. The following sections describe the Monte Carlo method and the model used in this study.

4.2 Integration Using the Monte Carlo Method

The Monte Carlo method is a well known tool which is used for the evaluation of complex integrals. Named for the gambling casinos of Monte Carlo, this approach is based on chance: the generation of random numbers to estimate the answer to the integral. Take, for example, a function $f(x)$ which is contained in a region R (Fig. 4.1). To calculate the integral of $f(x)$ (which is the area under the curve) using the Monte Carlo method, we introduce points into R at random locations. The area under the function is simply the probability that a particular point will be placed under $f(x)$. Thus, in Fig. 4.1, the estimate of the area under $f(x)$ after ten guesses is $\frac{6}{10}$ or .6 times the area of the box. As more points are introduced into the region, the estimate will converge to the true answer.

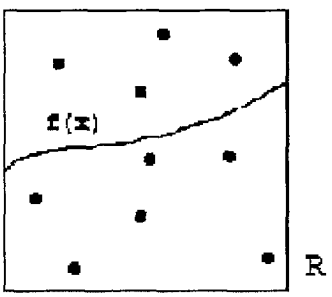

Figure 4.1: Simple Monte Carlo evaluation of an integral

The immediate goal of the Monte Carlo radiative transfer model developed for this study is to calculate the ratio of the number of photons which leave the atmosphere to the number of photons which were fired into it. For calculations at solar wavelengths, this is a measure of the normalized emergent flux. The model derived for this research accommodates cloud scattering and absorption as well as surface reflection. Gas absorption is accounted for outside of the Monte Carlo model using the Equivalence Theorem, a topic which will be discussed in the next chapter.

4.3 A Simple Monte Carlo Model

Consider for simplicity a plane-parallel layer of cloud droplets which occupies a three-dimensional space that can scatter and absorb radiation. A standard right-hand x, y, z coordinate system is used. The measurements we are interested in are the emerging fluxes out the top and bottom of the layer. The number of photons which emerge from the top or bottom of the layer is dependent upon how many photons are absorbed and direction of emergence as determined by the scattering properties of the medium. The Monte Carlo technique employs a very simple routine of following each photon from scattering point to scattering point until it is absorbed or exits the layer. A good description of the simulation of the transfer process in a Monte Carlo model is found in Chapter 2 of Marchuk et al. (1980). The following is a step-by-step description of this process.

1. Each photon begins its journey at a piercing point on top of the model atmosphere (x_0, y_0, z_0). The location of the point is chosen from a uniform random distribution over the x y domain of the model atmosphere. The photon's direction is determined by the solar zenith and azimuth angles and is expressed in terms of the direction cosines (i_0, j_0, k_0).

2. From the piercing point, the free path of the photon is chosen. This is the distance traveled in the medium to the first scattering point. If the free path is long enough, the photon will exit the scattering atmosphere. For a homogeneous atmosphere, the free path is calculated by choosing a random transmission between 0 and 1. This random transmission is translated to physical distance in the medium using the cloud extinction coefficient σ. According to Beer's law of transmission, the transmission T of the photon is:

$$T = e^{-\sigma l} \tag{4.1}$$

where l is the distance the photon traveled. For this application, a random transmission is chosen and l is calculated:

$$l = -\frac{1}{\sigma} \ln T \tag{4.2}$$

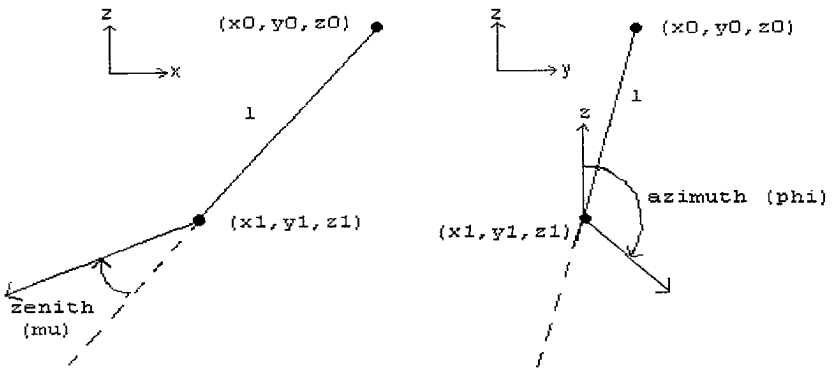

Figure 4.2: Scattering geometry example. Shown are two views of the event, one in the x-z plane to illustrate the zenith angle μ and the other in the y-z plane to illustrate the azimuth angle ϕ.

A value of 0 means the photon will travel 0 distance and a value of 1 means it will travel an infinite distance. Using the distance traveled l, the coordinates of the endpoint of the path (x_1, y_1, z_1) are calculated:

$$\begin{aligned} x_1 &= x_0 + i_0 l \\ y_1 &= y_0 + j_0 l \\ z_1 &= z_0 + k_0 l \end{aligned} \tag{4.3}$$

3. If the new coordinates lie inside the medium, the photon is either absorbed or scattered at (x_1, y_1, z_1). The absorption is determined by the single-scattering albedo ω_o which ranges from 0 to 1. If a random number is less than ω_o, the photon is absorbed and the model starts over with a new photon in step 1. The photon is scattered if it is not absorbed. Fig. 4.2 shows the geometric setup for the scattering scenario. The azimuth ϕ of the new trajectory is simply a random number between 0 and 2π. The zenith angle μ is determined by the cloud particle phase function cumulative density function (cdf). The cdf monotonically increases from 0 to 1 and the rate of increase is determined by the shape of the phase function. A typical water cloud phase function and its cdf are displayed in Fig. 4.3. A random number from 0 to 1 is chosen and located on the cdf curve. The new zenith angle of the photon is the angle associated with the random number. Using ϕ and μ, the new direction cosines

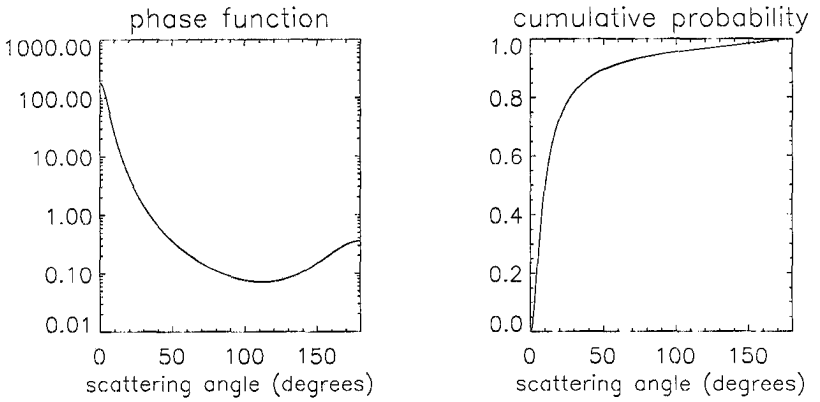

Figure 4.3: Double Henyey-Greenstein phase function and its associated cumulative density function, $g_{eff} = .85$

are then calculated from relationships found in Marchuk et al. (1980):

$$
\begin{aligned}
i_1 &= i_0\mu - (j_0 sin\phi + i_0 k_0 cos\phi)\left[\frac{1-\mu^2}{1-k_0^2}\right]^{\frac{1}{2}} \\
j_1 &= j_0\mu + (i_0 sin\phi - j_0 k_0 cos\phi)\left[\frac{1-\mu^2}{1-k_0^2}\right]^{\frac{1}{2}} \\
k_1 &= k_0\mu + (1-k_0^2)cos\phi\left[\frac{1-\mu^2}{1-k_0^2}\right]^{\frac{1}{2}}
\end{aligned}
\tag{4.4}
$$

4. Steps 2 and 3 are repeated until the photon is absorbed or leaves the medium. If the photon leaves the upper or lower boundary, it is counted as a contribution to the upwelling or downwelling flux. If the photon leaves the lower boundary and a reflecting surface is present, the photon's survival is once again left to chance. If a random number between 0 and 1 is lower than the surface albedo α, the photon will reflect back into the atmosphere. The new direction of the photon is calculated as it is for particle scattering. However, the direction of travel is restricted to the upwelling hemisphere and the surface used in the present model is assumed to be Lambertian. Photons reflected off a Lambertian surface have an equal probability of being reflected into the upwelling hemisphere with any azimuth and any $/mu$.

4.4 The Monte Carlo Model Used for this Study

The Monte Carlo model used for this study uses the basic process described above with a number of modifications. These modifications serve to increase the flexibility, speed, and accuracy of the model.

4.4.1 Measurement Levels

The quantities of interest for this study are upwelling and downwelling flux above and below a cloud layer. The altitude in the model atmosphere at which these measurements are made can vary from case to case. Therefore, to obtain these quantities the photons are counted every time they cross a measurement level in a particular direction. They are added as a contribution to the upwelling or downwelling flux at that level. The model atmosphere is horizontally periodic. Therefore, if a photon leaves one side of the atmosphere, it is reintroduced in the opposite side.

4.4.2 Cloud Heterogeneity

The process explained above applies to a homogeneous cloud layer. The mean free path derived from (4.2) uses an extinction coefficient which is assumed not to change along the photon's path. For a heterogeneous medium, the extinction coefficient can vary a great deal and (4.2) no longer holds. This model employs a pixel based cloud grid which assumes each grid box is a homogeneous cube with a particular extinction. This setup is analogous to a dataset which might be returned from a cloud radar or a cloud resolving model. Each pixel contains an average retrieved extinction coefficient for that radar volume. To account for this type of heterogeneity a vector of summed optical path defined by the photon's direction to the cloud boundary is calculated. The summed optical path of a geometric path length l consisting of N segments each of length l (one through each cloud pixel) is just $\lambda_{tot}(l_n) = \sum_{n=1}^{N} \sigma_n l_n$. An example of this is shown in Fig. 4.4. The path of the photon takes it through four cloud pixels and therefore four different extinctions. The summed optical path of the photon is also shown.

The random transmission that was chosen is converted to an optical path using $\lambda_{rand} = -\ln T_{rand}$. The vector $\lambda_{tot}(l_n)$ is then linearly interpolated to find the distance traveled by the photon.

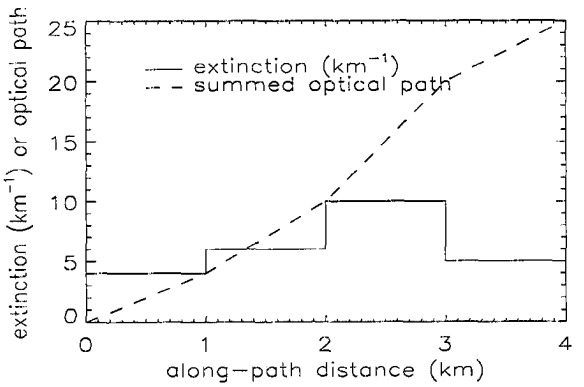

Figure 4.4: An example of the summed optical path for a photon which travels through 4 cloud pixels, each with a different extinction coefficient.

4.4.3 Rayleigh Scattering

As discussed in Chapter 3, photons can be scattered by gas. This scattering is treated in the same manner as cloud scattering. In addition to cloud extinction, the distance a photon travels is now also determined from the Rayleigh scattering coefficient $\sigma_{ray,sca}$. The task becomes one of determining whether the photon scatters off a cloud droplet or gas. A second random transmission is chosen for Rayleigh scatter and $\sigma_{ray,sca}$ is integrated and stored in a vector of Rayleigh optical path. Using the random transmission, the distance the photon travels is interpolated from the vector of optical paths as it is for cloud scattering. If the Rayleigh scattering distance is shorter than the cloud scattering distance, then Rayleigh scattering occurs. The inverse is true if cloud distance is shorter. The new direction of the photon is then determined from the cloud or Rayleigh phase functions. This method of determining cloud or Rayleigh scatter may not be exact and has not been rigorously derived. Although the method employed here does not lead to appreciable error, further study is required to determine a proper procedure.

4.4.4 Variance Reduction

Variance reduction is a technique which maximizes the speed and accuracy of a Monte Carlo model. When a photon is lost to cloud or surface absorption, The simple model described above must start over with a new photon. Eventually, the calculated fluxes

converge to the true answer. This convergence can be greatly accelerated if each photon is allowed to survive until it exits the top of the atmosphere (assuming a reflecting lower boundary is present) but carries with it a weight that describes the probability of survival from each interaction. Using this variance reduction method, the photon enters the medium with weight 1. At each scattering point, the weight is multiplied by the single-scattering albedo. If the photon hits the surface, its weight is multiplied by the surface albedo and it is sent back into the scattering atmosphere. This process continues until the photon escapes the top boundary. When a photon exits the lower boundary of the medium, its weight is saved as a contribution to the downwelling flux. Likewise, when a photon leaves the top boundary, its weight contributes to the upwelling flux. In effect, each photon becomes a "photon packet" carrying with it the ratio of photons that survive the journey to the total number of photons that start it.

As its name implies, this type of variance reduction constrains the error of the final answer and accelerates the convergence of the guesses to the true answer. Fig. 4.5 shows the convergence of reflected and transmitted fluxes using variance reduction to the true answer as obtained from a 32-stream adding-doubling model. It is seen that in addition to this variance reduction technique, the choice of random number generators also plays a role in model accuracy and convergence speed. Here, the more sophisticated random number generator (ran3 from Numerical Recipes) converges faster than the relatively simple generator uni, however the final values for each are within an acceptable error range.

4.5 Model Performance

Using the modifications discussed above to increase model flexibility, speed, and accuracy, the results of the Monte Carlo model were compared to those obtained from a 32-stream adding-doubling model. Use of the adding-doubling model restricted the cloud morphology to plane-parallel. However, it was assumed that if the optical path summation referred to in the preceding sections proved successful for a cloud in which each pixel contained the same extinction coefficient, it would work for a heterogeneous cloud as well.

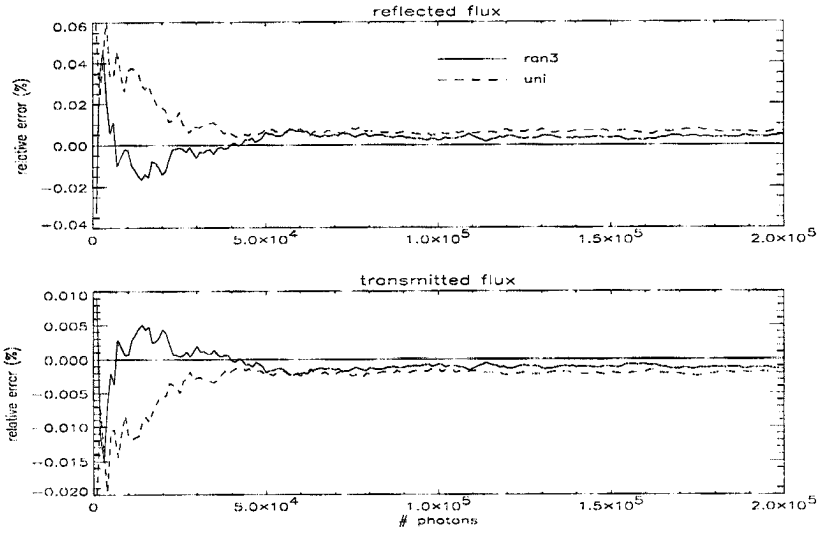

Figure 4.5: Convergence rate for the Monte Carlo model using two different random number generators. Relative errors are shown for a single layer cloud, $\tau = 5$, $g = .85$, and $\omega_o = 1$

The cloud and surface parameters chosen for the comparisons were intended to represent typical parameters that will be encountered in later experiments involving stratocumulus clouds. This range is mostly defined by observations of each parameter from field experiments and Mie theory. The model atmosphere is set up for a single cloud layer overlying a reflecting surface. The parameters which have the largest variations are optical depth τ and the cosine of the solar zenith angle μ_o. Because these parameters have such large variations, the comparisons of reflected and transmitted fluxes that were done between the Monte Carlo and adding-doubling models are shown as a function of τ and μ_o. The other parameters which defined the model setup are the effective asymmetry factor g_{eff}, single-scattering albedo ω_o, and the surface albedo α. For water clouds, g_{eff} is about .85 in the visible part of the shortwave spectrum. Although flux scales as g_{eff}, a double Henyey-Greenstein phase function was used to account for the backward peak in phase function observed in water clouds. The single scattering albedo ω_o is approximately 1 for this part of the spectrum, but a comparison using $\omega_o = .9$ was also done to show the Monte Carlo model can handle cloud absorption. α was chosen to be .2, a typical albedo over land.

The first experiment involved varying τ from 0 to 50, typical values expected in a stratocumulus cloud field. Here, μ_o was fixed at .866 or a 30 degree solar zenith angle. As seen in Fig. 4.6, the Monte Carlo results compare well to the adding-doubling reflected and transmitted flux for a conservatively scattering cloud layer ($\omega_o = 1$).

Similar results are seen when ω_o is changed to .9 in Fig. 4.7. At this value, the cloud can absorb radiation as observed in the decrease in reflected radiation as cloud optical depth increases. Again, the models compare favorably. The apparent scatter in the Monte Carlo reflected flux is similar in magnitude to the other plots, but it is emphasized by the magnification of the y-axis.

The flux comparisons were performed again, this time the cloud optical depth was fixed at 10 and the cosine of the solar zenith angle was allowed to vary. Figures 4.8 and 4.9 show the results for the $\omega_o = 1$ and $\omega_o = .9$ cases, respectively. Once again, the comparison is favorable for the entire range of μ_o.

4.6 Summary

In this section, the Monte Carlo method of integration was introduced and applied to solving radiative transfer problems. A simple Monte Carlo model for simulating reflected and transmitted radiative fluxes was described and extended to accommodate heterogeneous cloud fields and variance reduction techniques. By employing variance reduction, the model's speed and accuracy was increased. Finally, the performance of the Monte Carlo model was compared to that of a 32-stream adding-doubling model which showed favorable agreement. In the following chapter, the Equivalence Theorem method for accommodating gas absorption will be discussed.

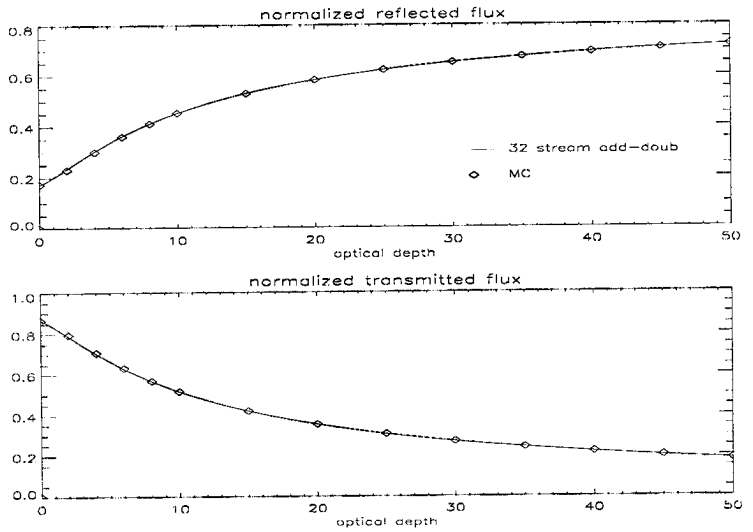

Figure 4.6: Flux comparisons between the Monte Carlo code and a 32-stream adding-doubling model: single layer cloud, $\mu_o = .866$, $g_{eff} = .85$ (double Henyey-Greestein), $\alpha = .2$, $\omega_o = 1$.

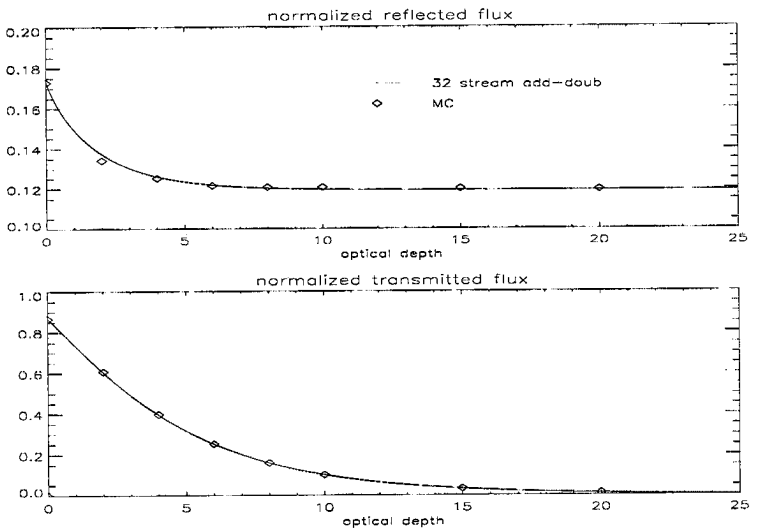

Figure 4.7: Flux comparisons between the Monte Carlo code and a 32-stream adding-doubling model: single layer cloud, $\mu_o = .866$, $g =_{eff} .85$ (double Henyey-Greestein), $\alpha = .2$, $\omega_o = .9$

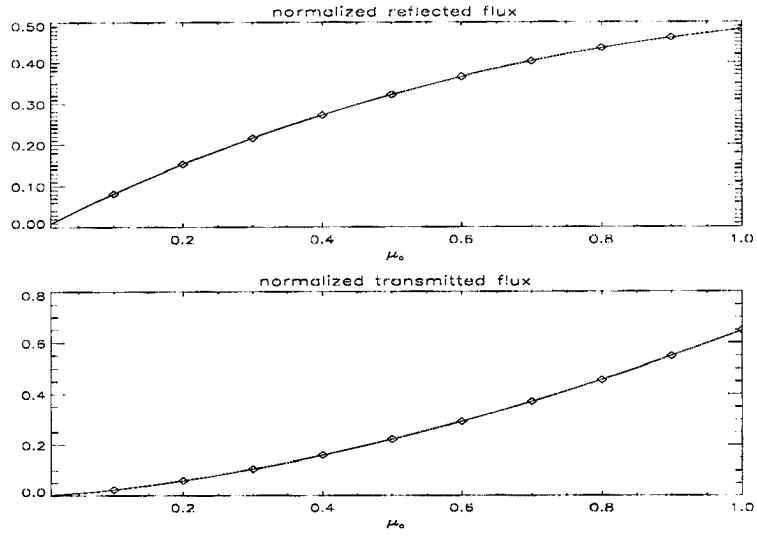

Figure 4.8: Flux comparisons between the Monte Carlo code and a 32-stream adding-doubling model: single layer cloud, $\tau = 10$, $g =_{eff} .85$ (double Henyey-Greestein), $\alpha = .2$, $\omega_o = 1$

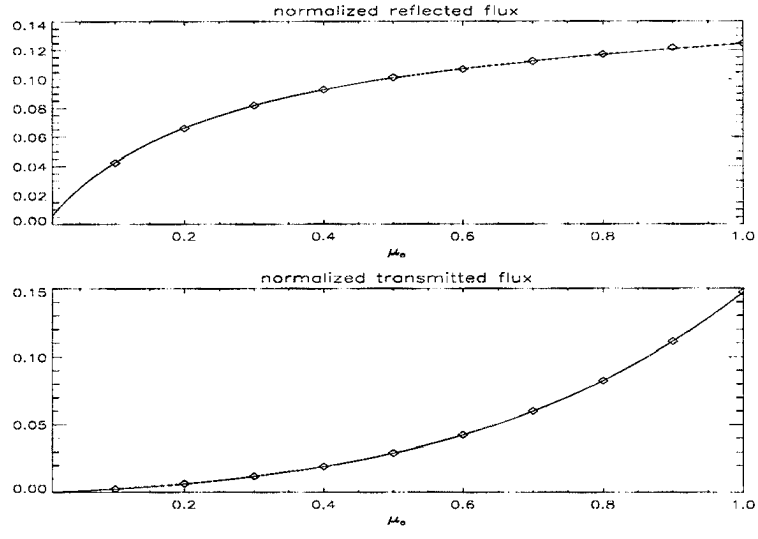

Figure 4.9: Flux comparisons between the Monte Carlo code and a 32-stream adding-doubling model: single layer cloud, $\tau = 10$, $g =_{eff} .85$ (double Henyey-Greestein), $\alpha = .2$, $\omega_o = .9$

Chapter 5

GASEOUS ABSORPTION

5.1 Introduction

In a simple Monte Carlo model which does not employ variance reduction techniques, gas absorption (like cloud absorption) determines whether a photon is attenuated in the atmosphere or is allowed to escape. In much the same way that free path is chosen in a cloud, the survival of the photon in the presence of gas absorption is left to choosing a random transmission. Once a transmission value is chosen, it is then determined whether or not the transmission to the boundary of the gas or the next scattering point along the photon's path is greater or less than this random value. If the transmission along the entire path is greater than the random value, the photon escapes the atmosphere or is allowed to scatter. If it is less than this value, the photon is considered attenuated in the atmosphere and the model starts over with a new photon.

When variance reduction is used, the attenuation of the photon along its path is dealt with in the same manner as cloud absorption or surface albedo. As described in the previous chapter, the single scattering albedo and surface albedo are accounted for in a weight. This allows the photon to continue through the atmosphere, carrying with it a probability of survival. Likewise, the photon's transmission due to gas absorption is multiplied to the photon's weight and represents its probability of survival as it travels through the gas.

The tool needed for the study of heterogeneous cloud effects is a broadband model that has high enough flux resolution to allow a spectral study of gas and cloud absorption. To achieve this type of resolution the model must be run once each time a cloud, gas or surface parameter is changed. The shortwave solar spectrum from .2 to 4 μm can

be subdivided into regions within which these parameters can be considered constant. Because cloud scattering properties do not vary to a large degree, the shortwave spectrum can be divided into a small number of spectrally constant cloud parameters. However, gas absorption varies greatly and it is the choice of these regions which determine the spectral flux resolution. Thus, the number of times the model must be run is dictated by the number of gas absorption regions that are used.

One of the most appealing aspects of the Monte Carlo model is its straightforward method of following each photon until it has left the atmosphere. However, the drawback to this technique is the fact that the model as described to this point must be run once every time a cloud or gas parameter is changed. Multiple gas optical depths can be accounted for in one run because, as mentioned above, the scattering properties of the cloud can be considered constant over certain spectral intervals. The attenuation of the photon due to gas along its path can be performed for each gas optical depth that occurs in the interval. This, on the other hand, requires a complex code that can keep track of the different gas parameters.

For this study, gas optical depths and resultant fluxes are calculated using the k-distribution technique. The data used consists of 287 spectral bands between .2 and 4 μm. The calculation of the flux in each band actually involves calculating the gas optical depth for several parameterized intervals in each band. For this k-distribution dataset, this mandates that the Monte Carlo model be run 12452 times to calculate the entire spectrum of spectral fluxes if no attempt is made to modify the code to perform multiple gas calculations for each constant cloud parameter interval. The time required to perform all calculations for a single model atmosphere in this case eliminates the feasibility of using the Monte Carlo technique for investigative studies. However, it is possible to run the Monte Carlo model without gas in the model atmosphere and then account for gas absorption afterward. This requires output of photon path length information from the model and is a modification of the Equivalence Theorem introduced by Irvine (1964). Thus, the model can be run only three or four times as mandated by the variations in cloud optical properties, saving time and ensuring model simplicity while maintaining full

theoretical rigor. In the following sections, the k-distribution method and its use with the Equivalence Theorem are described.

5.2 The K-Distribution Method

5.2.1 K-Distribution Theory

Within a spectral band $\Delta\nu$, gas absorption can vary dramatically. To account for this variation and thus the variation in the gas absorption coefficient k, a model can be run once for each wavelength and its associated k in the band. This method is referred to as the line-by-line (LBL) technique. Though extremely accurate, this method suffers from the time and computing resources required to employ it. A solution to this problem involves creating a smooth function that describes the variation of k in the spectral band. This is the k-distribution technique and is described in Lacis and Oinas (1991). Observing that the mean transmission of the band ($T_{\bar{\nu}}$) is independent of the order of k, a probability density function (pdf) for the k values in the band $f(k)$ can be created. Integration over the pdf for all k also results in the mean transmission:

$$T_{\bar{\nu}} = \int_{\Delta\nu} e^{-k(\nu)u} \frac{d\nu}{\Delta\nu} = \int_0^\infty f(k) e^{-ku} dk \tag{5.1}$$

Although integration is performed in k space, the function $f(k)$ is usually not smooth. (5.1) still requires a lot of integration nodes and therefore more computation time. However, $f(k)$ can be described by a cumulative probability function $g(k)$

$$g(k) = \int_0^k f(k) dk \tag{5.2}$$

which is monotonically increasing and smooth in k space. Also, instead of integrating over k, the inverse of $g(k)$ can be used. $k(g)$ also monotonically increases and its bounds of integration are 0 to 1:

$$T_{\bar{\nu}} = \int_{\Delta\nu} e^{-k(\nu)u} \frac{d\nu}{\Delta\nu} = \int_0^1 e^{-k(g)u} dg \tag{5.3}$$

A striking example of the utility of this method is seen in Fig. 5.1. Here, the absorption coefficient $k(\nu)$ is shown for the 9.6 μm band (in the infrared portion of the spectrum) of ozone. To integrate $e^{-k(\nu)u}$ in (5.1) requires large amounts of computer time to account

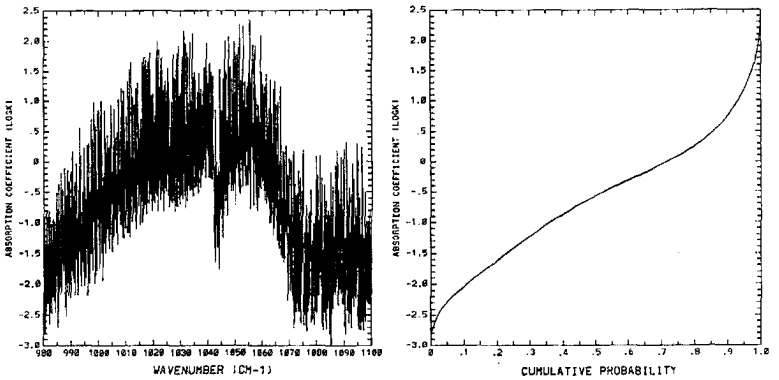

Figure 5.1: Absorption coefficient $k(\nu)$ in (cm atm)$^{-1}$ as a function of (a) wavenumber and (b) cumulative probability $k(g)$ for the O_3 9.6-μm band for a pressure of 25 mb and a temperature of 220 K. (from Fu and Liou, 1992)

for the large variations in $k(\nu)$. However, the same result can be obtained by integrating $e^{-k(g)u}$ in (5.3). Because $e^{-k(g)u}$ is a smooth function as seen in the second plot of Fig. 5.1, fewer integration nodes are necessary and less computation time is needed.

Discretization of $k(g)$ into intervals over which $k(g)$ can be considered constant results in the following:

$$T_{\bar{\nu}} \approx \sum_{i=1}^{n} w_i e^{-k_i u} \tag{5.4}$$

Here, there are n intervals of absorptions and associated with each is a weight w which specifies the fraction of $k(g)$ with that particular extinction.

5.2.2 K-Distribution Implementation

The implementation of the k-distribution method involves creating a dataset that provides the absorption coefficient k and weight for each band interval for each gas. The absorption coefficients are actually functions of pressure and temperature and for the k-distribution tables are specified at reference values. To account for pressure and temperature variations, the optical path u of the photon is scaled. For the present application, the gas density ρ_g which is used to calculate u will be scaled. By doing this, the absorption coefficient k, the gas density ρ_g, and the photon path length l can be kept separate. This will become important when the Equivalence Theorem is implemented. The present model uses gas profiles which are divided into layer quantities. Hence, each layer is assigned a

mean temperature $\bar{T}$ and mean pressure $\bar{P}$. The scaled ρ_g for a particular layer used by Chou and Arking (1981) for infrared calculations is:

$$\rho'_g = \left(\frac{\bar{P}}{P_{ref}}\right)^n \left(\frac{T_{ref}}{\bar{T}}\right)^m \rho_g \tag{5.5}$$

where P_{ref} and T_{ref} are the reference pressure and temperature at which the k-distribution tables are defined. m and n are are empirical and are chosen depending on how the tables were computed. Chou and Arking (1981) note that temperature scaling is not as important in the solar region of the spectrum if T_{ref} is chosen in the middle of the possible temperature range. In this study in which only solar wavelength are considered, m is zero. By keeping ρ'_g and l separate, (5.4) becomes:

$$T_{\bar{\nu}} \approx \sum_{i=1}^{n} w_i e^{-k_i u} = \sum_{i=1}^{n} w_i e^{-k_i \rho'_g l} \tag{5.6}$$

The units for k, ρ'_g, and l are $cm^2 \cdot g^{-1}$, $g \cdot cm^{-3}$, and cm, respectively. Hence, the exponential term in (5.6) remains dimensionless.

When used to compute a band flux for a single layer, the k-distribution method described above returns a gas absorption coefficient k and a weight w for each parameterized interval in the band. The model is then run once for each k to obtain a corresponding flux $F(k)$. The total flux for the band is:

$$F_{\Delta\nu} = \sum_{i=1}^{n} w_i F(k_i) \tag{5.7}$$

for n intervals in the band. For bands in which two gases are absorbing, the following approximation is made:

$$F_{\Delta\nu} = \left(\sum_{i=1}^{n_1} w_{1i} F(k_{1i})\right)\left(\sum_{j=1}^{n_2} w_{2j} F(k_{2j})\right) \approx \sum_{i=1}^{n_1}\sum_{j=1}^{n_2} w_{1i} w_{2j} F(k_{1i}) F(k_{2j}) \tag{5.8}$$

A description of the k-distribution data used in the present model can be found in Chou and Arking (1981) for H_2O and Chou (1990) for CO_2 and O_2. Ozone (O_3) absorption is handled in a different manner than k-distribution. The UV cross-section method as seen in Stamnes and Tsay (1990) is a simple application of Beer's Law for a wavelength band of average ozone absorption coefficient $k(\nu)$. Because ozone absorption is a smooth function

in the solar spectrum between 1.75 and 7.0 μm, there is no need to create k-distributions to increase model speed. Instead, the average $k(\nu)$ (weighted by the incoming solar flux) is used for each band (Chandrasekhar, 1960):

$$\bar{k}(\nu) = \frac{\int_{\nu_1}^{\nu_2} k(\nu) F_o(\nu) d\nu}{\int_{\nu_1}^{\nu_2} F_o(\nu) d\nu} \tag{5.9}$$

Therefore, the flux in the ozone absorption band $F_{\Delta\nu}$ is calculated using only one interval and a weight equal to 1.

In total, there are four absorbing gases used in this study in the shortwave solar spectrum between .2 and 4 μm. The exact bandwidths of each absorber are shown in Table 5.1 and the scaling exponents m and n used in (5.5) and the reference pressures and temperatures for each gas are shown in Table 5.2.

Table 5.1: Gas absorption regions in the solar spectrum

gas	bandwidth (μm)	bands
H_2O	.687–3.846	237
CO_2	1.429–1.667, 1.887–2.174, 2.500–3.030	48
O_2	.687–.699, .760–.778	11
O_3	.280–.687	11

Table 5.2: Reference parameters and scaling exponents

gas	P_{ref} (mb)	n	T_{ref} (K)	m
H_2O	300.00	0.8	240.00	0.0
CO_2	300.00	0.8	240.00	0.0
O_2	300.00	0.8	240.00	0.0
O_3	300.00	0.4	273.15	0.2

Running the model for each k_i to calculate $F(k_i)$ needed for (5.8) is a time consuming process as noted above. It is possible, however, to calculate $F(k_i)$ after the Monte Carlo model has been run regardless of the complexity of the gas or cloud. This involves a statistical approach to photon transmission by obtaining a photon path length distribution from the Monte Carlo model.

5.3 The Equivalence Theorem

Although the k-distribution technique decreases the number of flux calculations required to cover the shortwave solar spectrum from potentially hundreds of thousands to 12452, this number is still too large to be performed by the Monte Carlo model alone. The key to streamlining performance lies in the realization that the paths of photons in the Monte Carlo model are identical for all gas optical depths as long as the scattering parameters of the atmosphere can be considered constant. The same holds for all cloud and surface absorptions. If the statistics of photon paths are kept from the Monte Carlo run, the fluxes including absorptions can be calculated off- line. This is accomplished using the modified Equivalence Theorem. The following subsections describe the modified Equivalence Theorem method for gas absorption and analogous methods for computing cloud and surface absorption.

5.3.1 Application to Gas Absorption

The Equivalence Theorem is explained in Irvine (1964) and later in Van de Hulst (1980). The root of its derivation is Beer's law of transmission: $T(\lambda_c) = e^{-\tau\lambda_c}$ where $T(\lambda_c)$ is the transmission of a of a photon or a packet of photons along an optical path length λ_c through a homogeneous layer of scattering and absorbing cloud embedded in a homogeneous absorbing gas. The layer total optical depth is τ. The associated intensity or flux (F) of the photon is then the flux of the photon before entering the layer (F_o) modified by the transmission:

$$F = F_o e^{-\tau\lambda_c} \tag{5.10}$$

As described above, to maximize the efficiency of the flux calculation in terms of Monte Carlo modeling, the attenuation due to gas needs to be separated from that due the to cloud optical properties. If the Monte Carlo model returns F_o and λ_c after cloud scattering and attenuation are taken into account, gas attenuation is accounted for in the following relation:

$$F = F_o e^{-\frac{\tau_g}{\tau_c}\lambda_c} \tag{5.11}$$

Of course, the Monte Carlo technique uses thousands of photons to estimate flux. This results in many different photon path lengths. To explicitly record all path lengths would be just as computationally expensive as performing the calculation during the model run. Instead, gas absorption is handled statistically. The Monte Carlo model can simply return the photon path length probability density function $p(\lambda_c)$ which is a normalized frequency distribution of occurrence of each path length. The composite flux from all photons is (5.11) integrated over all possible lengths:

$$F = F_o \int_0^\infty p(\lambda_c) e^{-\frac{\tau_g}{\tau_c}\lambda_c} d\lambda_c \tag{5.12}$$

This is the Equivalence Theorem as explained by Irvine (1964). This relation applies to a homogeneous layer of cloud embedded in a homogeneous gas. However, modifications to (5.12) must be made for application to a heterogeneous cloud embedded in a gas which has a vertically varying atmospheric profile. The restriction of the original derivation (5.12) to a homogeneous cloud layer arises from the use of optical path length. The cloud optical path in clear air between cloud parcels is zero. As a result, (5.12) will not attenuate the radiation in this region even though it travels through an absorbing gas. The remedy for this is to separate cloud and gas extinction and keep a path length distribution that is not dependent on the properties of the cloud. This is related directly from Irvine's Equivalence Theorem by using the definitions of optical depth (τ_g and τ_c) and optical path (λ_c):

$$e^{-\frac{\tau_g}{\tau_c}\lambda_c} = e^{-\frac{\Delta z \cdot k}{\Delta z \cdot \sigma_e} l \sigma_e} = e^{-kl} \tag{5.13}$$

Now, instead of $p(\lambda_c)$, the geometric path length distribution $p(l)$ is used in (5.12) and the new relation becomes:

$$F = F_o \int_0^\infty p(l) e^{-kl} dl \tag{5.14}$$

In the case of a homogeneous layer of cloud and gas, this relation is identical to (5.12) because $p(\lambda)$ is identical to $p(l)$. However, for a layer consisting of a heterogeneous cloud embedded in a homogeneous gas, $p(\lambda)$ and $p(l)$ can be very different. Thus, $p(l)$ must be output from the Monte Carlo model and the gas absorption coefficient k is be used instead of the gas optical depth.

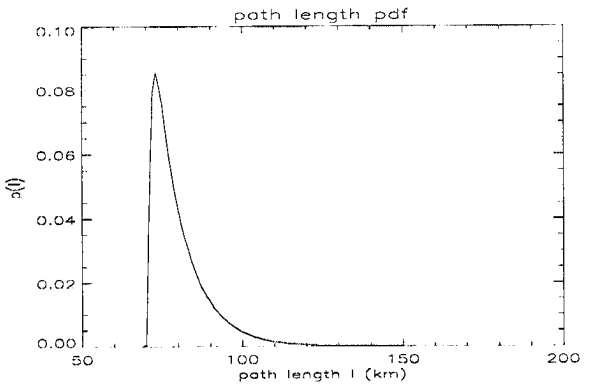

Figure 5.2: A path length pdf for downwelling flux at the surface. This example is from the model run with a cloud in the lowest layer, a solar zenith angle of 45 degrees, and no Rayleigh scattering.

An example of $p(l)$ output from the Monte Carlo model is shown in Fig. 5.2. This was taken from the model validation that will be presented at the end of this chapter. The model atmosphere consisted of a cloud between 1 and 2 km. Rayleigh scattering was not implemented. The pdf displayed is comprised of path length probabilities for photons which have crossed the surface downwelling flux measurement level. These photons will not have path lengths that are shorter than that required to travel in a straight path from the top of the atmosphere to the surface at the specified solar zenith angle (45 degrees for this case). For cases that will be used in this study, it has been determined that a path length pdf covering 1000 km with a one km bin size is sufficient for gaseous absorption calculations.

Now that cloud heterogeneity has been accommodated, the Equivalence Theorem must be modified again to account for a profile of gas in the model atmosphere which varies in the vertical. This is accomplished by keeping a pdf for each path length bin that describes how much of the path occurred in each gas layer. This allows the average k to be calculated which can then be used in (5.14). As a simple example, consider a photon which travels through a two layer atmosphere as portrayed in Fig. 5.3. Layer 1 has a gas extinction coefficient k_1 and layer 2 k_2. The total geometric path length is $l = l_1 + l_2 + l_3$. The average gas extinction encountered by the photon is:

$$\bar{k} = \frac{(l_1 + l_3)k_1 + l_2 k_2}{l} \tag{5.15}$$

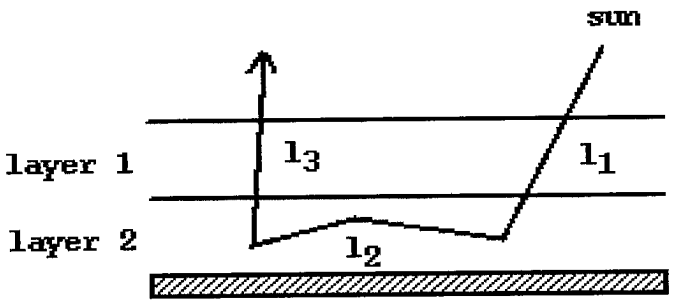

Figure 5.3: Path of one photon through 2 gas layers (scattering cloud not shown in layer 2). l_1, l_2, and l_3 are used to calculate the mean gas extinction coefficient.

Another way to write this is in terms of a pdf. The pdf needed to calculate the average extinction encountered by the photon with total path length l is denoted $p(l, n)$ where n indicates the layer number. This pdf describes how much of l occurs in each layer. The function $p(l, n)$ is normalized for each l and, therefore, is not quite a true two-dimensional pdf. The average extinction is then written:

$$\bar{k} = p(l, 1)k_1 + p(l, 2)k_2 \tag{5.16}$$

or

$$\bar{k} = \sum_{n=1}^{2} p(l, n)k_n \tag{5.17}$$

An example of the pdf $p(l, n)$ is shown in Fig. 5.4. The Monte Carlo model atmosphere used to produce it was the same as that for Fig. 5.2. Here, it is seen that photon path length increase is due primarily to increased residence time of the photon in the lowest layer. This is the layer containing the scattering cloud. This surface actually represents one pdf for each path length value.

Using the above formulation of the average extinction coefficient, the flux including gas absorption (5.14) for N layers is:

$$F = F_o \int_0^\infty p(l) e^{-l \sum_{n=1}^{N} p(l,n) k_n} dl \tag{5.18}$$

5.3.2 Application to Cloud and Surface Absorption

As noted previously, the cloud properties (σ_{ext}, g, and ω_o) and surface albedo (α) used in computing F_o are constant for each interval in the spectrum. However, it is useful

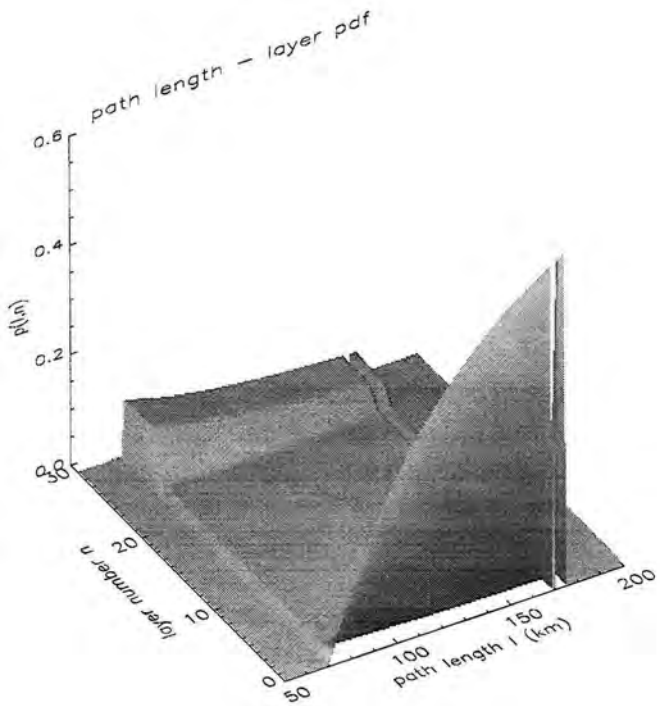

Figure 5.4: The pdf $p(l, n)$ is actually a collection of one pdf for each path length value. This example is for downwelling flux at the surface from the model run with a cloud in the lowest layer, a solar zenith angle of 45 degrees, and no Rayleigh scattering.

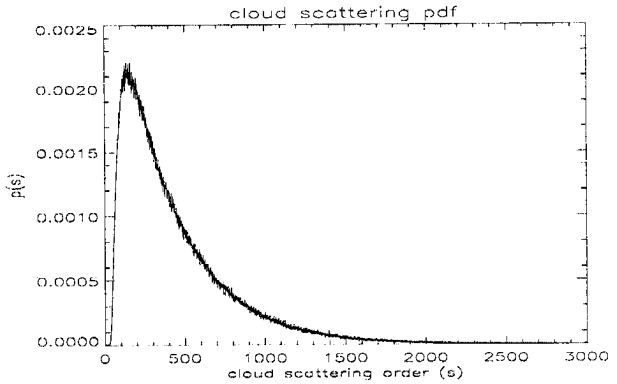

Figure 5.5: A cloud scattering pdf for downwelling flux at the surface. This example is from the model run with a cloud in the lowest layer, a solar zenith angle of 45 degrees, and no Rayleigh scattering.

to recognize the fact that cloud and surface absorption can be treated in the same manner as gas absorption. Neither ω_o nor α have any bearing on the geometry of a photon's trajectory. Instead, the photon is simply attenuated by these parameters at each collision with a cloud particle or the surface. Therefore, cloud absorption and surface albedo can be accounted for after the Monte Carlo run as long as information is saved about how often photons scatter off each medium. Like gas absorption, this information is contained in probability density functions.

To obtain the pdf for cloud scattering events, the model cloud is defined as conservatively scattering ($\omega_o = 1.0$) and the total number of times each photon scatters is put into a scattering pdf $p(s)$. Here, s denotes the scattering order or total number of scatters for a photon. Because this pdf is discrete (there can only be integer numbers of scatters), it is summed over scattering orders and multiplied to the flux that is returned from the Monte Carlo model without cloud absorption:

$$F = F_o \sum_{s=0}^{\infty} \omega_o^s p(s) \tag{5.19}$$

Fig. 5.5 shows a typical cloud scattering pdf. It has been determined that 5000 scattering orders are enough to allow (5.19) to be accurate for thick cloud.

Similarly, the pdf for surface scatters $p(r)$ is constructed during the Monte Carlo run in which the surface is perfectly reflecting ($\alpha = 1.0$). Here, r is the number of times

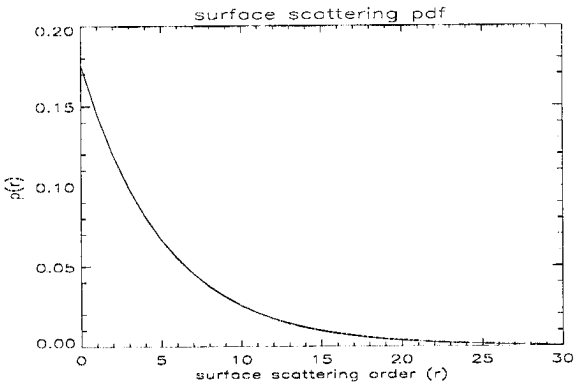

Figure 5.6: A surface scattering pdf for downwelling flux at the surface. This example is from the model run with a cloud in the lowest layer, a solar zenith angle of 45 degrees, and no Rayleigh scattering.

a photon strikes the surface. The contribution to the flux by all photons including the absorption by the surface is:

$$F = F_o \sum_{r=0}^{\infty} \alpha^r p(r) \tag{5.20}$$

An example of a surface scattering pdf is shown in Fig. 5.6. This is shown for the same case as the previous pdf examples. Only 50 orders of surface scattering are retained. Because the surface albedo used in this study is never greater than .5, scattering orders beyond 50 will result in a negligible flux contribution as seen in (5.20).

There are two primary advantages to treating cloud and surface absorption in a manner analogous to the Equivalence Theorem for gas absorption. First, there is less constraint on the size of the intervals of constant cloud optical properties or surface properties that are used in the Monte Carlo model. The intervals are now only dependent on σ_{ext} and g which may result in larger-in-size and thus fewer intervals required to cover the entire spectrum. This saves Monte Carlo computational time. Second, because cloud and surface absorptions are no longer parameterized by intervals of assumed constant values, any spectral resolution for ω_o and α can be used. This is especially important for this study in which absorption of solar radiation is explored at high spectral resolution.

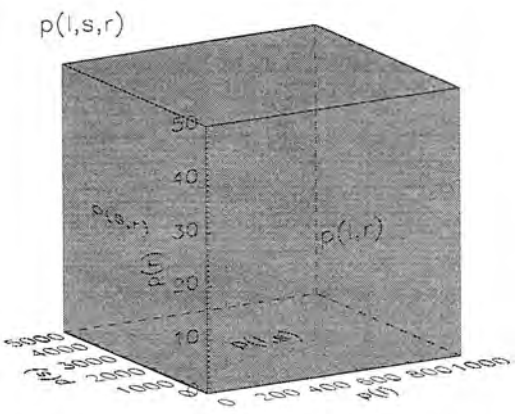

Figure 5.7: A portrayal of the three-dimensional pdf $p(l, s, r)$. Integration of this pdf over one absorber results in a two-dimensional pdf (one of three faces) that can be used to compute the flux associated with the remaining two absorbers. Integration over two absorbers results in a one dimensional pdf (one of three axes) which is used in a similar fashion.

5.3.3 Equivalence Theorem Implementation

(5.18), (5.19), and (5.20) represent the radiative flux when only gas, cloud, or surface absorption are accounted for outside of the Monte Carlo model. Obviously, a great deal of flexibility can be achieved if all of these absorbers can be dealt with at the same time after the Monte Carlo run. The total flux when all absorbers are accounted for in an Equivalence Theorem manner is obtained by using a three-dimensional pdf. This pdf $p(l, s, r)$ contains information about how often every possible combination of path length, cloud scattering, and surface scattering occurs. The expression that calculates the total flux is the integral (continuous and discrete) over the three-dimensional pdf and appears as a combination of (5.18), (5.19), and (5.20):

$$F_{tot} = F_o \cdot \int_0^\infty \left(\sum_{s=0}^{\infty} \left(\sum_{r=0}^{\infty} p(l, s, r) \alpha^r \omega_o^s e^{-l \sum_{n=1}^{N} p(l,n) k_n} \right) \right) dl \tag{5.21}$$

The pdf $p(l, s, r)$ holds a great deal of information and can be used to calculate the total flux as well as the flux including any combination of the three absorbers. Integration of the pdf over l, s, or r results in a two-dimensional pdf which is used to calculate the flux accounting for the remaining two absorbers. Further integration of the two-dimensional pdf returns a one-dimensional pdf from which the flux including only one absorber is

obtained. As an example, the volume pdf $p(l, s, r)$ is shown in Fig. 5.7. Integration over s results in the face of the cube denoted $p(l, r)$. This pdf is used to obtain the flux including only gas and surface absorption. Further integration over r results in the cube axis $p(l)$. This one-dimensional pdf would be used to calculate the flux including only gas absorption. In all, there are eight combinations of fluxes that can be calculated after one run of the Monte Carlo model. Of course, integration over a pdf that is smaller in dimension than $p(l, s, r)$ requires eliminating a summation or integration in (5.21). A list of the pdf needed and the corresponding modification to (5.21) for each combination is given in appendix A.

Use of (5.21) or any of the relations listed in appendix A requires that the Monte Carlo model be run with no absorption ($\omega_o = 1$, $\alpha = 1$, and no gas). This condition eliminates variance reduction techniques discussed in the previous chapter. Because every photon is traced until it leaves the top of the atmosphere, the speed of the Monte Carlo run will be decreased. However, this speed decrease is more than acceptable given the efficiency gained by using the above Equivalence Theorem techniques.

As powerful as the full three-dimensional pdf is, it is not without its limitations. If all desired path lengths (0 to 1000 km), cloud scattering orders (0 to 5000), and surface scattering orders (0 to 50) are kept, $p(l, s, r)$ is too large to be held in the memory of any computer available to this study. If this pdf is stored as an integer array (to be normalized later) it would require 500 megabytes of random access memory. Furthermore, the Monte Carlo model used in this study keeps track of probability density functions for upwelling and downwelling flux above and below cloud level. Unless each pdf is obtained by running the Monte Carlo model four times for the same atmospheric parameters (a factor of four decrease in speed), 2 gigabytes of memory are required. This is beyond the capacity of most computers. Thus, the full pdf $p(l, s, r)$ cannot be used.

A practical assumption is required to decrease the information needed by the above Equivalence relations in order to continue with this study. The pdf $p(l, s, r)$ must be reconstructed from as little information as possible while retaining as much accuracy as possible. According to probability theory, if the functions $p(l)$, $p(s)$, and $p(r)$ are

independent, then the following is true:

$$p(l, s, r) = p(l) \cdot p(s) \cdot p(r) \tag{5.22}$$

Thus, the three dimensional probability density function can be reconstructed from three vectors which require relatively little computer memory. However, each of the three probability vectors defined for this study are not completely independent. As a result, the above relation becomes an approximation. The more dependent the probabilities become, the worse the approximation is. Because any combination of the above vectors into a two-dimensional array can be accommodated by a computer with a modest amount of memory, the task becomes one of placing the two most dependent probabilities in a pdf that will result in a reasonable approximation. Clearly, when the cloud becomes very thick, occurrences of surface scatters will be correlated with a high number of cloud scatters. After all, the photon must travel the vertical extent of the cloud to reach the surface. The thicker the cloud is, the more cloud scattering occurs. Total path length is not as correlated with the number of cloud or surface scatters, especially for low clouds. Because most of the cases used for this study involve low, thick clouds, cloud and surface scatters are accounted for in the two-dimensional pdf:

$$p(l, s, r) \approx p(l) \cdot p(s, r) \tag{5.23}$$

A more rigorous derivation of this approximation begins with the chain rule. Here, it is already known that cloud and surface scatters will be grouped together.

$$\begin{aligned} p(l, s, r) &= p(l|s, r) \cdot p(s|r) \cdot p(r) \\ &= p(l|s, r) \cdot p(s, r) \\ &\approx p(l) \cdot p(s, r) \end{aligned}$$

The conditional probability $p(l|s, r)$ simply contains the probability that a photon has a total path length l given that is has scattered s times off a cloud and r times off the surface. If the path length probability were completely independent of s and r, then $p(l) = p(l|s, r)$.

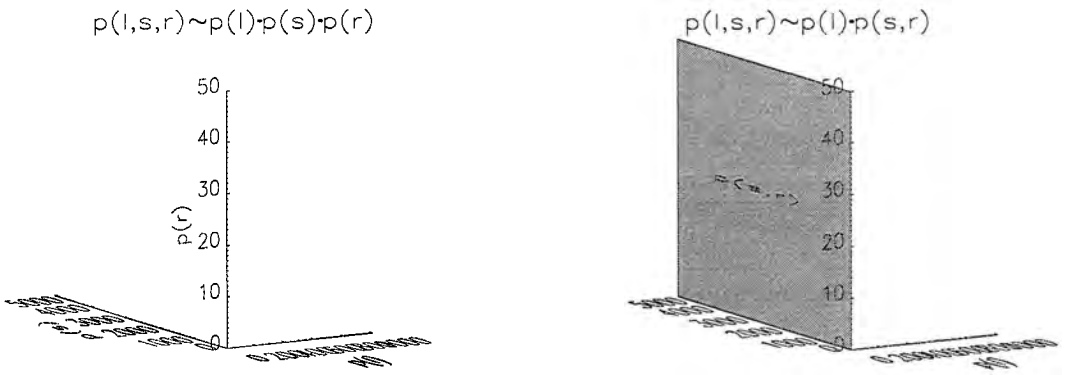

Figure 5.8: The amount of information that is used to approximate the full three dimensional pdf $p(l, s, r)$ as used by (5.22) and (5.23). The arrays denoted $p(l) \cdot p(s, r)$ holds more information and are a better approximation. The decrease in size from $p(l, s, r)$ allows this information to be stored in computer memory.

Fig. 5.8 portrays the amount of information that (5.22) (which is actually approximate as a result of dependence) and (5.23) use to reconstruct the pdf $p(l, s, r)$ as portrayed in Fig. 5.7.

Beyond constructing this relation for the total flux, the exact form of the k-distribution used in the present code must be established. This involves a modification of (5.18) to accommodate absorber amount as discussed above with k-distribution density scaling. The Equivalence theorem routine takes as input from the Monte Carlo model the flux without gas, cloud, or surface absorption (F_o) and the photon path length distribution ($p(l)$). Gas amounts are input from an atmospheric profile. The modified Equivalence Theorem for gas (5.18) including k-distribution scaling and absorber amount becomes:

$$F = F_o \int_0^\infty p(l) e^{-l \sum_{n=1}^{N} p(l,n) \rho'_{g,n} k_n} dl \tag{5.24}$$

The addition of this routine to the Monte Carlo routine described in the previous chapter is the essence behind the Monte Carlo/Equivalence Theorem model (hereafter referred to as MC/ET). The combined package now has the ability to measure spectral and broadband solar fluxes that are reflected from or transmitted through a heterogeneous cloud embedded in a gas atmosphere. The variation in the vertical profile of the gas atmosphere and a spectrally varying reflecting surface are also accounted for. Of course, the Monte Carlo portion of the model as described to this point is only run once because

it is assumed that the scattering properties of the atmosphere are constant. This is not a poor assumption in the solar shortwave part of the spectrum, however to obtain a better degree of accuracy the spectral region must be subdivided into smaller regions. This optimization will be discussed in the next chapter.

5.4 Model Performance

The following 5 figures show results from a test of the MC/ET model assuming the scattering properties of the atmosphere are constant across the solar spectrum. The model atmosphere consisted of a 30 layer gas atmosphere and a cloud in the 0 to 1 km layer. The Monte Carlo portion of the model was run once with a cloud optical depth $\tau = 40$ asymmetry factor $g = .85$, and a solar zenith angle of 45 degrees. Gas, cloud, and surface absorption across the shortwave spectrum (.2 to 4.μm) were taken into account by the modified Equivalence Theorem portion of the model. The gas atmosphere included the standard McClatchey mid-latitude summer profiles of the four k-distribution constituents (H_2O, CO_2, O_3, and O_2). The cloud single scattering albedo was taken from a stratocumulus type I cloud (ScI) as given in Stephens (1979). The surface albedo was derived from the ARESE campaign and varied from .15% in the visible to .35% in the near infrared (this is discussed in more detail in Chapter 8). Upwelling flux at the top of the atmosphere and downwelling flux at the surface are plotted for five cases: flux without any absorption (Fig. 5.9), only surface absorption (Fig. 5.10), only cloud absorption (Fig. 5.11), only gas absorption (Fig. 5.12), and including all absorptions (Fig. 5.13). These fluxes are compared to results from a 32-stream adding-doubling model. Also shown in each figure are the integrated broadband flux results and relative error. The lower half of each figure shows the spectral absolute and relative errors. Because spectral fluxes can go to zero in gas absorption bands, the relative errors are calculated with respect to the TOA downwelling solar spectral flux.

When no absorption is accounted for, the results shown in Fig. 5.9 simply reiterate the comparisons of the Monte Carlo and 32-stream adding-doubling models in Chapter 4. Because the spectral flux in this case is the single flux value obtained from each model run

multiplied by the incoming spectral solar flux, the difference between the two is a constant relative error. The relative error is below 1% for the spectral and broadband upwelling and downwelling fluxes. Likewise, Figures 5.10 and 5.11 show that fluxes calculated including surface and cloud absorption agree to within 1%. The flux including only gas absorption in Fig. 5.12 also results in less than 1% broadband error. However, the spectral errors for upwelling flux are larger. The largest errors occur in the absorbing regions of the spectrum. The absolute errors are larger, reaching 20 $Wm^{-2}\mu m^{-1}$. This may result from numerical error involved when the proability density functions $p(l)$ and $p(l,n)$ are integrated many times or simply the difference in how gas absorption is handled. Decreasing the path length pdf bin size from 1 km to .5 km did not decrease this error.

When all absorptions are included according to (5.23), the errors associated with the approximation are evident in Fig. 5.13. The upwelling broadband flux error is now 1.6% and the downwelling error is 3.6%. Upwelling absolute spectral error, which had not been greater than 20 $Wm^{-2}\mu m^{-1}$ for the individual absorbers, has doubled. Because gas is not included in the same pdf as cloud and surface absorption, the largest errors are expected where all three are important. This occurs in the water vapor absorption bands. If the full three-dimensional pdf had been used, it is expected that the spectral errors in Fig. 5.13 would have been smaller.

This error analysis was conducted to prove the MC/ET theory is valid. To prove absolute accuracy, the present model should be compared against a benchmark plane-parallel, high spectral resolution calculation. At the time of this experiment, this was unavailable. The 32-stream was the most accurate model available that would run in a reasonable amount of time. Running the adding-doubling model with 64-streams theoretically would have increased accuracy, however the model would have required many days to run. As a comparison, the MC/ET model required one hour whereas the 32-stream required about twenty. The 32-stream model is slow because it must perform all 12452 multiple scattering calculations.

5.5 Summary

In this chapter, the theory and implementation of the k-distribution method for gas absorption was discussed. These data allow computation of spectral fluxes at high resolution in the shortwave solar spectrum. Though requiring fewer calculations than line-by-line techniques, the high spectral resolution computations are still prohibitively time consuming for Monte Carlo applications. The Equivalence Theorem, as described by Irvine (1964) and Van de Hulst (1980), was modified and extended to accommodate a heterogeneous cloud embedded in a gas with a vertically varying profile in order to address this problem. Similar relations were introduced to account for high resolution variations in cloud and surface absorption. When used with the Monte Carlo model derived in the previous chapter, the resulting MC/ET model is able to calculate spectral fluxes over the entire solar spectrum assuming constant scattering parameters in a simple and efficient manner. The validity of the modified Equivalence Theorem theory was shown relative to a 32-stream adding-doubling model. The spectral errors are within the requirements of a study such as this. Also, the broadband errors are smaller than those quoted by previous researchers as justification for using a Monte Carlo model. The following chapter will discuss the subdivision of the shortwave solar spectrum into intervals to more accurately describe the variations in scattering geometry due to cloud and Rayleigh characteristics.

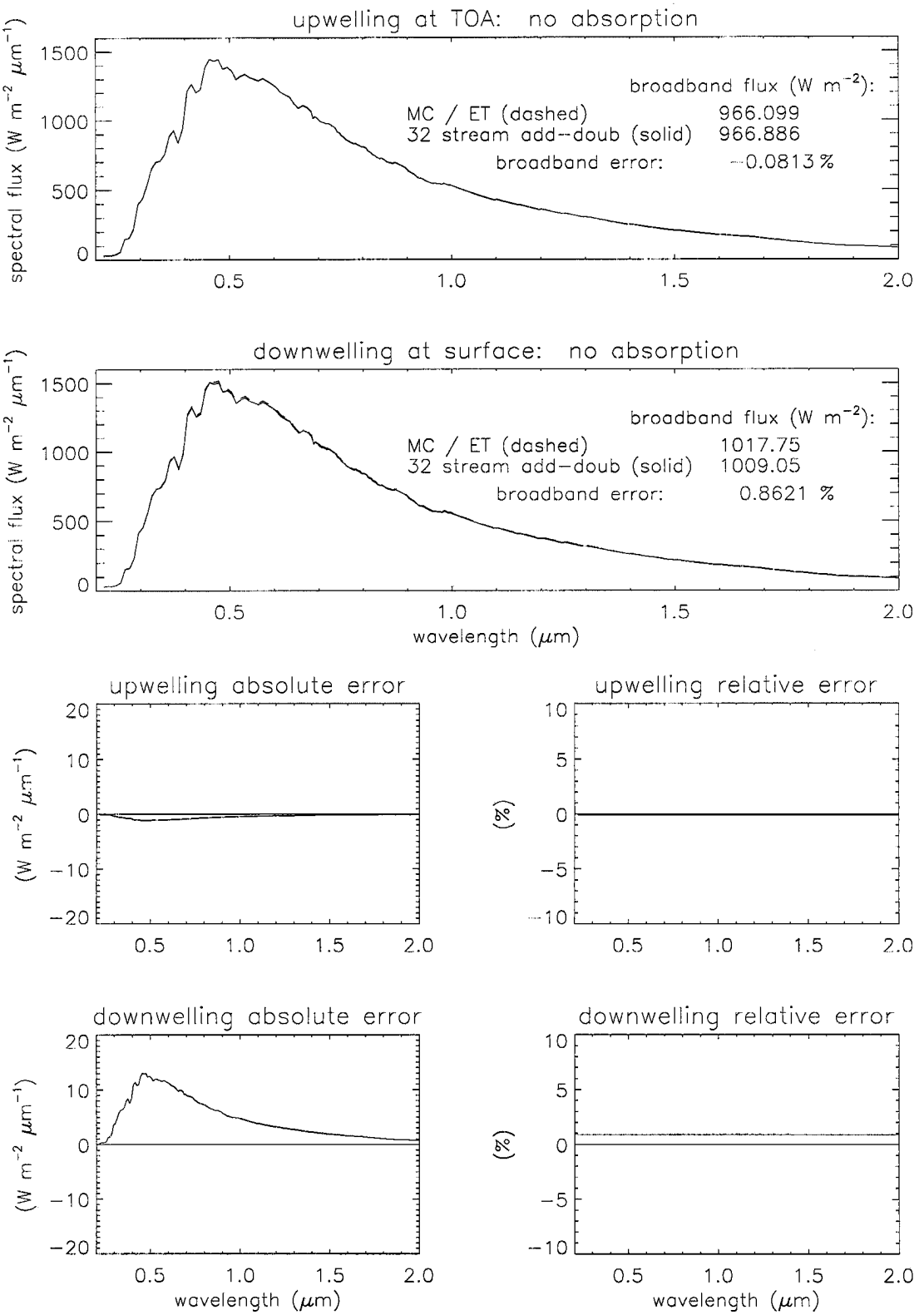

Figure 5.9: Comparison of results from MC/ET and the 32-stream adding doubling model without any atmospheric absorption.

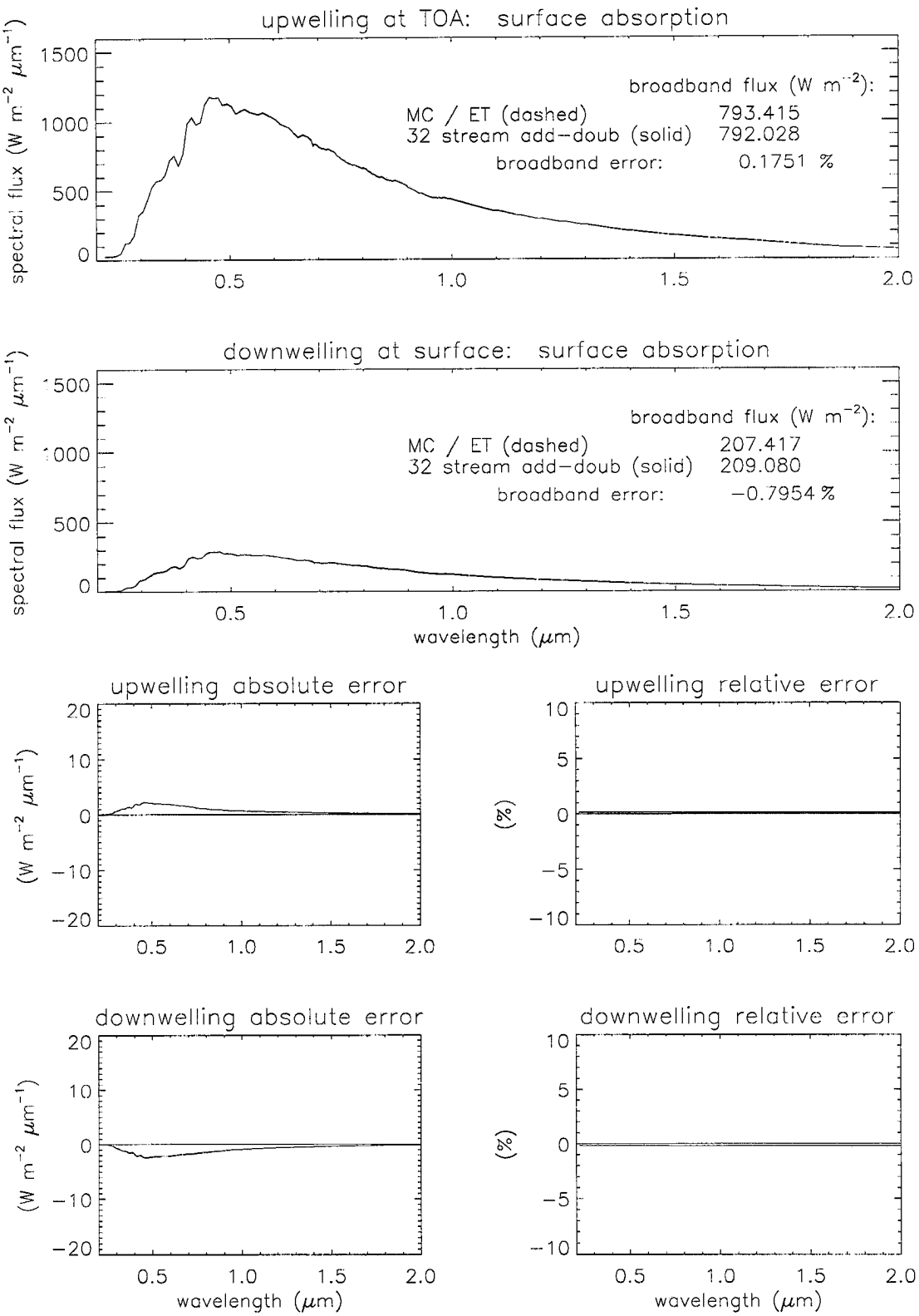

Figure 5.10: Comparison of results from MC/ET and the 32-stream adding doubling model when absorption by the surface is taken into account.

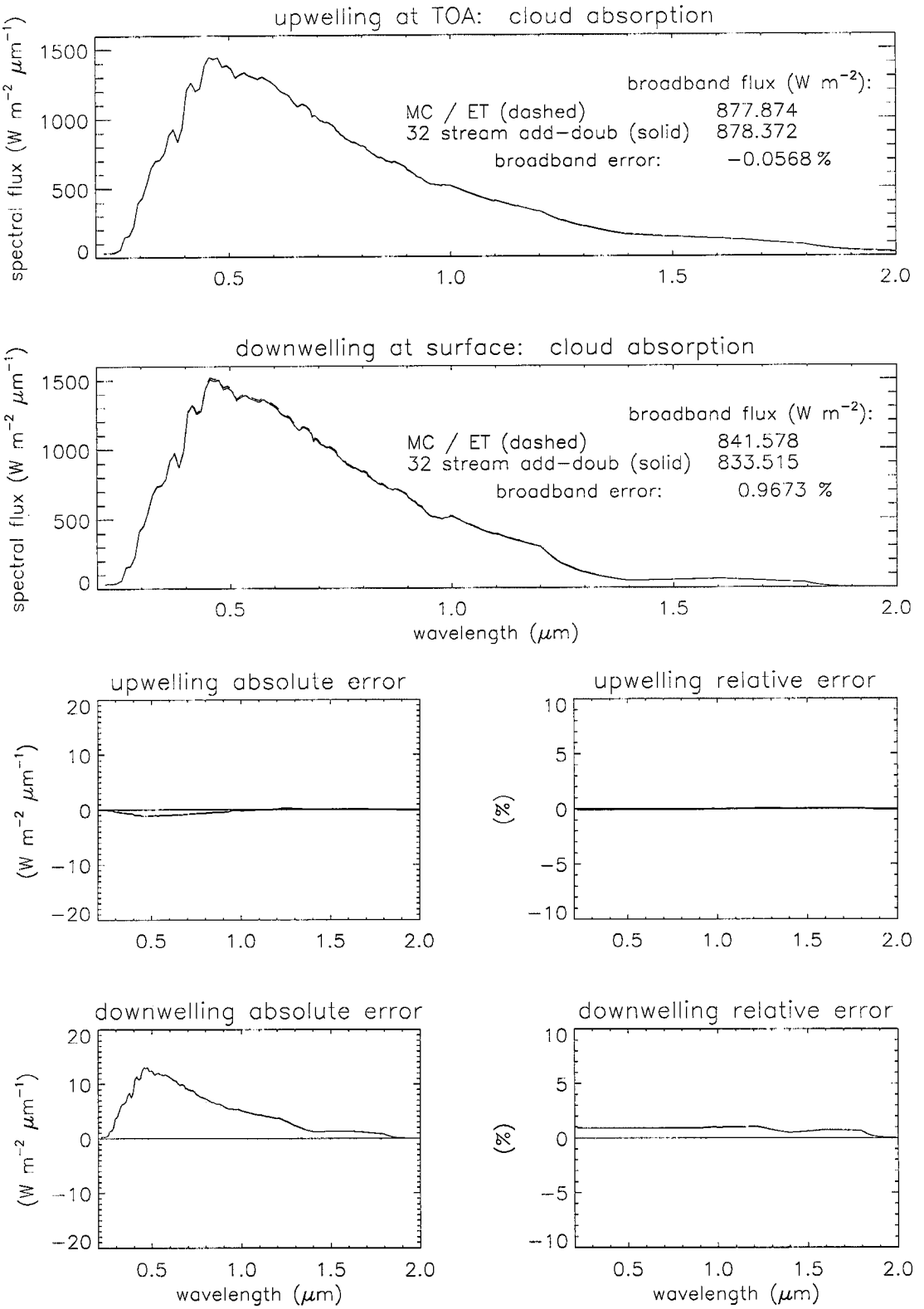

Figure 5.11: Comparison of results from MC/ET and the 32-stream adding doubling model when absorption by cloud is taken into account.

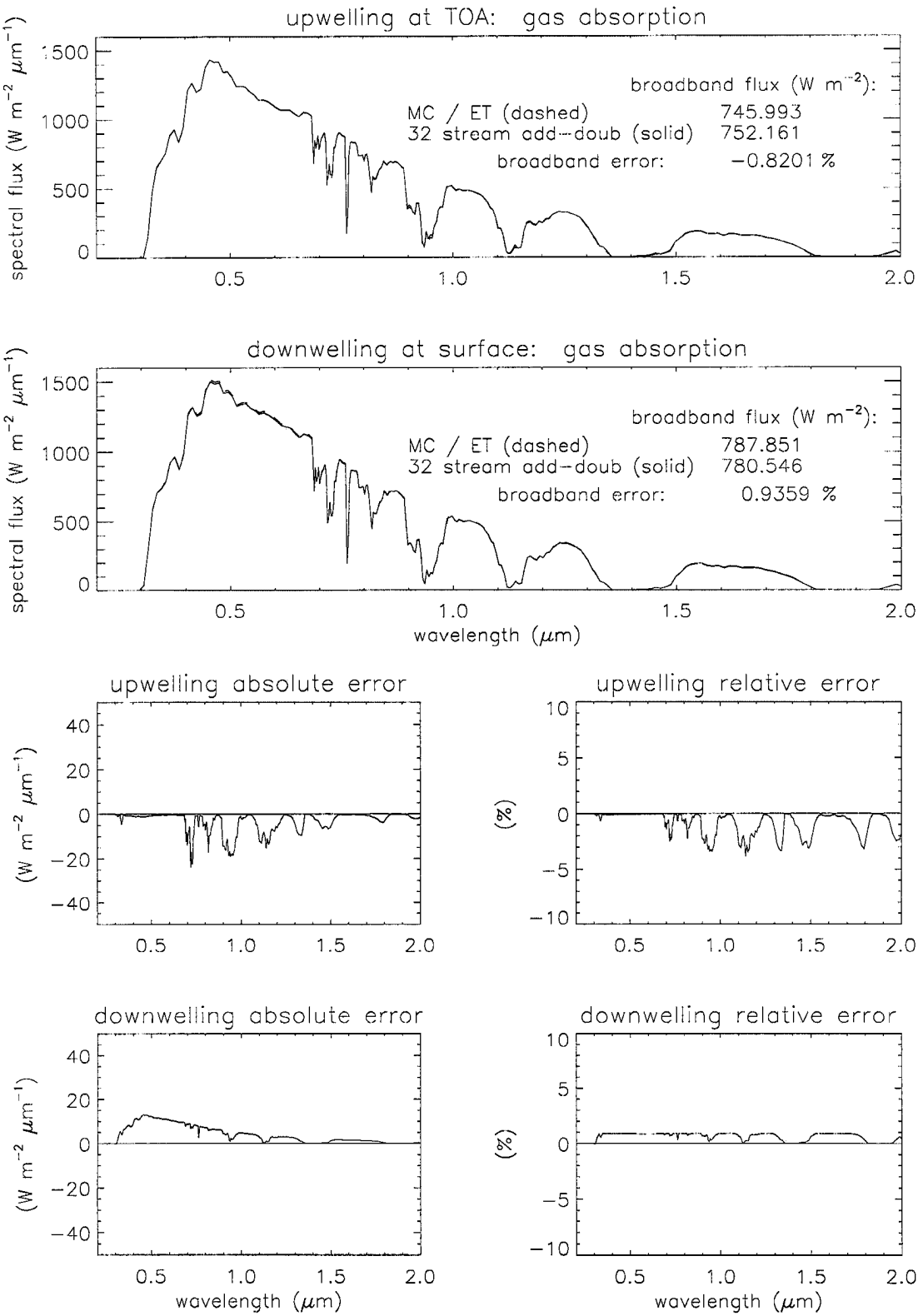

Figure 5.12: Comparison of results from MC/ET and the 32-stream adding doubling model when absorption by gas is taken into account.

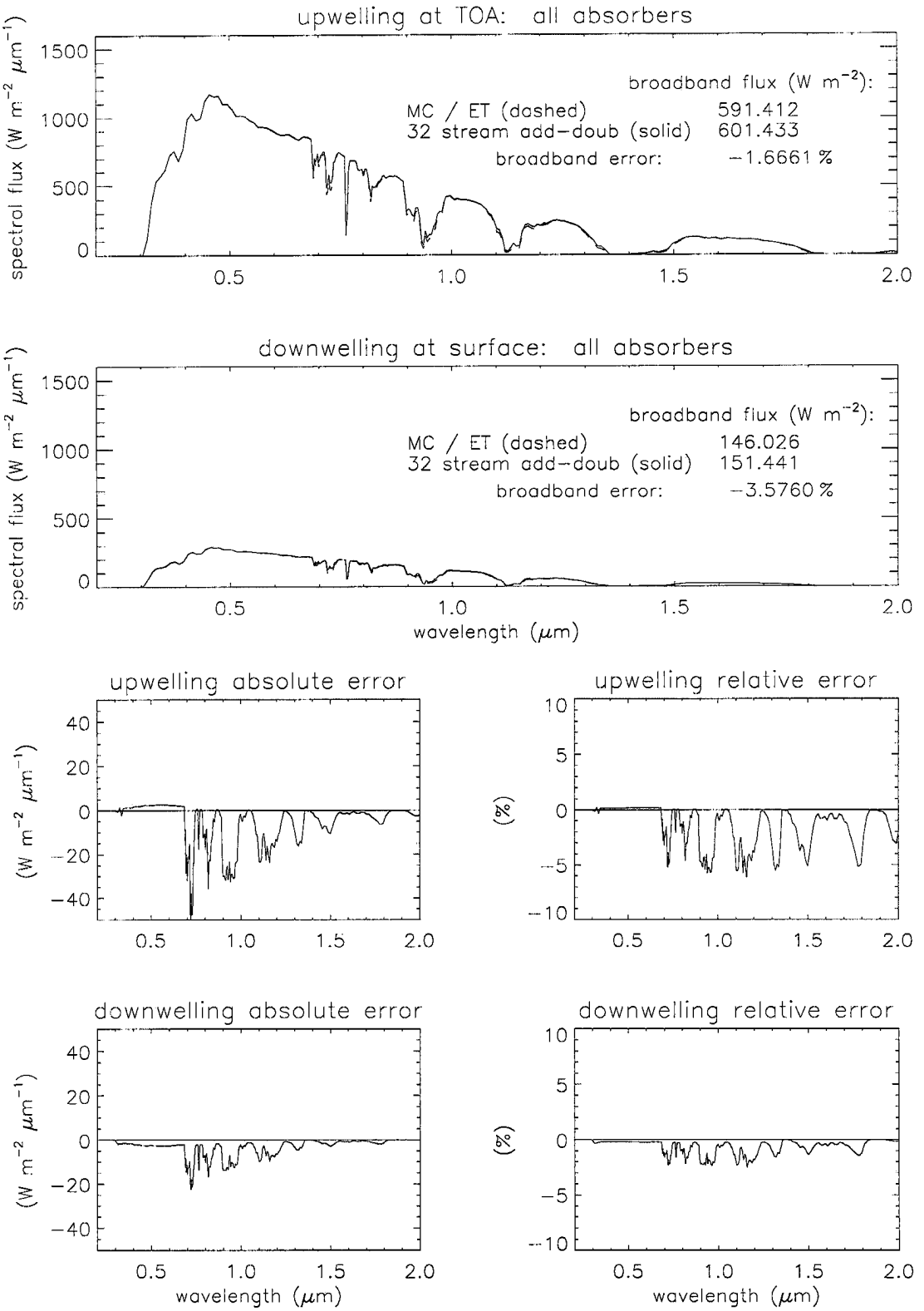

Figure 5.13: Comparison of results from MC/ET and the 32-stream adding doubling model when surface, cloud, and gas absorptions are accounted for.

Chapter 6

ACCURATE MC/ET SIMULATION OF THE SHORTWAVE SPECTRUM

6.1 Introduction

In the previous chapter, the modified Equivalence Theorem was developed and shown to be effective in simulating high spectral resolution gas, cloud, and surface absorption in a wavelength interval where the scattering properties of the atmosphere are assumed to be constant. Simplifying assumptions were shown to work reasonably well for the shortwave solar spectrum in which the scattering properties of a ScI cloud change little. However, to increase accuracy, the region from .2 to $4\mu m$ should be divided into intervals. In addition to this, subdivision of the shortwave region is required if Rayleigh scattering is to be used in model simulations. Rayleigh scattering varies dramatically in wavelength and, therefore, the assumption that one Rayleigh optical depth can approximate the optical depth across the spectrum is very poor and will result in large errors.

This chapter discusses the method used in choosing the optimal number of intervals that will be used for the experiments in the following chapters. Also, errors resulting from dividing the shortwave spectrum into those intervals will be shown as the MC/ET method is compared to the 32-stream adding- doubling model run at full resolution. These errors on the whole are 1% for broadband fluxes.

6.2 Subdivision of the Shortwave Spectrum

The goal of this procedure is to divide the shortwave spectrum into the fewest number of intervals possible without sacrificing too much accuracy. A low number of intervals translates to less computation time required. Error for the minimization scheme is defined

as the comparison between a model run with a few intervals compared to the same model run using scattering properties at full resolution.

The scattering properties that determine how a photon behaves in this study are cloud extinction coefficient ($\sigma_{ext,cld}$), cloud asymmetry factor (g) and Rayleigh extinction coefficient ($\sigma_{ext,ray}$). There are many ways to create a scheme that will result in a fewer intervals over which a radiative transfer model is run. For example, regions can be chosen in which the average scattering properties are calculated and used in each Monte Carlo run. This, however, can lead to discontinuities at interval boundaries unless some sort of interpolation is used. If interpolation is employed, then the use of interval average scattering properties becomes less accurate. Instead, a better method of spectrum subdivision involves choosing wavelengths which, upon the use of linear interpolation, will reproduce the scattering properties of Fig. 3.4. If these model inputs are well described by the chosen points, then perhaps the interpolated output flux between these wavelengths will be accurate. This eliminates the concept of the interval and replaces it with discrete nodes between which interpolation is used. Hence, the model must be run at least once for each end of the shortwave spectrum. The nodes in between are derived from an error minimization scheme.

The method used in this study to find the locations of these nodes is slightly different than described above. The reason for doing this minimization is to describe the most accurate spectral variation in flux and scattering statistics that are output from the Monte Carlo model which are input to the modified Equivalence Theorem routine. Therefore, rather than being concerned about how well the nodes can reproduce the input scattering properties, they must simply reproduce the final flux and scattering statistics. The results of this minimization may be applied to any model which uses the same 287 wavelength bands and an atmosphere whose clouds have the scattering properties of a ScI cloud.

The complete theory behind the minimization scheme used is described as follows. First, the 32-stream adding-doubling model was run for a variety of conditions which best represent those that will be encountered in later experiments. These conditions included four solar zenith angles (40, 50, and 60 degrees) and six ScI cloud $\sigma_{ext,cld}$ realizations.

These realizations were simply the spectral $\sigma_{ext,cld}$ for a cloud 1 km thick multiplied by a factor ranging from 1 to 0. This represents clouds of different geometric or optical thickness while retaining the spectral variations of the ScI cloud. In addition to this, Rayleigh scattering as a function of wavelength was also used. The other parameters were set in the same way they would be used in the Monte Carlo run: $\omega_o = 1, \alpha = 1$, and no gas absorption. These conditions require specific assumptions concerning the interpretation of the results. First, spectral upwelling flux at the top of the atmosphere is constant. Because there is no absorption, every photon that enters the atmosphere must leave resulting in identical upwelling and downwelling fluxes at TOA. Therefore, it is assumed that nodes chosen solely by comparing downwelling flux errors at the surface will also be a good approximation for the upwelling flux at TOA. Second, it is assumed that the scattering statistics can be linearly interpolated between nodes in the same manner as flux. Both of these assumptions will be tested when the MC/ET results are compared to the results from the 32-stream at the end of this chapter.

The adding-doubling model was run using the full resolution (287 band) cloud and Rayleigh scattering properties and returned the downwelling spectral flux for each of the solar zenith angle and cloud $\sigma_{ext,cld}$ conditions stated above. These results are plotted in the top row of Fig. 6.1. There is one panel for each solar zenith angle and each panel contains the normalized flux results for six cloud $\sigma_{ext,cld}$. The darkest line represents results using the unchanged ScI $\sigma_{ext,cld}$ and the lightest line represents results for which only Rayleigh scattering was present (clear sky). The minimization scheme then processed these results to determine where nodes should lie. To do this, the normalized flux was multiplied by the incoming solar flux at TOA for absolute and relative error analysis. Next, a step by step process was invoked:

1. Node 1 was set at .2 μm and node 2 at 4 μm.

2. The spectral flux was linearly interpolated between these two points for all conditions. If the flux at any wavelength in the resulting spectrum differed from the spectral flux calculated with full resolution by more than 6 $Wm^{-2}\mu m^{-1}$ or 10%,

then the node 2 was moved closer to node 1 by one band. This was repeated until all fluxes between the two nodes were below these error thresholds.

3. Once error thresholds were not exceeded, node 3 was introduced at 4 μm and step (2) commenced between nodes 2 and 3.

4. The above was repeated until the errors across the shortwave spectrum were below the thresholds.

This minimization scheme resulted in five nodes which are listed in Table 6.1. Right away, it is seen that most of the nodes are located in the shortest wavelengths. This indicates that flux results from the changes in Rayleigh scattering are large compared to those due to changes in cloud scattering. The second and third rows of Fig. 6.1 show the absolute and relative errors, respectively. According to these plots, the largest fluctuations in absolute error occurs in the shorter wavelengths where changes in Rayleigh scattering dominates and the largest fluctuations in relative error occurs around 3 μm where changes in cloud scattering dominates.

Table 6.1: Results from the error minimization scheme to subdivide the shortwave solar spectrum.

node	wavelength (μm)	$\sigma_{ext,cld}$ (km^{-1})	g_{cld}
1	0.218	37.759	0.85747
2	0.375	39.538	0.84350
3	0.495	40.900	0.84223
4	0.726	40.093	0.82692
5	3.810	52.641	0.77048

6.3 Model Performance

From the previous section it is known that the output flux from the Monte Carlo model (or any model for that matter) run at the above five wavelengths should not deviate more that 6 $Wm^{-2}\mu m^{-1}$ or 10% from the results when the model is run at full resolution (i.e. 287 nodes or wavelengths). However, to gain a perspective on how this decrease in

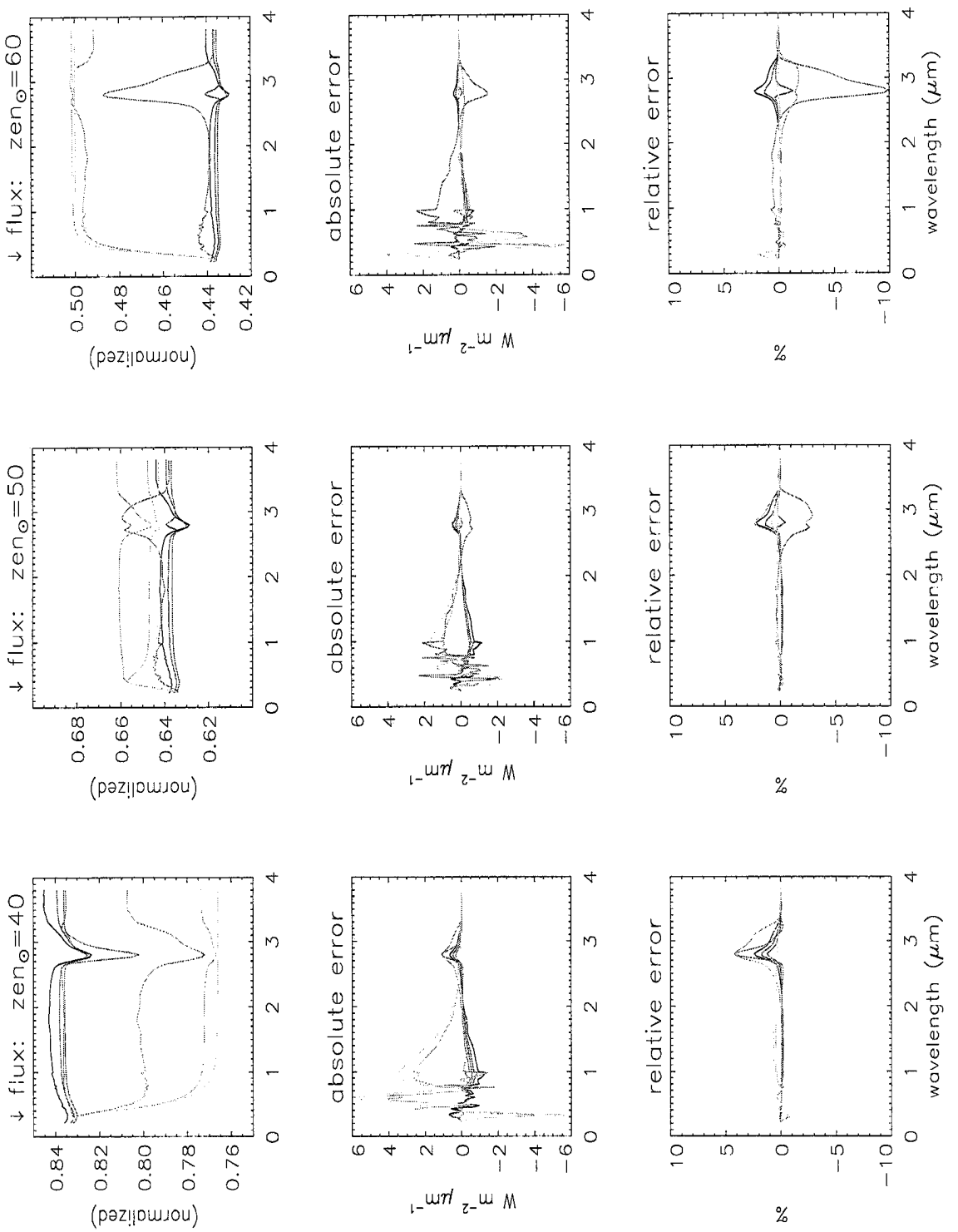

Figure 6.1: Results from the error minimization scheme to subdivide the shortwave solar spectrum. The first row is the output normalized flux from the 32-stream model run at full resolution. The second and third rows are the absolute and relative errors incurred when the full resolution flux is approximated by 5 nodes and linear interpolation.

cloud scattering resolution affects the comparison between the MC/ET method and the 32-stream adding doubling model, the same type of error analysis employed in the previous chapter is shown in Figures 6.2 and 6.3.

The cases shown include one for no absorption and one for all absorbers run for the MC/ET model using the five nodes versus the adding-doubling model run at full resolution. The case without absorption (Fig. 6.2) reveals errors that are comparable to those seen when both models were run for $\sigma_{ext,cld} = 40$ and $g = .85$. If the MC/ET model were run at full resolution, almost identical errors would be expected. However, the slight increase in broadband downwelling flux error from .86% to 1.05% is indicative of the error that the use of five nodes and linear interpolation has introduced. The spectral absolute and relative errors are almost identical except for some variation in the downwelling fluxes. When all absorbers are accounted for in the models, errors depicted in Fig. 6.3 result. In this case, the broadband errors are small when compared to those in the previous chapter. The upwelling error has decreased from 1.67% to .05% and the downwelling error has decreased from 3.58% to 1.14%. However, these errors are fortuitous, resulting from the almost even distribution of absolute spectral error about 0. A further investigation of the cause of these errors is be required and will be the subject of future study. They could result from a variety of possible sources including the merging of the adding-doubling source code with the k-distribution routine or numerical error in the modified Equivalence Theorem code. Otherwise, the variation in spectral errors is comparable to those in the previous chapter.

To demonstrate that the broadband error between the MC/ET model and the 32-stream is within acceptable error bounds, it was compared to similar results from the study of Hignett and Taylor (1996). In that study, upwelling flux above cloud level and downwelling flux below cloud level computed from a 5 band Monte Carlo model is compared to fluxes from the Slingo-Schrecker scheme (Slingo and Schrecker, 1982). Although the simulated atmospheres were different between the present study and that of Hignett and Taylor the errors between the Monte Carlo models and the "benchmark" for both studies are shown in Table 6.2. As seen, the relative errors between the MC/ET and 32-stream

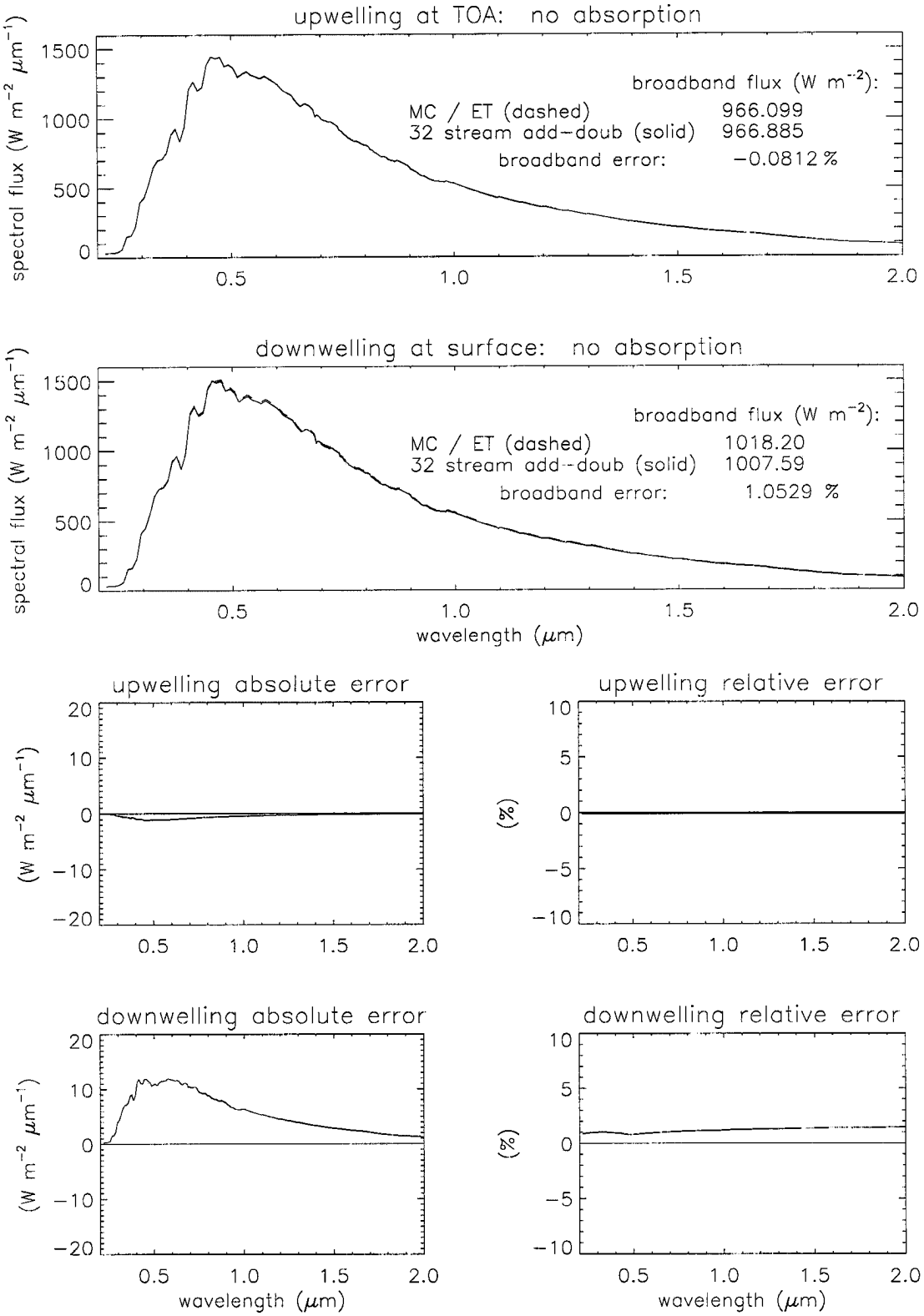

Figure 6.2: Comparison of results from MC/ET and the 32-stream adding doubling model without any atmospheric absorption.

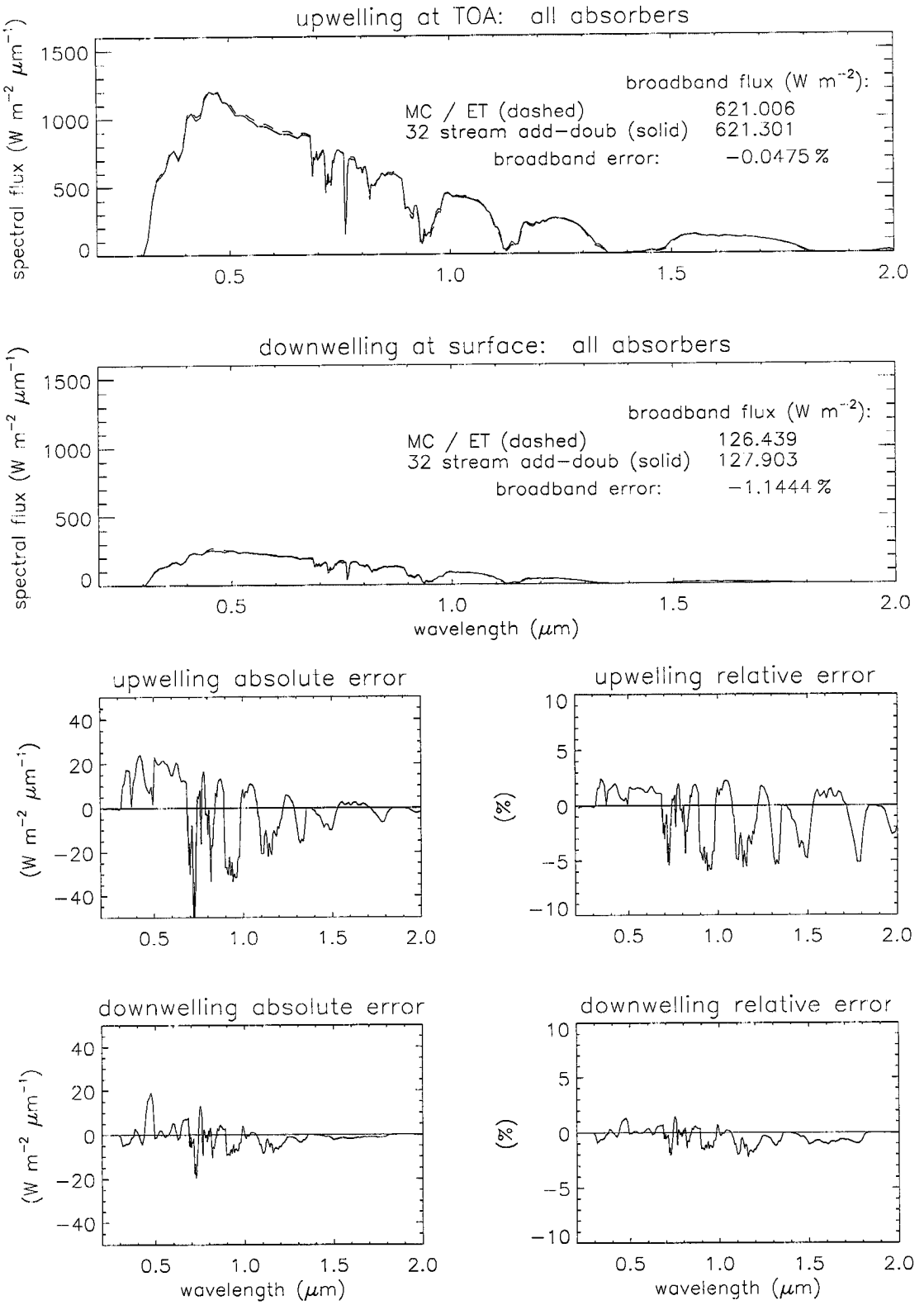

Figure 6.3: Comparison of results from MC/ET and the 32-stream adding doubling model when gas, surface, and cloud absorption is used.

models are well below those in Hignett and Taylor. Usually, errors tend to increase with atmosphere complexity. The model atmosphere in Hignett and Taylor consisted of a single layer cloud with optical depth 10, no absorbing water vapor, no Rayleigh scattering, and no reflecting surface. The present study included a single layer cloud with an optical depth around 40 (depending on spectral position), four absorbing gases, Rayleigh scattering, and a spectrally reflecting surface. For this reason, the MC/ET model appears to perform very well. Of course, some extra error is expected in the Hignett and Taylor comparison because the Monte Carlo model consisted of 4 bands whereas the Slingo-Schrecker scheme consisted of 24 bands.

Table 6.2: relative errors between MC/ET and 32-stream (denoted "present study") and between the Monte Carlo model of Hignett and Taylor (1996) and the radiation scheme of Slingo and Schrecker (1982) (denoted "H & T (1996),").

	H & T (1996)	present study
$F_{up,top}$	1.76%	0.0475%
$F_{dn,bot}$	−3.89%	−1.14%

6.4 Summary

In this chapter, the need to subdivide the shortwave solar spectrum and the method employed to do so were discussed. The approximation of the wavelength dependent scattering properties of cloud and gas each by one number can lead to significant error when compared to real world observations. However, to use the full resolution properties would require the Monte Carlo model to be run 287 times for the present wavelength bands. Through the use of error minimization it was concluded that only five Monte Carlo calculations are required to approximate the solar shortwave spectrum and to keep that approximation within acceptable error bounds. The location of these five nodes was primarily dictated by the variation of Rayleigh scattering at short wavelengths. In the following chapters, the MC/ET model using this information will be employed to perform studies of the effect of cloud heterogeneity on absorption of solar radiation and to simulate observed fluxes from airborne measurements.

Chapter 7

EXPERIMENTS AND RESULTS I: THE THEORETICAL EFFECT OF CLOUD HETEROGENEITY

7.1 Introduction

The purpose of the experiments in this chapter is to answer some of the questions posed by past researchers as discussed in Chapter 2. With the development of the MC/ET model, the role of cloud heterogeneity on the absorption of solar radiation by gas and cloud particles can be assessed. For simplicity, aerosol effects will not be addressed in the current study.

The first section defines the parameterization of the model surface and cloud and gas atmospheres. Next, the problem of assessing the effect of cloud heterogeneity on solar absorption by gas and cloud particles will be investigated in three experiments. For these experiments, internal heterogeneity is defined as the non-uniform distribution of cloud extinction within a single cloud parcel, whereas spatial heterogeneity defines the arrangement of each parcel with respect to others. First, spatial effects as described by cloud fraction will be investigated. For this experiment, each cuboidal cloud contains identical and uniform extinction. The size of the parcels is changed to represent different cloud fractions. Second, the effect of internal heterogeneity will be studied with a fractal cloud model. For this experiment, the cloud fraction is one although the extinction in the cloud is not uniform. Following this, the effects of spatial and internal heterogeneity will be combined in a case study involving cloud fields obtained from the Landsat satellite. For each experiment, the broadband and spectral characteristics of absorption and albedo will be explored and compared to results obtained using the plane-parallel approximation.

7.2 The Model Atmosphere

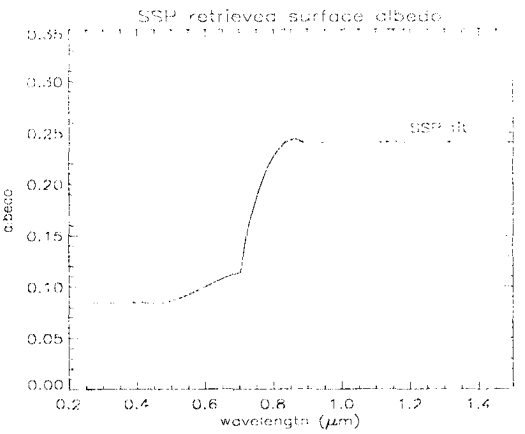

Figure 7.1: Fit to the SSP retrieved ARESE surface albedo used in all experiments

7.2.1 Cloud Characterization

All of the following experiments consist of different cloud amounts located between 1 and 2 km above ground. This cloud altitude is approximately the same as the cloud layer observed on 30 October 1995 during the ARESE IOP. As previously mentioned, the cloud type chosen was a stratocumulus I (ScI) cloud (Stephens, 1979) which has a visible optical depth near 37. This describes a low level, optically thick cloud.

7.2.2 Surface Characterization

To reproduce realistic fluxes in the model simulations, the spectral dependence of surface absorption is important. For this reason, a spectral surface albedo was obtained from observations during the ARESE campaign. By combining measured clear sky upwelling spectral flux from the Scanning Spectral Polarimeter (SSP) and downwelling spectral flux from a clear sky model run, the spectral surface albedo was retrieved. A more precise description of how this retrieval worked will be presented in the next chapter when simulations of ARESE case studies are discussed. The spectral albedo used for the experiments in this chapter is plotted in Fig. 7.1

7.2.3 Gas Profile

As noted in Chapter 5, the Equivalence Theorem uses the densities of four gases (H_2O, CO_2, O_3, and O_2) to compute fluxes which include the effects of gas absorption.

Gas amounts as discussed here are in terms of mixing ratio (q in g/g) but are easily converted to density (ρ_g in $g \cdot cm^{-3}$). CO_2, O_3, and O_2 mixing ratios were taken from the standard mid-latitude summer profile for all experiments. H_2O mixing ratios, on the other hand were derived from radiosonde data taken during ARESE. The reason for this lies in the necessity that the cloud layer be saturated with respect to water vapor. The mid-afternoon sounding from 30 October 1995 is shown in Fig. 7.2. The saturation of the cloud layer is evident in the overlapped temperature and dew point curves. The derived H_2O mixing ratio along with the mid-latitude summer O_3 mixing ratio are shown in Fig. 7.3. The mixing ratios for CO_2 and O_2 are not shown because they are constant in altitude at 5.013×10^{-4} and .2314 g/g, respectively. These gas profiles are the same for all of the following experiments. Even if there is no cloud present in the model atmosphere, the layer between 1 and 2 km is saturated.

7.3 Spatial Heterogeneity and the Redistribution of Radiation

The purpose of this experiment is to determine what role the spatial distribution of extinction in the form of cloud amount or cloud fraction (A_c) has in changing gaseous and cloud absorption. This is compared to results obtained when the model is run using the plane-parallel approximation.

The procedure involved "growing" cuboidal clouds in a model atmosphere. The clouds were regularly spaced and periodic. The centers of the clouds were 4 km apart. The model run started with clear sky (cloud fraction 0) and continued until the edges of the clouds touched, thus creating a plane-parallel layer (results as a function of cloud fraction are plotted from 1 to 0 to represent increasing spatial heterogeneity). The optical depth of the clouds were kept constant at the nodal values for a ScI cloud. Thus, the area averaged optical depth increased from 0 to the ScI values (about 40 at visible wavelengths). Information output from each run included upwelling and downwelling spectral and broadband fluxes at 0 and 10 km and the scattering and path length probability density functions associated with each flux measurement.

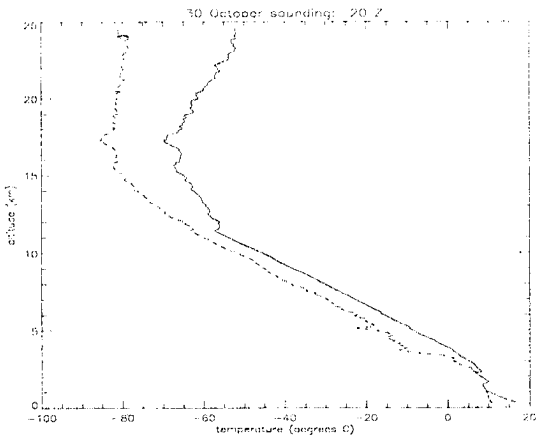

Figure 7.2: Temperature (solid) and dew point (dashed) profiles for 30 October 1995.

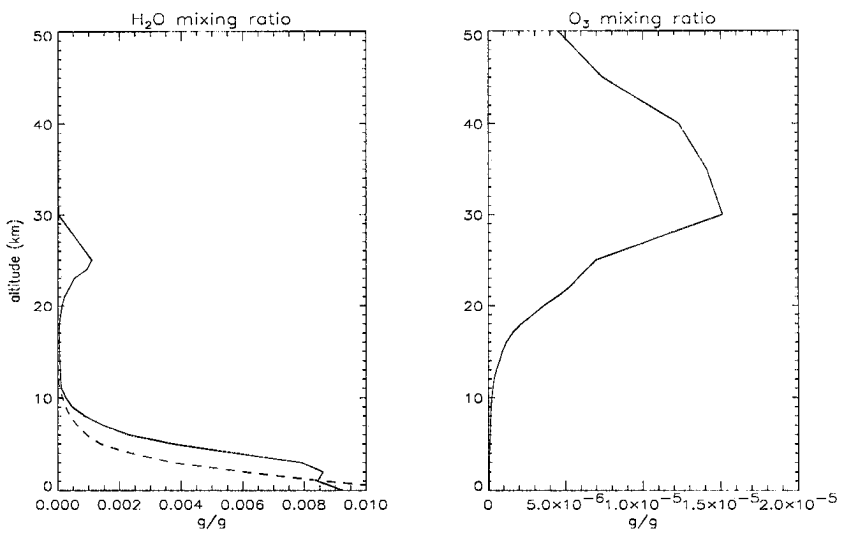

Figure 7.3: Gas profiles used as model input. H_2O profile to 24 km is obtained from 30 October 1995 sounding. The H_2O profile above 24 km and O_3 profile are from standard atmosphere mid-latitude summer data. The dashed curve in the H_2O mixing ratio profile is the standard mid-latitude mixing ratio for comparison.

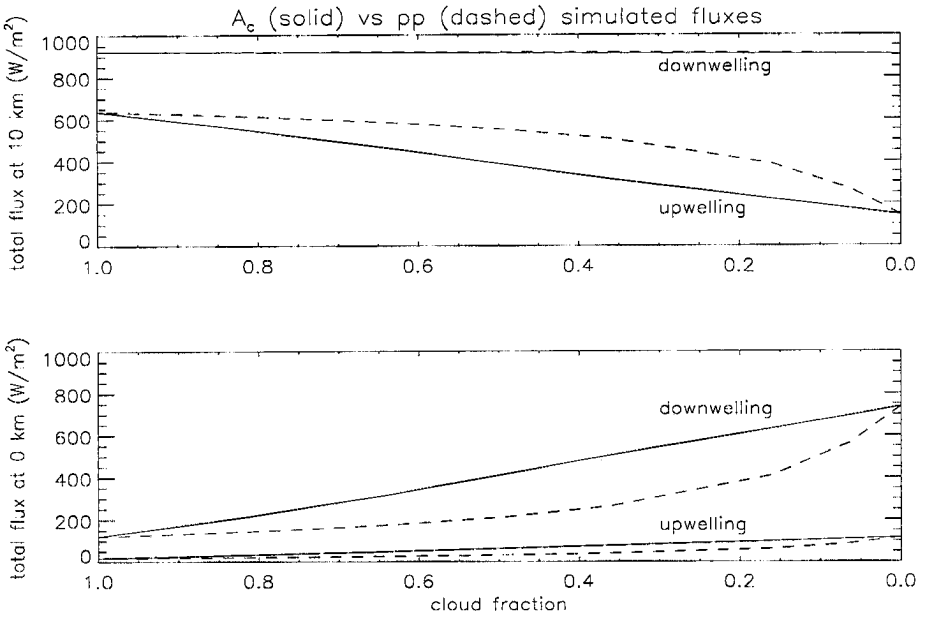

Figure 7.4: Upwelling and downwelling fluxes at 10 km (top) and 0 km (bottom) as a function of cloud fraction for ScI cloud between 1 and 2 km. The water vapor profile is saturated in the cloud layer. Dashed curves indicate plane-parallel fluxes for area averaged optical depth corresponding to each cloud fraction.

7.3.1 Fluxes and Total Atmospheric Absorption

The simulated fluxes resulting from this experiment can be seen in Fig. 7.4. The top panel shows the downwelling and upwelling flux at 10 km. The downwelling flux is nearly constant because the solar zenith angle is set at 45 degrees for all cases. This flux does show slight variation due to Rayleigh scattering of upward flux above 10 km. Upwelling flux decreases from the value for overcast sky (A_c=1) as cloud amount decreases. The dashed curve indicates the reflected flux for a plane-parallel atmosphere with the same area averaged optical depth. The lower panel displays the downwelling and upwelling fluxes at the surface (0 km). Transmission increases as the model atmosphere becomes more clear. Again, the dashed curves indicate the fluxes for an equivalent plane-parallel atmosphere. As seen in these results, the plane-parallel approximation overestimates reflectances and underestimates transmittances.

The total broadband absorption of solar flux is plotted Fig. 7.5. As the cloud cover decreases, so does the total atmospheric absorption (solid line). The range of absorp-

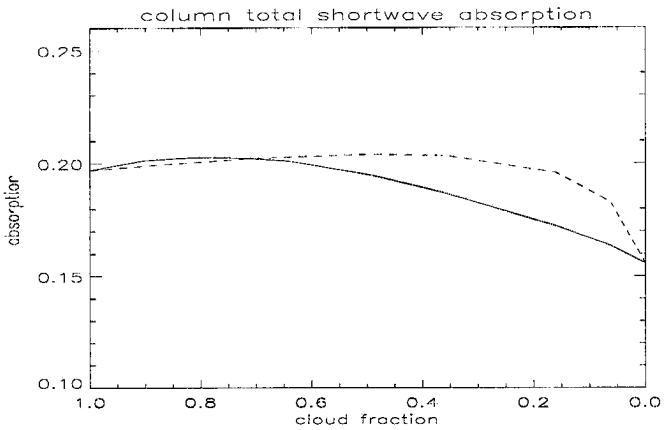

Figure 7.5: The total column absorption for the case in Fig. 7.4. Dashed curve indicate plane-parallel values for area averaged optical depth corresponding to each cloud fraction.

tions is around 20% for mostly cloudy conditions to 15.5% for clear sky. Although many researchers have questioned the plane-parallel approximation as possibly the root of the absorption discrepancy, the horizontally uniform model atmosphere actually leads to an increase in total absorption for cloud fractions less than .7 for this case. However, the total absorption for fractional cloud cover is slightly larger than that of the plane-parallel cloud for cloud fractions above .7.

To investigate the spectral features of absorption, the cloud fraction of .36 will be studied. For this geometry, the plane-parallel approximation overestimates atmospheric absorption by about 2%. The spectral differences are small, but most noticeable beyond 1.5 μm. In this region, gas and cloud absorb solar radiation. Below 1.5 μm, gas is primarily responsible for total absorption. To gain a better understanding of the roles of cloud and gas, the two effects are separated and discussed in the following two sections.

7.3.2 The Effect of Cloud

The amount of cloud absorption was calculated by running the modified Equivalence Theorem without gas absorption and performing the same flux differencing technique that was used to obtain total absorption. Gas absorption is calculated in a similar manner, however cloud absorption was turned off ($\omega_o = 1$). This method of comparing contributions to total absorption is also seen in Herman and Curry (1984). In this way, the

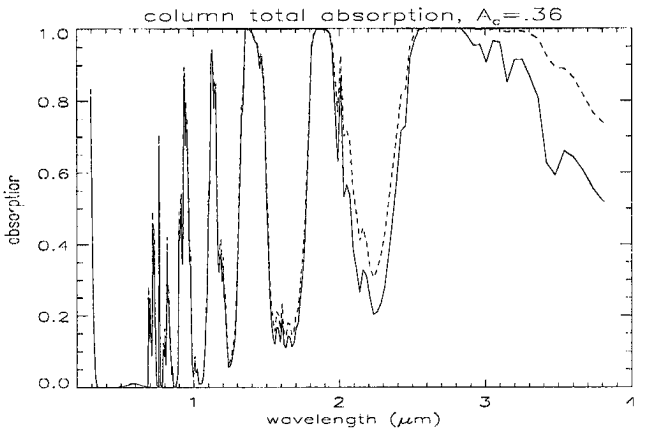

Figure 7.6: The spectral absorption for a cloud fraction of .36 (solid) compared to that obtained when the plane-parallel approximation (dashed) is used.

absorption is broken down into two components that approximately represent contributions to total absorption. This is not exact because gas or cloud absorption change when the other is included at the same time in the calculation. It simply gives a rough estimate of the importance of each constituent. Surface absorption was always present in these calculations.

The contribution to total absorption by cloud is plotted in Fig. 7.7. As expected, cloud absorption is maximum when cloud amount in the model atmosphere is maximum. This value is 6%. The difference between the plane-parallel and fractional cloud field indicates the effect of cloud distribution. The plane-parallel cloud absorbs more radiation. This effect is most dramatic at low cloud fractions where the plane-parallel cloud, though relatively thin, extends horizontally throughout the entire atmosphere and the fractional cloud, though thick, is arranged in widely separated cells. However, the difference in absorption between the two atmospheres at maximum is only 2 to 3%. This behavior is consistent with that reported by Stephens (1988a).

As discussed in Chapter 5, cloud absorption is accounted for in the modified Equivalence Theorem by using a scattering pdf. Therefore, the total column absorption using the flux differencing technique is dependent on four of these functions. Most information about cloud absorption can be inferred by looking at the functions that lead to upwelling flux above cloud and downwelling flux below cloud. Also, instead of comparing the en-

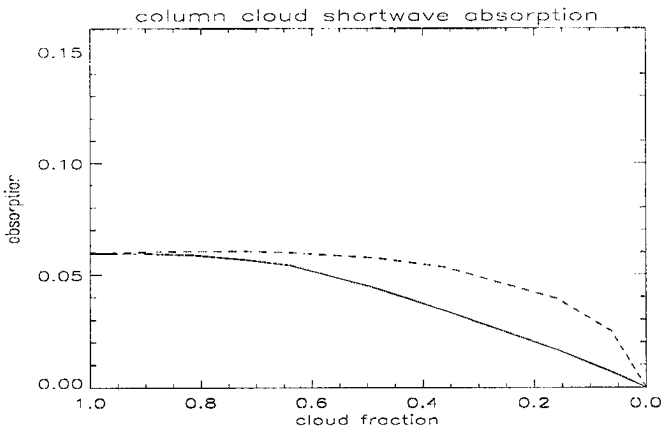

Figure 7.7: Cloud absorption for the case in Fig. 7.4. Dashed curve indicate plane-parallel values for area averaged optical depth corresponding to each cloud fraction.

tire pdf for each run, the average cloud scattering order for each can be studied. The downwelling pdf above cloud is insignificant because almost all photons that cross this measurement level have not yet interacted with the cloud. Likewise, the upwelling pdf at the surface contains no new information beyond that contained in the downwelling pdf. The average scattering order for a pdf of size S is obtained with the following relation:

$$\bar{s} = \sum_{s=0}^{S} s \cdot p(s) \tag{7.1}$$

Fig. 7.8 shows the average scattering orders for the upwelling flux above cloud and downwelling flux below cloud for the plane-parallel (dashed) and cloud fraction (solid) simulations. The plane-parallel average scattering order for both the top up and bottom down pdf always exceed those for the broken cloud (except when cloud fraction is 1 or 0, at which point they are equal). From this standpoint alone, higher cloud absorption in the plane-parallel runs is expected. However, it is interesting to note that most of the difference between the two occurs in bottom down scattering orders. The top up pdf is dominated by single or low order scattering events whether the cloud is homogeneous or broken. For the bottom down pdf, the photons have a better chance of reaching the surface through clear sky without undergoing a lot of scatters when the cloud is broken. Photons reaching the surface in the plane-parallel atmosphere must always travel through a substantial amount of cloud. As a result, the bottom down pdf provides more information about cloud heterogeneity.

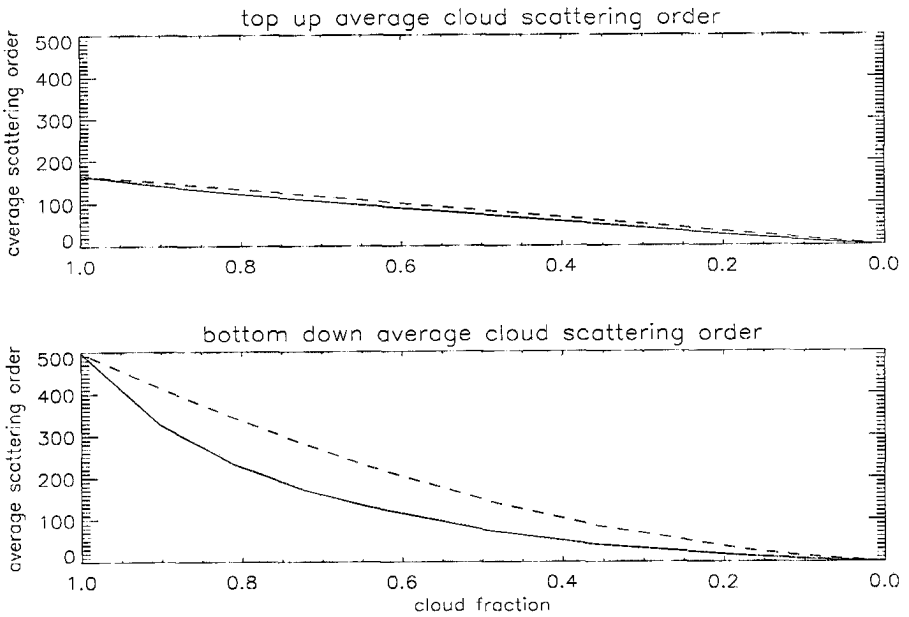

Figure 7.8: Average cloud scattering order as a function of cloud fraction (solid) or equivalent plane-parallel optical depth (dashed). Values were obtained from the .726 μm top up and bottom down cloud scattering pdf for each cloud scenario.

The difference between the plane-parallel and broken cloud top up and bottom down pdf can be seen in Fig. 7.9. The top up functions are very similar except for an almost constant offset. The effect of the broken cloud is seen at 0 and 1 scattering order. In the atmosphere containing a cloud fraction of .36, photons have a high probability of reflecting off the surface and crossing the above cloud flux measurement level without interacting with any cloud parcels. Similarly, this peak in probability is seen in the bottom down pdf. Here, however, the probability of low scattering orders is small for the plane-parallel cloud because photons usually undergo tens of scatters before emerging from cloud base.

Spectral absorption of radiation by the cloud in Fig. 7.10 resembles the behavior of the cloud single scattering albedo. Absorption features are more pronounced as a result of strong multiple scattering. This effect is exaggerated by the plane-parallel approximation where the cloud is almost completely absorbing around 3 μm.

7.3.3 The Effect of Gas

Like the procedure for determining the effect of cloud, the contribution of gas to total absorption was estimated by setting $\omega_o = 1$. Gas absorption is larger than cloud

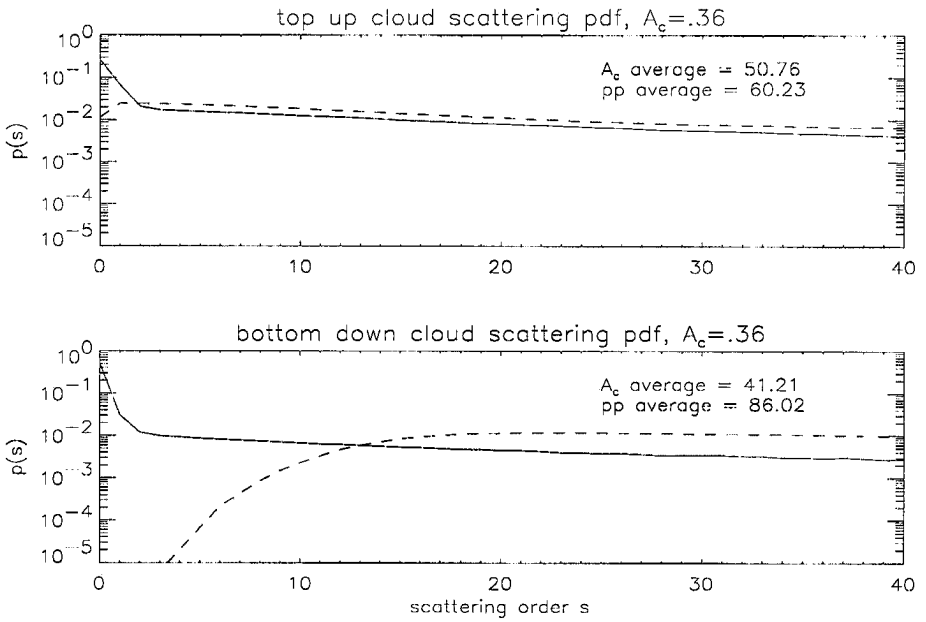

Figure 7.9: The .726 μm top up and bottom down cloud scattering pdf for cloud fraction .36 (solid) and equivalent plane-parallel optical depth (dashed) cloud geometries.

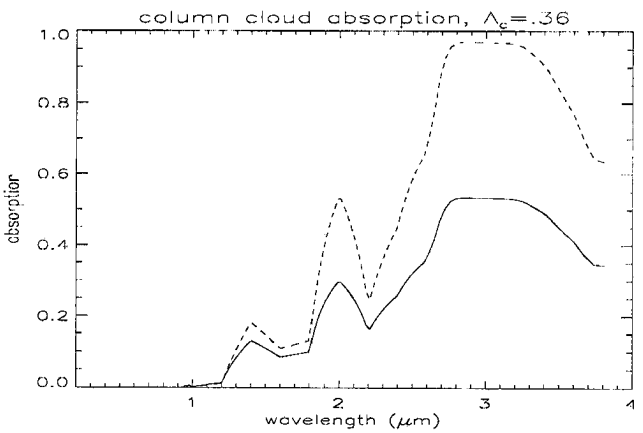

Figure 7.10: The spectral cloud absorption for a cloud fraction of .36 (solid) compared to that obtained when the plane-parallel approximation (dashed) is used.

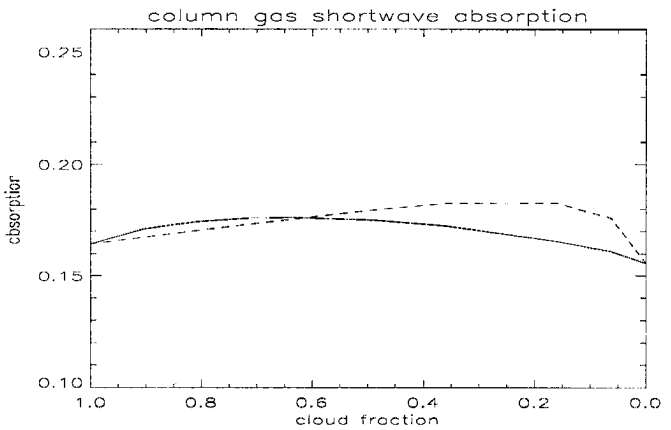

Figure 7.11: Gas absorption for the case in Fig. 7.4. Dashed curve indicate plane-parallel values for area averaged optical depth corresponding to each cloud fraction.

absorption by a factor of about 2.5 as seen in Fig. 7.11. The relative importance of gas seen here is higher than shown by Stephens (1978a) and opposite to that shown by Slingo and Schrecker (1982). But as Slingo and Schrecker (1982) note, many results are possible due to different relative amounts of water vapor and cloud water in the atmosphere. In comparing the results for the broken and plane-parallel cloud fields, it is seen that the peaks in gas absorption are widely separated in cloud amount. Broken cloud absorption is most pronounced near a cloud fraction of .65 and the homogeneous cloud absorption near an equivalent cloud fraction of .25. Here, the broken cloud absorbs more radiation for cloud fractions above .6 whereas the plane-parallel cloud absorbs more below .6.

Like average cloud scatter, the upwelling and downwelling average photon path lengths can be examined for insight into the behavior of gas absorption. Average path lengths are obtained from the path length pdf in the following manner:

$$\bar{l} = \int_0^\infty l \cdot \; p(l) dl \tag{7.2}$$

The average path lengths for the plane-parallel and broken fields are plotted in Fig. 7.12. Interestingly, the top up path lengths are similar and relatively invariant to cloud amount. The largest change occurs between clear sky and the first cloud simulation. It does not appear that the upwelling average path lengths hold much information about cloud absorption amount or cloud heterogeneity. The bottom down path lengths, on the other

hand, vary greatly with cloud amount. In addition, the average path lengths are different whether the cloud is broken or plane-parallel. At face value, this would indicate that the plane-parallel cloud always promotes higher gas absorption. However, the plot comparing gas absorption (Fig. 7.11) displayed more absorption for the broken cloud atmosphere above cloud fraction .6. This cannot be anticipated by looking at the average path length plots. This apparent discrepancy is due to the differences in reflectance and transmittance between the two cloud geometries. For the plane-parallel case, Fig. 7.11 shows a sharp increase in gas absorption between clear sky and thin cloud. This behavior is anticipated according to the downwelling average path length. This is interpreted as an increase in path length, and therefore absorption, due to the introduction of multiple scattering in the cloud layer. However, gas absorption soon subsides as the cloud gets optically thicker. At this point, a greater amount of radiation is reflected off cloud top and less radiation is allowed to pass through the lowest layers of the atmosphere where water vapor amount is high. At the same point, the broken cloud field allows a relatively higher amount of radiation to reach the lowest layers through gaps between cloud elements. Hence, gas absorption for the broken cloud field eventually overtakes that for the plane-parallel field. Similar arguments are presented in Stephens (1978a) and Slingo and Schrecker (1982) to explain decrease in gas absorption as a cloud gets thicker even though path lengths continue to increase.

The upwelling and downwelling path length pdf for a cloud fraction of .36 are shown in Fig. 7.13. Some information about where photons have been is contained in these plots. For a solar zenith angle of 45 degrees, the straight line path from the to of a 50 km atmosphere to the surface is 70.7 km. The bottom down path length pdf for broken cloud (solid line) shows a large probability of photons traveling 70.7 km. These photons reach the surface without much cloud or Rayleigh scatter. The plane-parallel pdf also shows a peak at this path length, but it is much smaller. Therefore, not as many photons are reaching the surface, or when they do, they undergo many cloud scatters which changes the path length. Similarly, the direct path from the top of the atmosphere to the surface and straight up to the 10 km flux measurement level is 80.7 km. The broken cloud top

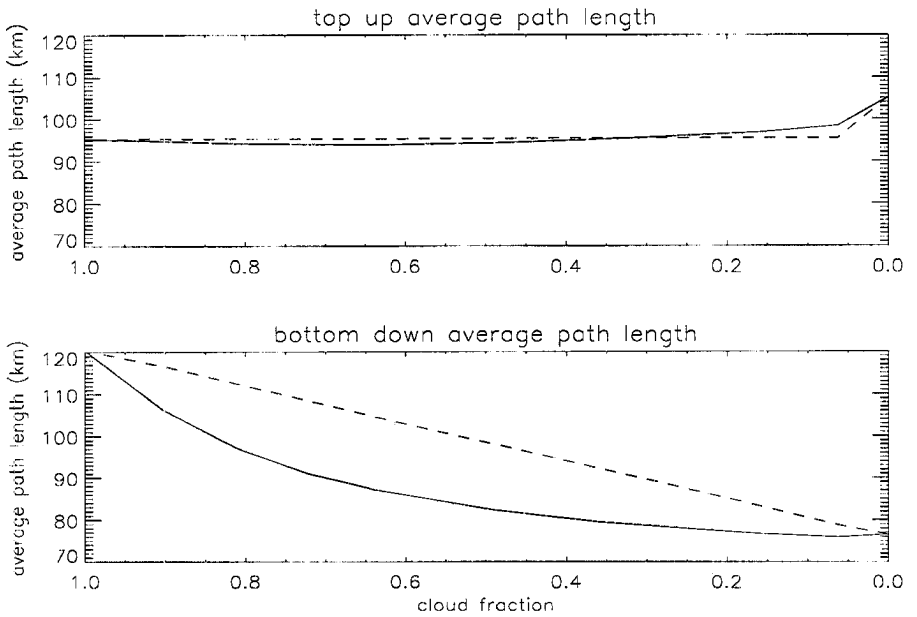

Figure 7.12: Average photon path length as a function of cloud fraction (solid) or equivalent plane-parallel optical depth (dashed). Values were obtained from the .726 μm top up and bottom down path length pdf for each cloud scenario.

up path length shows a peak at 80.7 km indicating that many photons have reflected off the surface. The plane-parallel pdf indicates that cloud interaction with photons is much more prevalent.

The spectral absorption of gas for a cloud fraction of .36 in Fig. 7.14 shows little difference from that for plane-parallel gas absorption. The primary reason for this is the fact that throughout the shortwave solar spectrum, gas is either nearly completely absorbing or nearly completely transparent. Differences at these two extremes should be small. The largest differences occur in wings of absorption bands between atmospheric windows and saturated absorption bands. In these areas, dramatic changes in absorption are occurring for both cloud geometries and the differences, though small, are more difficult to observe.

7.3.4 The Effect of Cloud Distribution on Albedo

As discussed in Chapter 2, albedo measurements are often compared to simulations to test model theory. There is a smaller chance of significant observation error because measurements are made simultaneously in space and time and there is no need to colocate

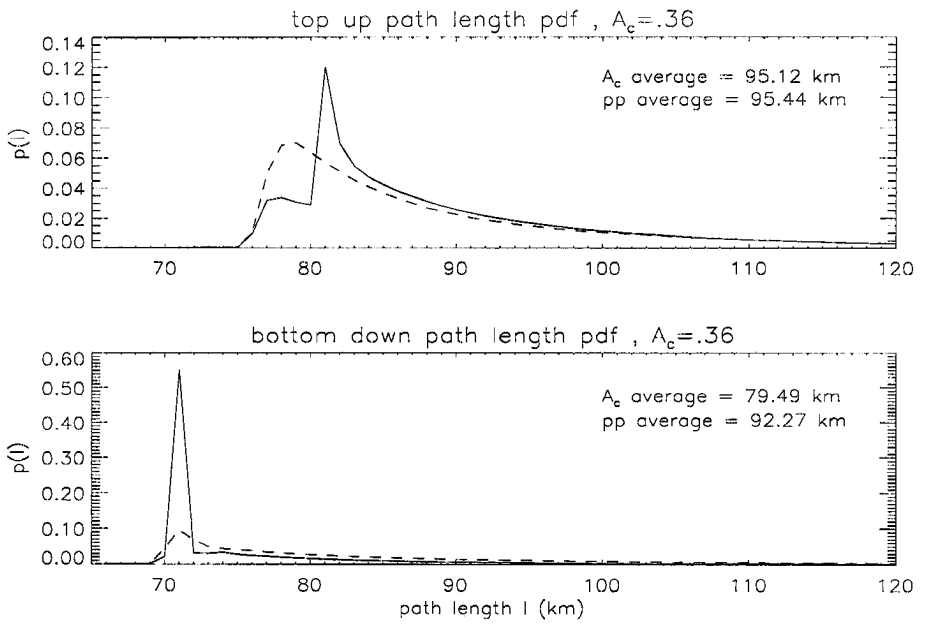

Figure 7.13: The .726 μm top up and bottom down photon path length pdf for cloud fraction .36 (solid) and equivalent plane-parallel optical depth (dashed) cloud geometries.

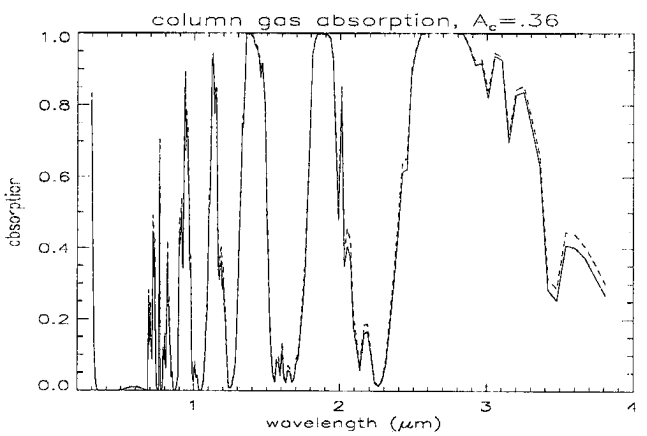

Figure 7.14: The spectral gas absorption for a cloud fraction of .36 (solid) compared to that obtained when the plane-parallel approximation (dashed) is used.

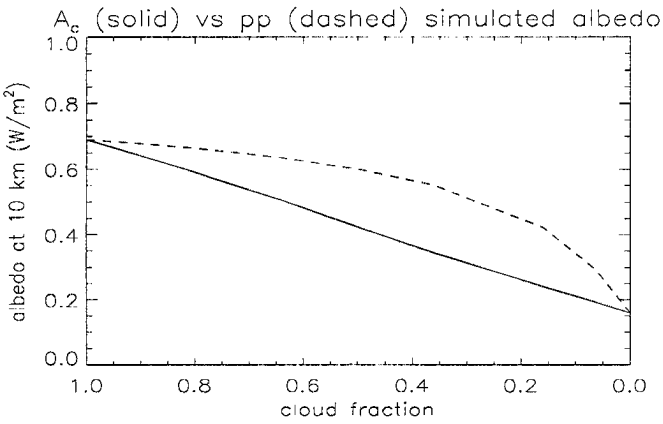

Figure 7.15: Albedo for the case in Fig. 7.4. Dashed curve indicate plane-parallel values for area averaged optical depth corresponding to each cloud fraction.

remote instruments. Also, if albedo measurements are made well above cloud level, sampling errors are reduced. However, as seen in the above experiment, cloud heterogeneity has a large effect on reflected flux. This effect is seen in Fig. 7.15 as a difference between plane-parallel (dashed) and broken cloud (solid) albedo. Here, the plane-parallel albedo is larger than the broken cloud albedo. As seen in Chapter 2, Zender et al. (1997) state that model albedo overestimation provides an indirect indicator of anomalous absorption. However, that study uses a plane-parallel model which artificially increases albedo. A caveat must be placed on their argument no matter how close an observed cloud is to plane-parallel: model albedo overestimation provides an indirect indicator of anomalous absorption if the cloud field geometry is accurately reproduced in the model atmosphere. The differences shown in Fig. 7.15 indicate that comparisons between simulated and observed albedo may be difficult in complex cloud situations with a one-dimensional model.

One method of removing the effects of cloud heterogeneity from albedo measurements is by calculating the ratio of NIR (.68 - 4.0 μm) to VIS (.2 - .68 μm) albedo. According to Hignett (1987), splitting the solar spectrum separates the effects of ozone and water vapor absorption in the VIS and NIR, respectively. By taking the ratio of the two albedos the effect of cloud particle scattering, which is similar in both regions, is reduced. For the

atmospheric column below 10 km, ozone absorption is small, so changes in the ratio will primarily be due to changes in water vapor absorption.

In the next chapter, the spectral characteristics of observed flux are not well resolved due to instrument limitations. Therefore, simultated flux at high resolution is used to fill in the gaps. As noted above, all fluxes and albedos are significantly affected by cloud heterogeneity. Therefore, direct simulations of cloud fluxes are not expected to match observations exactly. To combine observed spectral flux with model results, model spectral flux is forced to match the observed 0.5 μm spectral flux and all other model wavelengths are adjusted to the same relative degree. The principle that validates this operation is that highlighted by the albedo ratio. As an example, an upwelling flux ratio f_r will be used in the same manner as the albedo ratio R_r. The argument of Hignett (1987) still applies and the new ratio still contains the same information. The behavior of the flux ratio is the same as that of the albedo ratio, however the absolute value is different by a factor of C assuming the ratio of the NIR to VIS downwelling flux is constant:

$$R_r = \frac{R_{NIR}}{R_{VIS}} = \frac{F_{up,top,NIR}/F_{dn,top,NIR}}{F_{up,top,VIS}/F_{dn,top,VIS}} = \frac{F_{up,top,NIR}}{F_{up,top,VIS}} \cdot C = f_r \cdot C \tag{7.3}$$

Because the effect of cloud scattering is removed by the flux ratio, changes in this quantity should only be due to gas absorption. As seen in this experiment, gas absorption changes, albeit slight, when cloud morphology changes. Fig. 7.16 shows how this effect changes the flux ratio. Here, the broken cloud (solid line) and plane-parallel cloud (dashed line) upwelling flux ratio is plotted as a function of their respective upwelling VIS fluxes. The first feature to notice is that the difference in gas absorption between the plane-parallel and broken cloud fields does not change the flux ratio much as long as the ratio is plotted as a function of the upwelling VIS flux. The diamonds indicate, from left to right, plane-parallel optical depths of 0.0, 0.5, 0.16, 0.36, 0.49, 0.64, 0.72, 0.81, 0.9, and 1.0 times the full Scl optical depths. The squares indicate cloud fractions of the same values for the broken cloud field. At plane-parallel optical depths greater that a factor around .3 and cloud fractions greater than .64, the flux ratio is nearly constant. The significance of this plot is as follows: as long as the upwelling VIS flux is above 250 Wm^{-2}, the modeled cloud

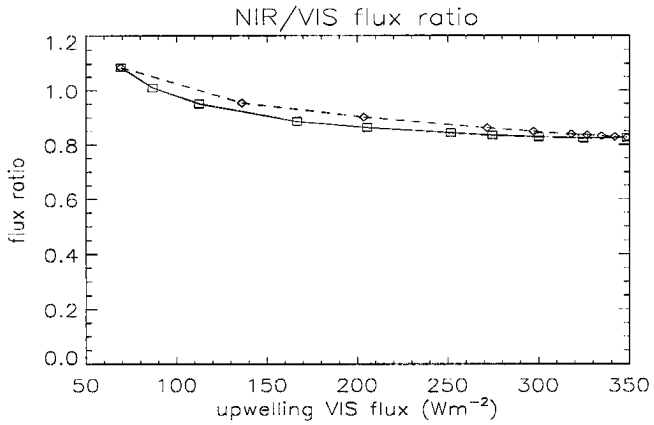

Figure 7.16: Upwelling NIR/VIS flux ratio for broken cloud (solid line) and plane-parallel cloud (dashed line) as a function of respective upwelling VIS flux. The diamonds indicate, from left to right, plane-parallel optical depths of 0.0, 0.5, 0.16, 0.36, 0.49, 0.64, 0.72, 0.81, 0.9, and 1.0 times the full Sc1 optical depths. The squares indicate cloud fractions of the same values for the broken cloud field. For upwelling flux values above 250 Wm^{-2}, cloud morphology and optical depth have very little impact on the NIR/VIS flux ratio.

plane-parallel optical depth can be underestimated by about 70% or the cloud fraction can be misspecified by 36% and the upwelling flux ratio should be accurate. Also, if cloud properties are tuned so that the upwelling VIS flux matches observations, the theoretical flux ratio is independent of cloud morphology.

The same relationships hold when spectral flux ratios are taken. Essentially, any measurement ratio will reduce the effects of cloud scattering. This is seen in Fig. 7.17 where the spectral ratios $0.87/0.5\,\mu m$, $0.818/0.5\,\mu m$, and $0.762/0.5\,\mu m$ are plotted. There is negligible gas absorption at .5 μm. The wavelengths 0.87, 0.818, and 0.762 are regions of strong water vapor, weak water vapor, and strong oxygen absorption, respectively. For all curves, a difference due to cloud morphology is only slightly seen.

Because the upwelling flux ratio is nearly constant for thick, overcast clouds, it is shown that when the spectral flux at a VIS wavelength changes, the flux at other wavelengths change to the same relative degree. This argument is assumed to apply to all measured fluxes.

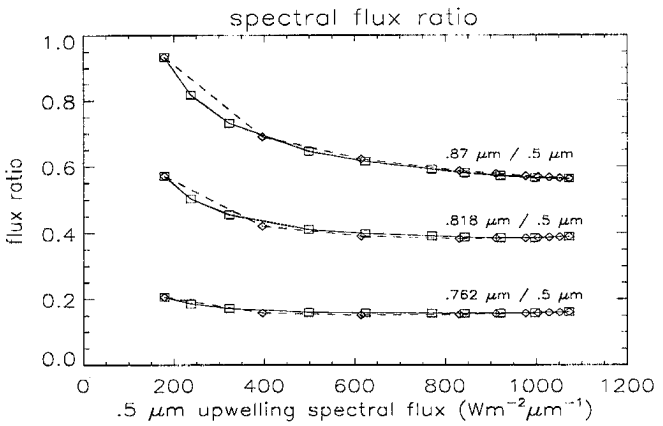

Figure 7.17: Same as Fig. 7.16, except for spectral wavelengths. The wavelengths 0.87, 0.818, and 0.762 are regions of strong water vapor, weak water vapor, and strong oxygen absorption, respectively

7.4 Internal Heterogeneity and the Redistribution of Radiation

In a broken cloud field, cloud parcels can seldom be considered homogeneous. Likewise, when the cloud fraction is 1.0, the cloud field will still exhibit some heterogeneity. These are examples of internal heterogeneity. To investigate the effect of internal heterogeneity on the redistribution of solar radiation, a fractal cloud field was used. A top-down view of the model cloud is shown in Fig. 7.18. The size of the cloud field was 32 km on each side and 1 km thick. Its location in the vertical was the same as for the cloud fraction experiment: 1 to 2 km. The same absorbing gas profile and reflecting surface was used. The cloud field in Fig. 7.18 has been normalized so that the area-average optical depth is 1.0 times the optical depth of a ScI cloud. The minimum and maximum optical depths were 0.328 and 2.488 times the ScI optical depth, respectively. This translates to ScI visible optical depths of 13.12 and 99.52. In effect, this cloud field was created by taking the cloud fraction 1.0 cloud from the previous experiment and redistributing the cloud mass using a fractal model. This experiment is less detailed than the previous one because only one realization of internal heterogeneity is used. In reality, there are an infinite number of ways the cloud mass can be rearranged and it is expected that each would affect the radiation field in a slightly different manner.

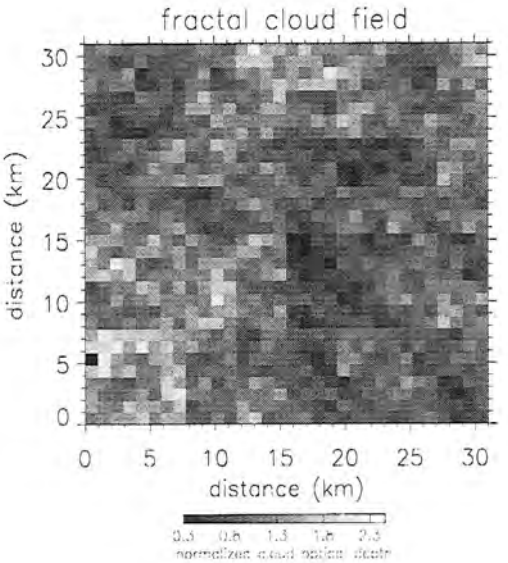

Figure 7.18: Fractal cloud field used to investigate the effect of internal heterogeneity. The cloud fraction is 1.0 and the minimum and maximum visible optical depths are 13.12 and 99.52

The fluxes from the fractal and plane-parallel cloud fields are listed in Table 7.1. The differences are fairly small. The plane-parallel cloud overestimates the upwelling flux above the cloud by 9 Wm^2 and underestimates the downwelling flux below the cloud by 10 Wm^2.

Table 7.1: Fluxes from the fractal cloud simulation compared to those computed using area-averaged optical depth.

flux (Wm^{-2})	fractal cloud	pp cloud
$F_{dn,top}$	922.449	922.623
$F_{up,top}$	627.922	636.508
$F_{dn,bot}$	130.732	120.874
$F_{up,bot}$	18.0911	16.610

Because the differences in the simulated fluxes are so small, small differences in atmospheric absorption are expected. Table 7.2 lists the calculated total, cloud, and gas absorptions. Not only is the difference in total absorption between the fractal and plane-parallel clouds small, it is negligible. However, this is the result of offsetting cloud and

gas absorptions. The plane-parallel cloud overestimates cloud absorption by 0.1% and underestimates gas absorption by 0.1%.

Table 7.2: Absorptions from the fractal cloud simulation compared to those computed using area-averaged optical depth.

absorption (%)	fractal cloud	pp cloud
total	19.7177	19.7102
cloud	5.8362	5.9482
gas	16.5224	16.4401

All of these absorptions are small. For clouds that are this thick, it appears that internal heterogeneity to the degree modeled here has little effect on atmospheric absorption. However, the slight bias between the plane-parallel and fractal cloud field does hold some information. Like the cloud fraction experiment, the more heterogeneous cloud exhibits less cloud absorption and more gas absorption. It is also seen in the previous experiment that absorption changes most rapidly when the cloud field is thin. Therefore, it is postulated that internal heterogeneity will play a larger role for thinner clouds and clouds which have larger pixel to pixel optical depth variability. Because the differences in fractal and plane-parallel absorption are so small for this experiment, a spectral absorption analysis would show little difference and is not presented.

7.5 Combining Spatial and Internal Heterogeneity: Landsat Simulations

After the effects of spatial and internal heterogeneity were investigated, the effects were combined by using a cloud dataset retrieved by the Landsat satellite. The full cloud data array and the cloud sub-scene that was used is shown in Fig. 7.19. The sub-scene was 9 km in length on each side and consisted of 8100 cloud pixels at 100 m resolution. The cloud fraction was .79. Cloud optical depth ranged from 1 at cloud edges to 101.2 at the thickest point. Once again, the cloud was 1 km thick between 1 and 2 km in altitude. Gas profiles were the same as for the previous experiments.

The resultant fluxes from the model simulations are listed in Table 7.3. The differences between the Landsat cloud field and the plane-parallel cloud field are significant, reaching

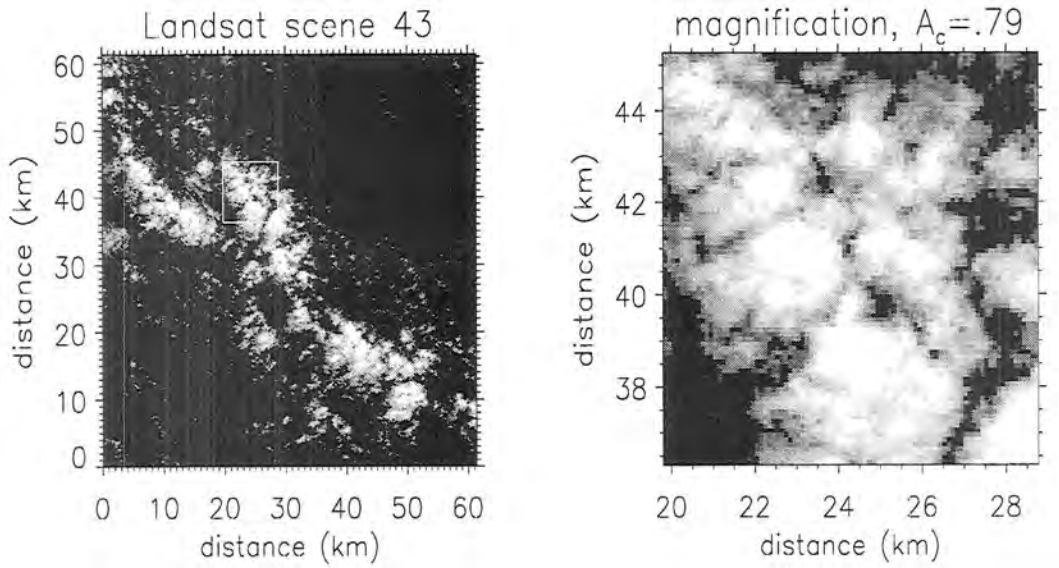

Figure 7.19: Scene from the Landsat satellite (left) and the portion of that scene used in the MC/ET model. The maximum cloud visible optical depth is 101.2.

almost 180 Wm^{-2} for downwelling flux below cloud. The upwelling flux difference is near 160 Wm^{-2} higher for the plane-parallel cloud. This translates to a 17% absolute difference in atmospheric albedo. Obviously, if the quantity of interest is flux or albedo, the plane-parallel approximation introduces a significant amount of error.

Table 7.3: Fluxes from the Landsat cloud simulation compared to those computed using area-averaged optical depth.

flux (Wm^{-2})	Landsat cloud	pp cloud
$F_{dn,top}$	917.904	921.751
$F_{up,top}$	448.053	610.571
$F_{dn,bot}$	328.369	146.584
$F_{up,bot}$	48.8412	20.428

However, upon looking at the total atmospheric absorption in Table 7.4, it is seen that the plane-parallel approximation introduces very little error. It underestimates total absorption by .7%, overestimates cloud absorption by .4%, and underestimates gas absorption by .9%.

Table 7.4: Absorptions from the Landsat cloud simulation compared to those computed using area-averaged optical depth.

absorption (%)	Landsat cloud	pp cloud
total	20.7346	20.0732
cloud	5.6386	6.0414
gas	17.9902	17.0733

Like the fractal cloud experiment, these absorptions are small because the Landsat cloud and the plane-parallel cloud are relatively thick. Though slightly broken and/or internally heterogeneous clouds produce some interesting absorption behaviors, their magnitudes are small even when the effects of spatial and internal heterogeneity are combined.

7.6 Summary

In this chapter, the theoretical effect of cloud spatial and internal heterogeneity on atmospheric radiometric fluxes, albedo, and absorption were studied. It was discovered that for cloud fractions greater than about 0.7 or an equivalent plane-parallel cloud optical depth, the horizontally homogeneous cloud does underestimate total absorption. However, the magnitude of this underestimation is only 0.25 to 0.5% for this cloud type and location. This degree of inaccuracy can be neglected in most modeling applications. Below 0.7, the plane-parallel approximation overestimates total absorption. The magnitude of this error is around 3.0%. This error may prove significant in some applications like general circulation modeling where the effects of a one-sided bias may accumulate. It was shown that for clouds of this type, spatial heterogeneity plays a more important role in changing absorption than internal heterogeneity. The differences between plane-parallel and heterogeneous fluxes and albedo are larger than absorption differences. Thus, to accurately simulate observed quantities, inclusion of cloud morphology information in radiative transfer models is important.

The most important point that the above experiments have shown is that the heterogeneity of low, thick water clouds cannot cause excess amounts of absorption using present absorption theory. This validates the use of plane-parallel models for nearly ac-

curate simulation of the absorptions in observed cloud systems. Accurate simulation of fluxes or albedos, however, is not described well when the plane-parallel approximation is used. This limitation is overcome by the use of the upwelling flux ratio. Comparing model results of this ratio with observed values should provide a rough indication of the spectral region where an anomaly in absorption might be occurring.

It must be emphasized that the results presented are not necessarily indicative of absorption behavior for other cloud types or altitudes. Furthermore, an in depth study of the effects of changing solar zenith angle and other distributions of cloud fraction and internal variability are needed to put absolute error bounds on the plane-parallel approximation. Now that a theoretical framework has been established, the observations made during ARESE are revisited in the next chapter. Comparisons will be made between the model and the observations to try and determine the nature of the absorption discrepancy in terms of broadband and spectral measurements.

Chapter 8

EXPERIMENTS AND RESULTS II: COMPARISONS OF SIMULATED AND OBSERVED ATMOSPHERIC ABSORPTION

8.1 Introduction

As seen in Chapter 2, observations made during ARESE and reported by Zender et al. (1997) and Valero et al. (1997) reveal that clouds appear to absorb more solar radiation than model simulations can predict. These case studies are revisited here where a more in depth look at the spectral signature of anomalous absorption is performed using knowledge gained from the experiments in Chapter 7 and the Scanning Spectral Polarimeter (SSP) flown on the Egrett aircraft.

Two case studies from ARESE have been chosen: 11 October (clear) and 30 October (overcast). According to the experiments in the previous chapter, direct simulation of observed flux is difficult resulting from poor cloud structure and microphysical data. However, an attempt was made to adjust cloud properties until above cloud upwelling and below cloud downwelling flux was reproduced. More specifically, the measurements of the .5 μm TDDR channel were reproduced because, according to Valero et al. (1997), no signs of absorption are present in this measurement as expected. Once model spectral flux was in close agreement with the TDDR .5 μm channel, comparisons were made with the higher resolution SSP upwelling spectral flux measurements. As discussed by Zender et al. (1997), albedo (or equivalently upwelling flux), provides an indirect measurement of atmospheric absorption. Therefore, if anomalous absorption is not present at .5 μm, it has a high probability of being manifested between the SSP wavelengths of .4 and 1.1 μm.

When simulating broadband VIS, NIR, and total shortwave flux, the spectral responses of the RAMS TSBR and FSBR instruments are used to modify model spectral

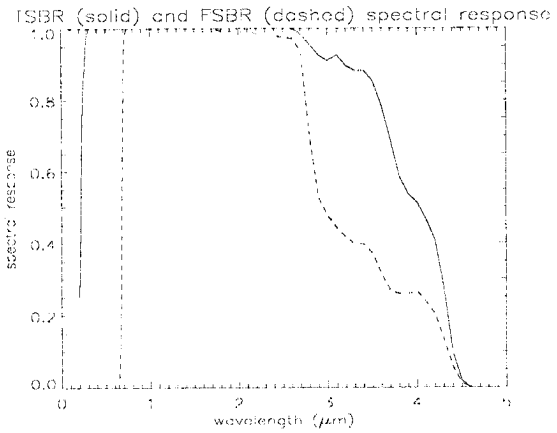

Figure 8.1: Spectral response functions of the RAMS TSBR (solid line) and FSBR (dashed line) pyranometers.

flux before integration. In this way, model output represents the same fraction of energy seen by the instruments. The TSBR and FSBR spectral responses are plotted in Fig. 8.1. Because the TSBR curve is near 100% for most of the shortwave solar region in question, total broadband flux output from the model is changed only very slightly. Likewise, for NIR broadband flux, the FSBR exhibits an almost square cutoff at .68 μm resulting in very little difference.

8.2 Surface Albedo Retrieval

If comparisons are to be made with high resolution upwelling flux instruments like the SSP, the spectral nature of the surface albedo is important. Because surface albedo can vary dramatically over land, surface measurements at the CART site were not used. Instead, albedo was retrieved from SSP measurements obtained during a low-level side by side instrument comparison flight on 11 October. The flight track followed by the two aircraft is shown in Fig. 8.2. By using the SSP measurements during this flight, a better representation of the area-averaged albedo is obtained. However, extrapolation of this albedo to the rest of the experiment flight paths (indicated by the dotted line) is an assumption at best. In addition to area-averaged albedo, measurements at the altitude of 2.93 km include the effect of low level aerosol. Zender et al. (1997) assume uniformly mixed mineral dust in the lowest 1 km and clean air above. The albedo retrieval used here

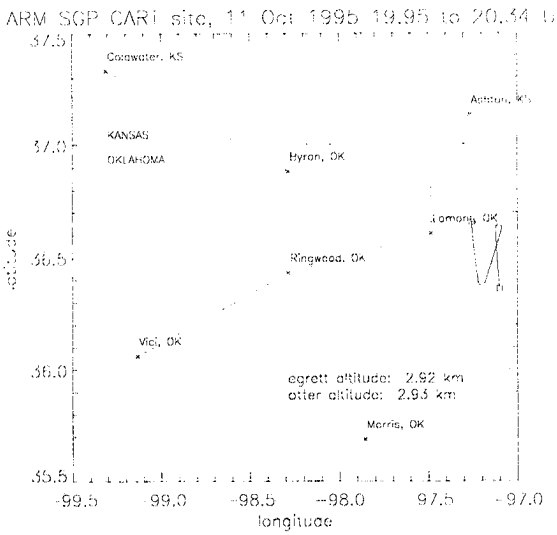

Figure 8.2: SGP CART site and aircraft flight strategies (dotted line). SSP measurements used for albedo retrieval were made during a three-leg low level instrument comparison flight.

implicitly includes the effect of aerosol absorption, though it is time invariant. It is also assumed that the effect of aerosol scattering on photon path length change is negligible.

The procedure for albedo retrieval included running the MC/ET model to get simulated downwelling SSP measurements at Egrett altitude. Once downwelling flux was obtained for the average solar zenith angle over the three flight legs, it was interpolated to SSP wavelengths and combined with the average SSP upwelling flux to obtain the SSP albedo plotted in Fig. 8.3. A curve was fit to the SSP albedo and a constant value was assumed below .4 μm and above .85 μm. Data above .85 μm was not used because SSP channels reside in strong water vapor absorption bands as indicated in Fig. 8.3.

8.3 ARESE Case Studies: Comparisons to RAMS Broadband and TDDR and SSP Spectral Quantities

8.3.1 11 October 1995

Unlike cloud cases, clear sky fluxes measured by the aircraft can be directly simulated without ad hoc adjustments to the optical properties of atmospheric constituents. The only parameters affecting simulated flux are the solar zenith angle, surface absorption, Rayleigh scattering, and gaseous absorption. As noted above, the effects of aerosol are limited to

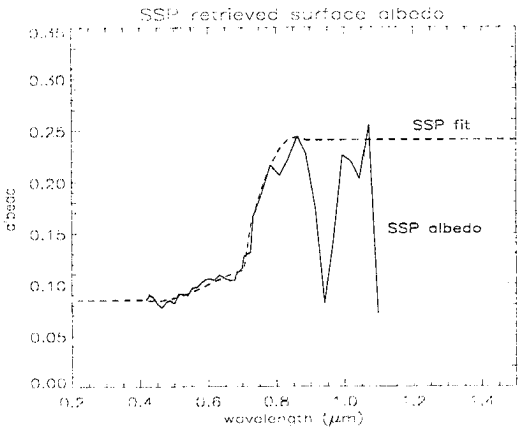

Figure 8.3: SSP retrieved ARESE surface albedo (solid) and the fit used in modeling simulations (dashed).

a contribution to surface absorption. The upwelling and downwelling total broadband fluxes at Egrett and Otter altitude are plotted in Fig. 8.4. The most important factor in the behavior of these clear sky fluxes is obviously the changing solar zenith angle. The second panel shows the normalized column net flux difference, interpreted loosely here to be column absorption. This is seen to vary between 5 and 20%. These values are reasonable as revealed by clear sky situations in the experiments of the previous chapter.

The shading indicated on Fig. 8.4 identifies the period for which simulations are performed by the MC/ET model. Only one simulation for each case was performed resulting from the time required to run the model. The flight track and aircraft altitudes for the time between 17.55 and 17.62 UTC are indicated in Fig. 8.5. The average solar zenith angle of 45.65 degrees was used along with the 17.5 UTC radiosonde which provided a profile of water vapor mixing ratio (top left panel of Fig. 8.6. The ozone profile was obtained from an ozone sonde launched at 15.5 UTC and CO_2 and O_2 mixing ratios were assumed constant at $5.013E^{-4}$ and .2314 g/g, respectively. A wide field of view (WFOV) camera image taken during this flight segment is shown in the top right panel of Fig. 8.6. Farm fields and rivers are evident in this photo taken from an altitude of 13.6 km. Clear skies are also indicated in the lower panel by the cloud detection lidar (CDL) which was flown on the Egrett. Here, laser reflection off the surface is the only returned signal.

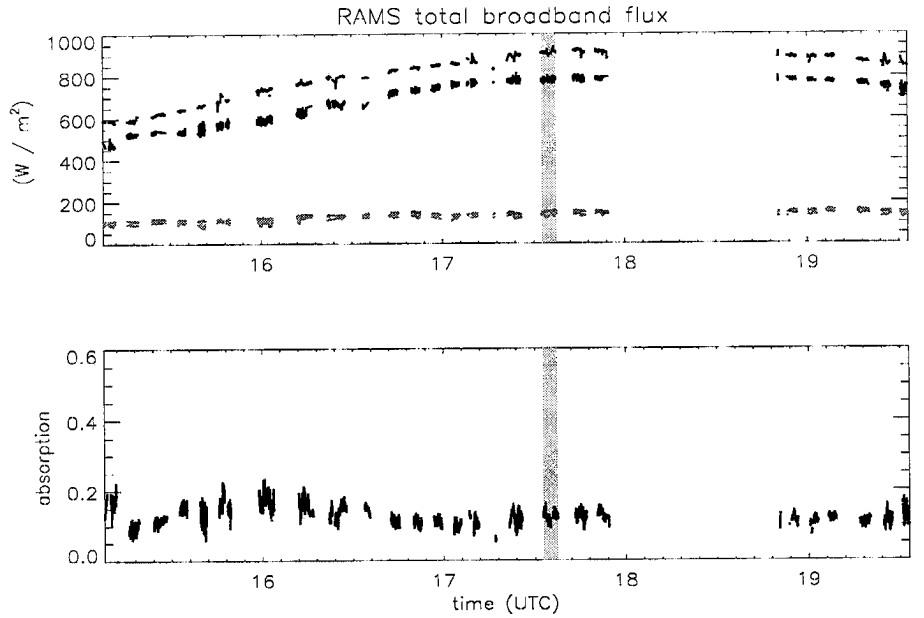

Figure 8.4: Downwelling Egrett and Otter total broadband flux (dark traces where the Otter measurement is lower) and upwelling Egrett and Otter total broadband flux (light traces) for the clear sky case of 11 October 1995. Model simulation was performed for the time period indicated by the shaded region.

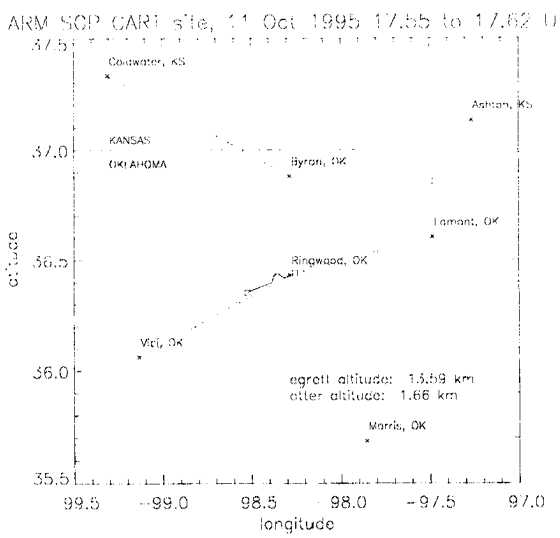

Figure 8.5: SGP CART site and aircraft flight strategies (dotted line). Flight track where measurements are used for comparison to model simulation is shown as a dark line between small squares.

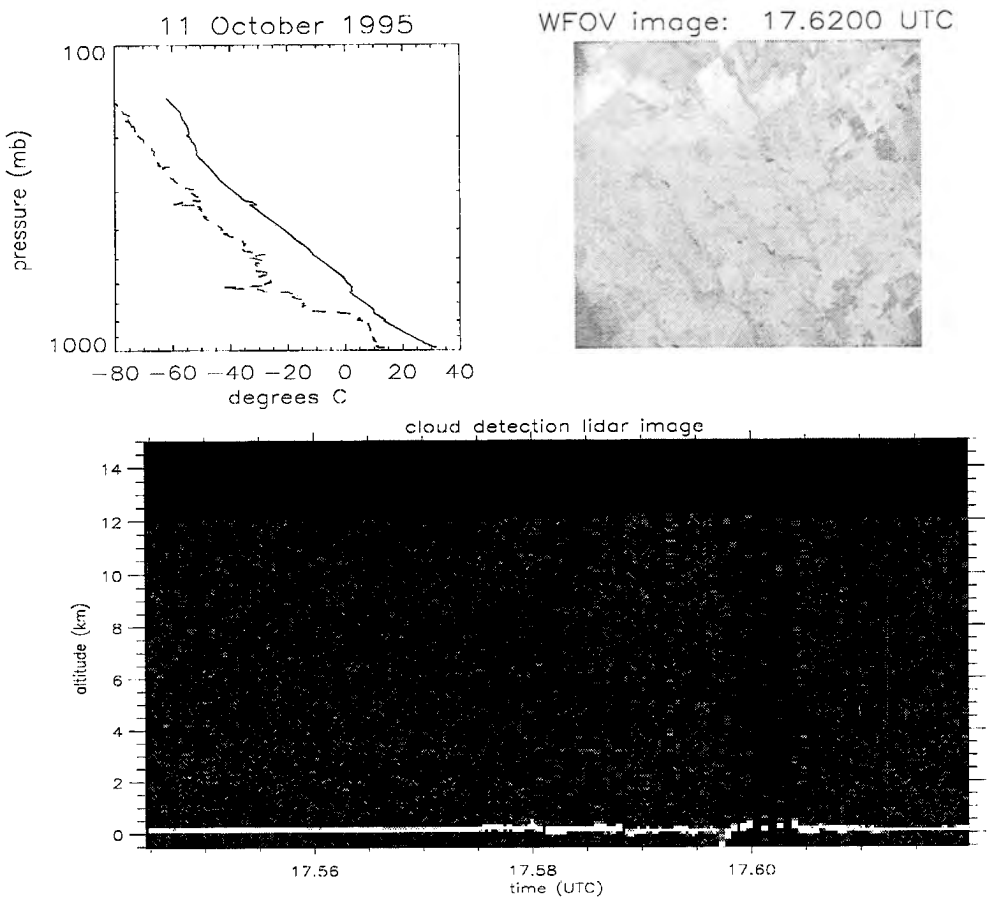

Figure 8.6: Upper left: 17.5 UTC sounding from the Central Facility in Lamont returned temperature (solid) and dew point (dashed) from which water vapor mixing ratio was determined. Upper right: WFOV image taken from the Egrett at an altitude of 13.6 km. Bottom: CDL image obtained during the flight leg between 17.55 and 17.62 UTC on 11 October 1995

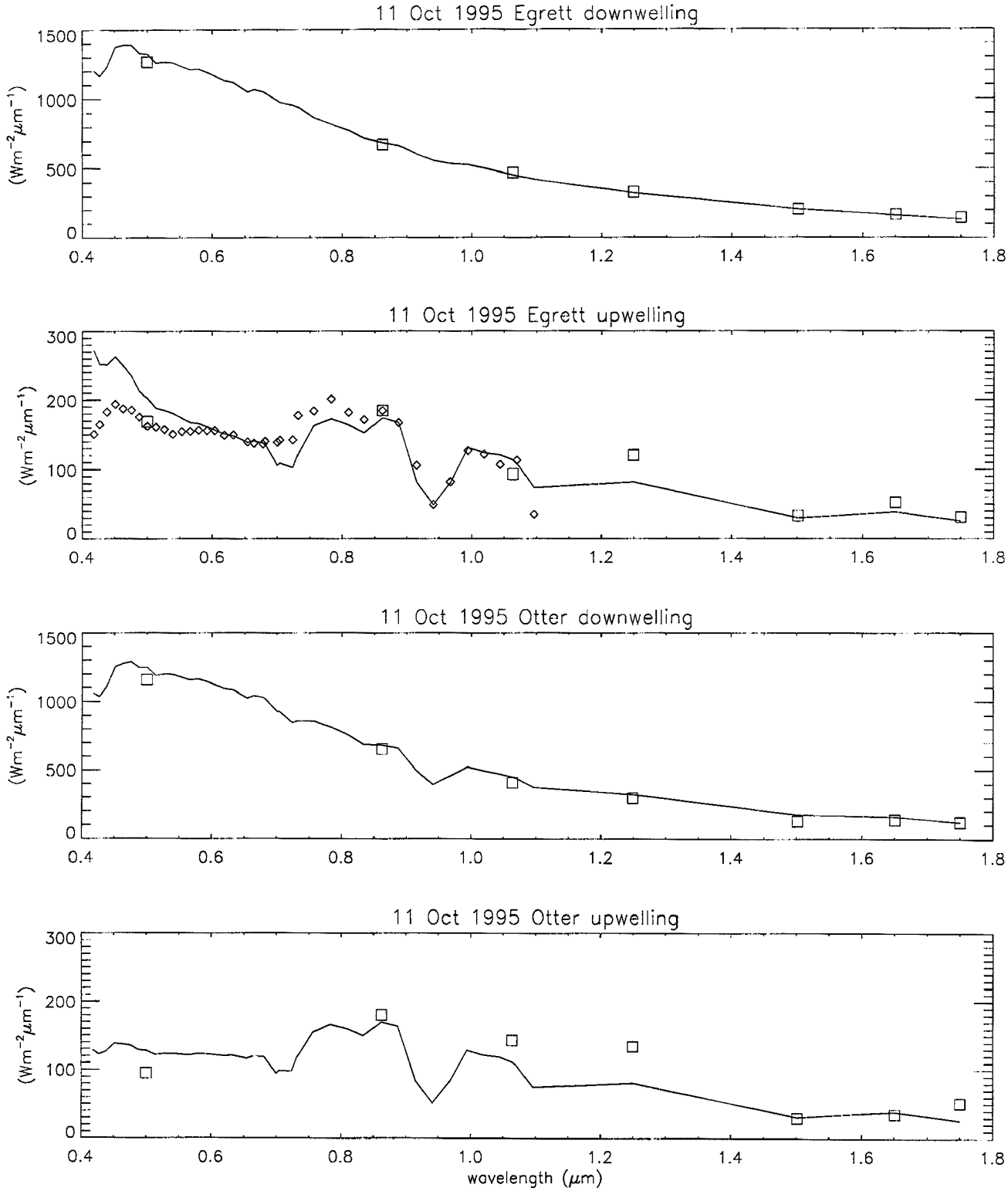

Figure 8.7: Above cloud (Egrett) and below cloud (Otter) spectral flux as simulated by MC/ET (solid line), observed by TDDR (squares), and observed by SSP (diamonds)

The downwelling and upwelling spectral flux measured by the Egrett at 13.6 km and the Otter at 1.7 km are plotted with the model simulated spectral flux at each level in Fig. 8.7. Model flux degraded to SSP and TDDR resolution for comparison, is indicated by the solid line. SSP and TDDR measurements are plotted as diamonds and squares, respectively. Egrett and Otter TDDR downwelling flux (panels 1 and 3) are well simulated by the model. The model overestimates downwelling 0.5 and 0.862 μm flux at Egrett altitude and most Otter downwelling TDDR measurements by about 50 $Wm^{-2}\mu m^{-1}$. Introduction of stratospheric aerosol into the model may bring downwelling fluxes below 0.9 μm into closer agreement. Except for SSP measurements between 0.4 and 0.5 μm, upwelling flux differences are no larger than those for downwelling flux (panels 2 and 4, note change in y-axis scale). The behavior of the difference between model and measurements from 0.4 to 0.85 μm is not captured particularly well by the model. This difference may indicate that the albedo retrieved east of Lamont, OK has different spectral properties than the albedo of other areas such as this one west of Ringwood, OK. It is also possible that tropospheric aerosol between the Egrett and Otter not included in the model simulation will have an effect on upwelling fluxes, especially at shorter wavelengths.

Broadband albedo and absorption for model and observation during this segment of flight track is listed in Table 8.1. The observed broadband quantities were obtained from the RAMS pyranometers. The down-looking FSBR instrument on the Egrett was not operational on this day so separation of the observed total shortwave spectrum into VIS and NIR regions is not possible. Differences in albedo are 0.63% and absorption are 2.76%. Clearly, the NIR region of the model accounts for almost all of the absorbed solar radiation. Only 1.25% of the radiation in the VIS region is absorbed by small amounts of ozone in the troposphere.

8.3.2 30 October 1995

Overcast sky conditions were observed on 30 October 1995. Broadband flux measurements for the entire flight are plotted in the top panel of Fig. 8.8. The Egrett upwelling flux measurement (light trace near 400 $Wm^{-2}\mu m^{-1}$ indicates a relatively uniform cloud

Table 8.1: 11 October 1995 model vs. observation column albedo and absorption.

spectral range	albedo (%)		absorption (%)	
	model	observation	model	observation
total	16.89	16.26	9.95	12.71
VIS	17.98	N/A	1.25	N/A
NIR	16.00	N/A	17.05	N/A

deck. Downwelling Otter flux (dark trace which begins near 100 $Wm^{-2}\mu m^{-1}$) shows much more variability. Because the Otter is flying just below cloud base, the effects of cloud heterogeneity on the downwelling flux are evident. The absorption calculated by net flux differencing is shown in the lower panel of Fig. 8.8. Absorption is near 40% when the cloud is thick and uniform (where Otter downwelling is low and constant) and reaches 10% where cloud edge effects as indicated by peaks in Otter downwelling flux are important. Holes or thin spots in the cloud funnel radiation, causing the downwelling flux to be high and the calculated absorption to be low. The region chosen for model simulation is shown by the shading in Fig. 8.8. This region between 17.65 and 17.9 UTC was chosen because the downwelling Otter and upwelling Egrett measurements indicate that the cloud is thickest and most uniform here. As noted in Chapter 1, sampling issues usually require fluxes to be averaged over large distances to converge. This is necessary because over short distances, cloud heterogeneity can cause large excursions from the true average flux and cause apparent positive or negative absorption. Valero et al. (1997) use the 0.5 μm TDDR measurement to assess the presence of apparent absorption. Because there should be very little absorption at this wavelength, all calculated absorption will be the result of cloud geometry effects. The mean absorption during this flight leg calculated from the 0.5 μm TDDR measurement is 6.9%. This is close to the 5% published by Valero et al. (1997) in which it is stated that convergence to this value indicates that sampling errors have been eliminated. The flight track corresponding to this time period is plotted in Fig. 8.9.

Because no cloud microphysical data were obtained for clouds between the Egrett and Otter aircraft during ARESE, direct simulation of fluxes using an observed cloud is

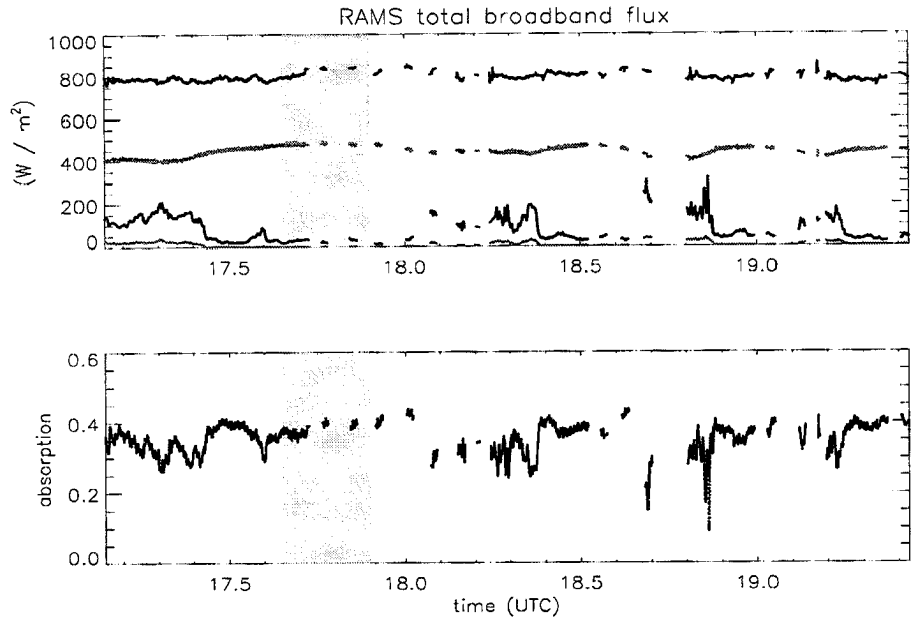

Figure 8.8: Downwelling Egrett and Otter total broadband flux (dark traces where the Otter measurement is lower) and upwelling Egrett and Otter total broadband flux (light traces where the Otter measurement is lower) for the overcast case of 30 October 1995. Model simulation was performed for the time period indicated by the shaded region.

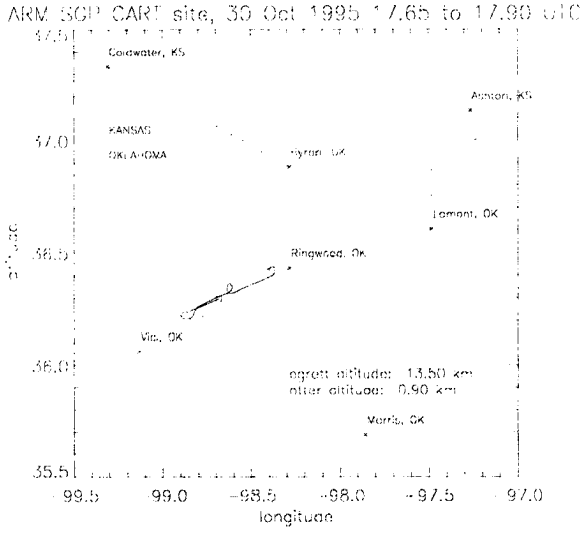

Figure 8.9: SGP CART site and aircraft flight strategies (dotted line). Flight track where measurements are used for comparison to model simulation is shown as a dark line between small squares.

not possible. Only cloud top and base information is used. Cloud base is inferred to be 1 km from the sounding plotted in the top left panel of Fig. 8.10 and Otter altitude (the Otter flew below cloud base at 0.898 km). A cloud top of 2 km was obtained from the CDL data plotted in the bottom panel. The CDL image also indicates the presence of a broken thin cirrus layer near 11 km. At the time of this study, the MC/ET model could not accept more than one cloud scattering phase function. This is the primary reason for neglecting the cirrus cloud. It is also obvious that the cirrus layer is optically thin because there is no noticeable attenuation of the lidar signal. It is speculated that the inclusion of this layer of cirrus in the model would affect the NIR portion of the spectrum due to differences in the ice particle phase function. It is most probable that reflection off the ice cloud would increase upwelling spectral flux slightly at these wavelengths. Valero et al. (1997) do not mention the existence of this cirrus layer in their analysis of 30 October aircraft fluxes and, apparently, also neglect it. The WFOV image of the unbroken cloud deck is displayed in the top right panel of Fig. 8.10. The average solar zenith angle of 50.62 degrees was used in the model simulation.

Model cloud optical depth was adjusted to best reproduce the observed TDDR 0.5 μm upwelling flux above cloud and downwelling flux below cloud. The optical depth in the VIS region was about 74, or almost twice that of the ScI cloud used in Chapter 7. These measurements show little sign of anomalous absorption for the entire flight as seen in Valero et al. (1997). The simulated Egrett downwelling and upwelling and Otter downwelling and upwelling spectral fluxes are plotted in Fig. 8.11. The SSP (diamonds) and TDDR (square) measurements are overlayed. The first detail to be pointed out is that the modeled upwelling and downwelling flux can not match the corresponding 0.5 μm measurements. In both cases, the model is too high. Though making the model cloud thicker will cause the downwelling flux to match, the difference in upwelling flux will get worse. Making the cloud thinner will have the opposite effect resulting in a worse agreement in downwelling flux. Following the argument of Zender et al. (1997), this bias will result in some unexplained absorption. Nevertheless, agreement between model and TDDR is good. SSP measurements fall on the model upwelling flux between

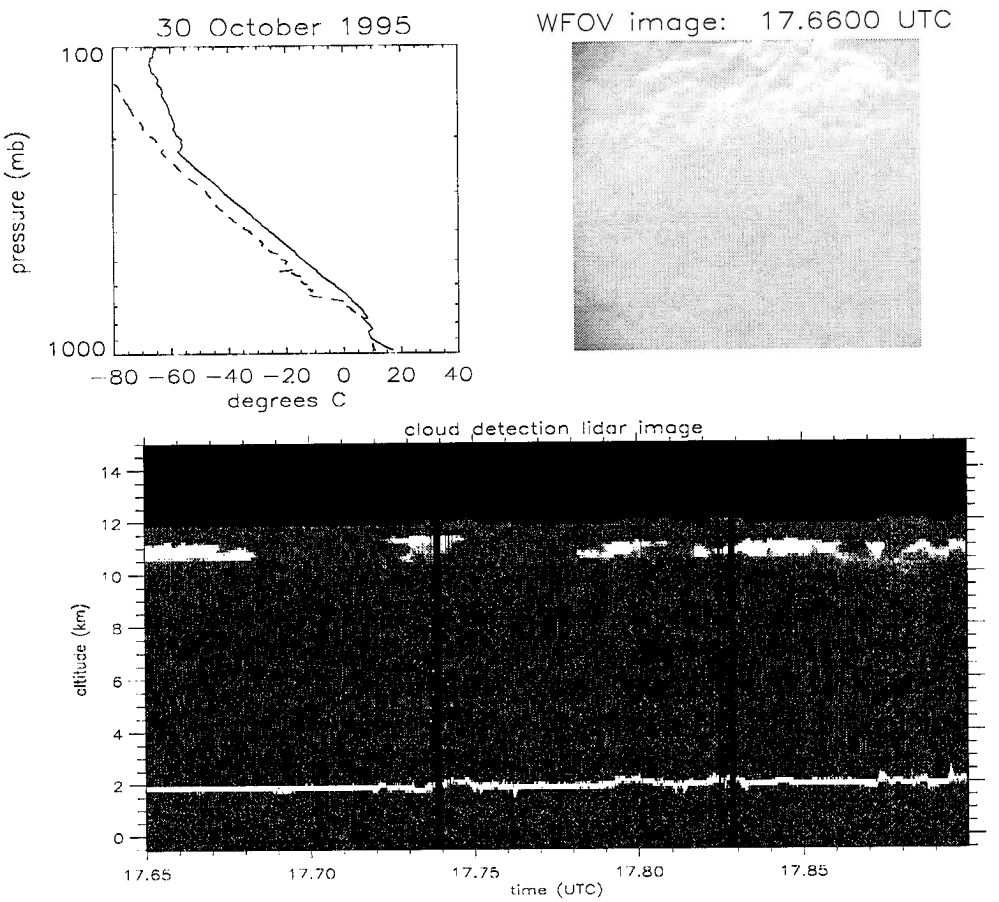

Figure 8.10: Upper left: 17.5 UTC sounding from the Central Facility in Lamont returned temperature (solid) and dew point (dashed) from which water vapor mixing ratio was determined. Upper right: WFOV image taken from the Egrett at an altitude of 13.5 km. Bottom: CDL image obtained during the flight leg between 17.65 and 17.9 UTC on 30 October 1995

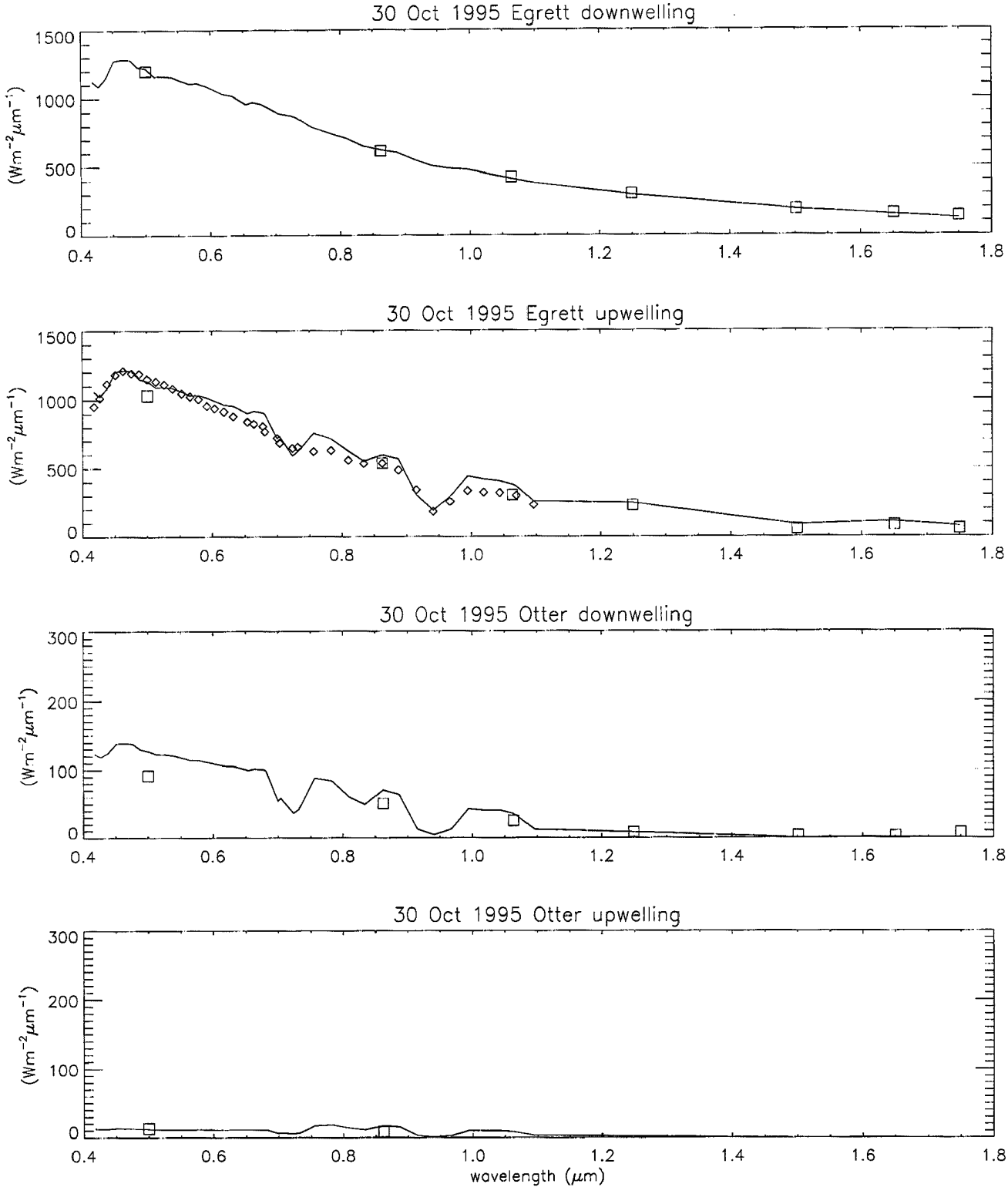

Figure 8.11: Above cloud (Egrett) and below cloud (Otter) spectral flux as simulated by MC/ET (solid line), observed by TDDR (squares), and observed by SSP (diamonds)

0.4 and 0.5 μm and between 0.875 and 0.95 μm. However, it appears that the SSP does not capture some wavelength to wavelength change in absorption features in the other regions. This may be due to differences between the ScI and true wavelength dependent phase function and optical depth or the presence of the thin cirrus layer. Except for these small differences, the SSP shows no evidence of the presence of major absorption that is not accounted for by theory.

Broadband albedo and absorption for model and observation as measured by the RAMS instruments during this segment of flight track is listed in Table 8.2. The differences in albedo are large: 10.9% for the total shortwave, 10.93% for VIS, and 8.17% for NIR. The differences in the modeled and observed absorptions are astounding. Observed absorption is higher than theory by 18.52% total, 22.3% for VIS, and 12.49% for NIR. These differences are not expected from the spectral flux analysis.

Table 8.2: 30 October 1995 model vs. observation column albedo and absorption.

spectral range	albedo (%)		absorption (%)	
	model	observation	model	observation
total	69.59	58.69	19.77	38.29
VIS	83.38	72.45	1.17	23.47
NIR	58.17	50.00	35.16	47.65

8.4 A Consistency Analysis and a Probable Discrepancy Source

The first part of this study investigated the effects of cloud heterogeneity on cloud and gas absorption. It was shown that this effect cannot change modeled atmospheric absorption to the magnitude of that measured by the broadband instruments during ARESE presented above. However, before another aspect of theory is investigated, a consistency check between the instruments flown on the aircraft needs to be performed.

The use of spectral instruments along side broadband instruments provides discrete points which relay information about the nature of the observed spectrum. However, without high resolution spectral observations, theory is relied upon to fill in the gaps. This is not ideal when a discrepancy between theory and observations is to be resolved.

Although upwelling SSP measurements provide necessary resolution, they do not cover the entire spectrum. Therefore, a consistency analysis was restricted to using the available data.

The upwelling SSP measurements on 30 October 1995 show good agreement with theory in terms of the non-existence of unaccounted for absorption regions. The only possibility lies in the presence of very small, very deep absorption lines between measurements. This probability and the probability that none of the SSP measurements would have overlapped one of these lines is extremely small. Therefore, it is concluded that if anomalous absorption exists, it is either outside the spectral region measured by the SSP or a phenomenon that affects all wavelengths to the same degree.

To test the first hypothesis, it was assumed that the 0.5 μm TDDR measurements were correct and that all radiation outside of the SSP wavelengths was attenuated in the atmospheric column between the Egrett and Otter. In addition to being a very conservative assumption, the non-existence of solar radiation outside the SSP wavelengths is impossible in nature as indicated by TDDR measurements beyond 1.25 μm. Yet, these TDDR measurements were neglected because there is a possibility that an absorber unexplained by theory exists in the spectral regions between them. Because some spectral features like the oxygen-A absorption band are poorly resolved by the SSP, the high resolution model spectral flux was used and scaled to match the 0.5 μm TDDR measurements. This scaling is theoretically validated for upwelling flux above cloud by the flux ratio investigation performed in the previous Chapter. That showed that if the measurement at one wavelength changes, the entire spectrum should change by the same relative amount. It is assumed that this same principal holds for the other three fluxes measured by the aircraft. The resulting spectral fluxes that were integrated for use in net flux differencing are shown in Fig. 8.12. According to the shape of the resulting spectra, the assumptions explained above are extremely conservative.

The absorptions that result from this experiment are listed in Table 8.3. Although albedo is underestimated and absorption is overestimated, it is not by much. Thus, the flux observed by the RAMS instruments must have spectra close to those used in this

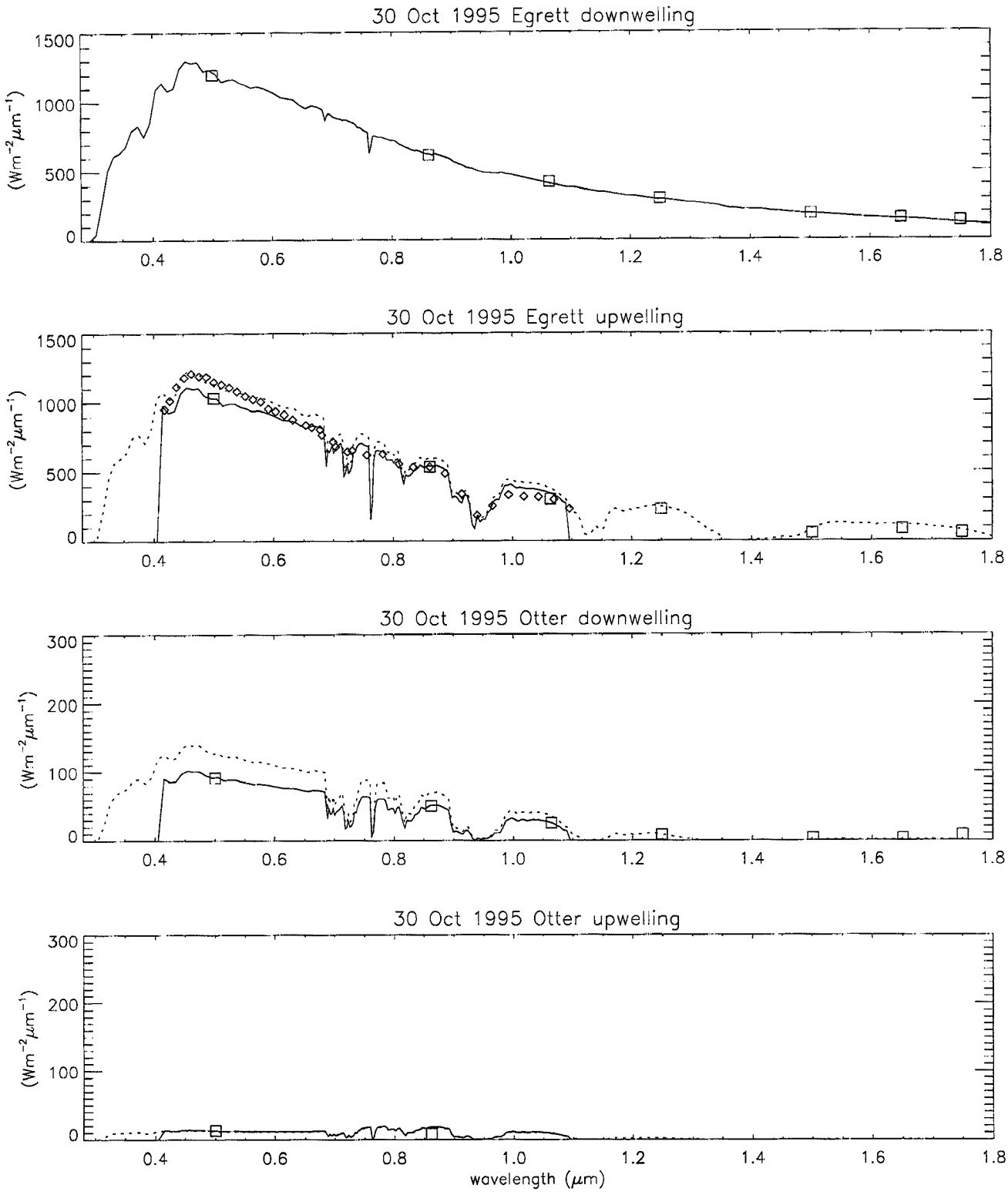

Figure 8.12: Original simulated fluxes for 30 October 1995 (dotted line), TDDR measurements (squares), and SSP measurements (diamonds). The spectra used in the conservative assumption simulation are plotted as solid lines.

experiment. The most striking example is in the VIS region of the spectrum where the absorption difference is only 3.2%. If the RAMS measurements are correct, all radiation at wavelengths less than 0.4 μm must be absorbed between the Egrett and Otter when the sky is overcast.

Table 8.3: Albedo and absorption results assuming 0.5 μm TDDR and SSP variation are correct and all radiation outside of SSP wavelengths is absorbed.

spectral range	albedo (%)		absorption (%)	
	experiment	observation	experiment	observation
total	52.67	58.69	43.90	38.29
VIS	68.12	72.45	26.67	23.47
NIR	41.39	50.00	56.48	47.65

To test the hypothesis that anomalous absorption affects all wavelengths equally, the model spectral fluxes were adjusted in a relative sense until their integration matched each broadband measurement from RAMS within 1 Wm^{-2}. This required multiplying the simulated Egrett downwelling spectral flux in Fig. 8.11 by 0.973, the Egrett upwelling flux by 0.748, the Otter downwelling flux by 0.41, and the Otter upwelling flux by 0.0. The resulting spectral fluxes that are required to reproduce the RAMS measurements are shown in Fig. 8.13. Clearly, if the RAMS instrument is accurate, the SSP and TDDR instruments as well as absorption theory must be incorrect.

8.5 30 October Absorption Inferred by TDDR, SSP, and Theory

Using the assumption that the absolute magnitude of the TDDR spectral observations, the non-existence of anomalous absorption between 0.4 and 1.1 μm as inferred from the SSP measurements, and the model gaseous absorption parameterization are correct, the broadband absorption for the entire flight on 30 October has been calculated. This simply involved matching the 0.5 μm model results with the 0.5 μm TDDR measurements and relatively adjusting the rest of the model spectrum in the same manner as the first experiment above. Integration of each adjusted model spectrum resulted in estimates of

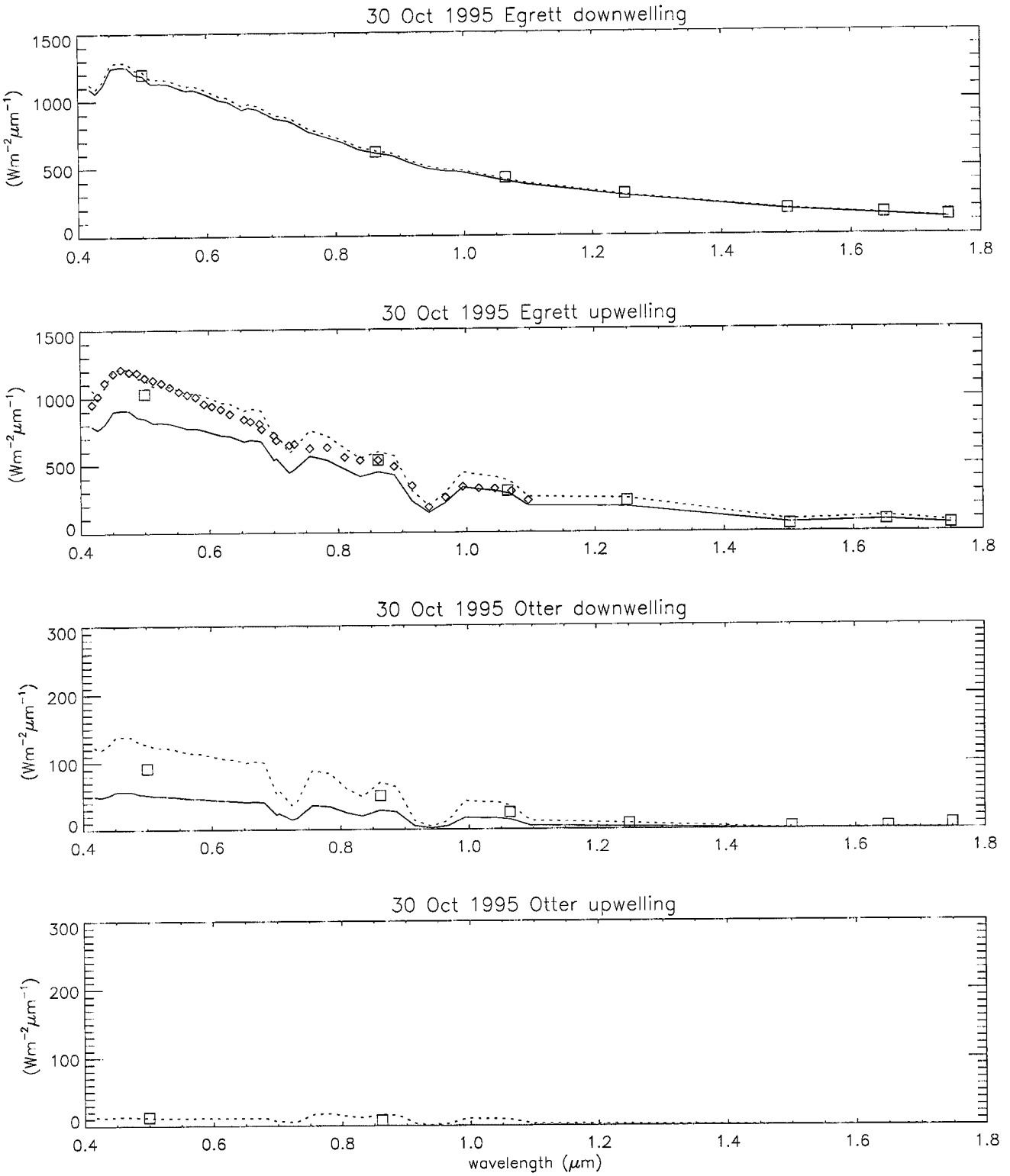

Figure 8.13: Original simulated fluxes for 30 October 1995 (dotted line), TDDR measurements (squares), and SSP measurements (diamonds). The spectra derived to match broadband RAMS measurements are plotted as solid lines.

the broadband flux. This was done for all TDDR measurements from 17 to 19.8 UTC and the mean absorption was calculated using the net flux differencing technique.

The absorption calculated from the RAMS instrument on 30 October reported by Valero et al. (1997) is near 36%. Absorption calculated for this day using the TDDR, SSP, and model as described above is 25.04%. This is in closer agreement to the model result of 19.77% for the flight leg between 17.65 and 17.9 UTC used in this study. Because the theoretical absorption should not change much due to cloud heterogeneity effects and neglecting changes in the profiles of absorbing gases, it is expected that the absorption that would be calculated by the model will remain around 20%. Hence, in this calculation of atmospheric absorption, the discrepancy between model and observation is reduced from 16% to 5%. If the Ackerman and Cox (1982) correction method is used and it is assumed that absorption in the visible portion of the spectrum is negligible, then the broadband absorption calculated with the TDDR, SSP, and model data decreases approximately to the expected model value of 20%.

8.6 Summary

In this Chapter, comparisons between theory and observations were presented for the clear sky case of 11 October 1995 and the overcast case of 30 October 1995 during the ARESE IOP. Model inputs included the SSP retrieved surface albedo, radiosonde data which provided water vapor and ozone amounts, and average solar zenith angles for short flight segments. It was shown for the clear sky case that total broadband albedo and absorption agreed within 0.7% and 3%, respectively. Spectral upwelling fluxes obtained by the TDDR and SSP radiometers differed in behavior from those output from the model in the VIS and short end of the NIR region. These differences are most likely due to variation in surface albedo between that used in the model and that observed along the section of flight track used. Aerosol effects may also have played a role.

Broadband comparisons between theory and observations were not as favorable. Because no cloud morphology or microphysical data was available for this case, a plane-parallel cloud was used in the MC/ET model and its optical thickness was adjusted until

above cloud upwelling and downwelling below cloud 0.5 μm simulated and observed spectral flux were as close as possible. This was justified by the experiments in Chapter 7 which indicated that the plane-parallel assumption does not bias absorption in mostly cloudy situations. Although TDDR and SSP measurements were in relatively good agreement with the model, the broadband absorptions differed by as much as 22%.

The agreement with TDDR and SSP and the disagreement with RAMS indicates the possible existence of instrument differences. The instrument discrepancy was highlighted in terms of two experiments. The first assumed that the TDDR and SSP measurements were correct and that the anomalous absorption must appear in regions where these instruments did not make measurements. Hence, all solar radiation below 0.4 μm and above 1.1 μm was assumed to have been absorbed between the Egrett and Otter. This brought the broadband absorptions into good agreement. This results casts uncertainty on the accuracy of the RAMS instruments in cloudy conditions. Second, it was assumed that the RAMS instruments were correct and the model spectra were adjusted to match the broadband observations. This clearly indicated that this assumption means all TDDR and SSP spectral flux channels are incorrect as well as theoretical absorption theory.

By assuming that the TDDR, SSP, and model results were accurate, the absorption for the entire overcast day was recalculated. The total shortwave absorption using these data is 25% versus the 36% indicated by RAMS.

Although undeniable proof has not been achieved with this study, results from Li et al. (to be submitted) also suggest that there may be a calibration problem with RAMS. By using the slope of albedo versus transmission β, it is shown that regressions using GOES-7 and ScaRaB satellite data over the SGP CART site results in a slope near 0.8 which is in good agreement with model values quoted by Cess et al. (1995). The SSP observations lie close to this regression line. However, the RAMS instruments and GOES-8 satellite produce regressions with a slope that is significantly smaller. The explanation given is that GOES-8 data suffer from incorrect calibration.

Chapter 9

SUMMARY AND CONCLUSIONS

The importance of the absorption of shortwave solar radiation to atmospheric processes has been well defined by many studies. Therefore, the discrepancy between simulated and observed atmospheric absorption is an issue for which a resolution is eagerly awaited by the scientific community. Motivated by the recent escalation of the debate about the existence of excess atmospheric absorption in the presence of clouds, the main objective of this study was to assess the role cloud heterogeneity plays in changing cloud and gas absorption. Because most simulated results are obtained from radiative transfer models which employ the plane-parallel approximation, the largest theoretical uncertainty was the implication of assuming a complex cloud system could be approximated as horizontally homogeneous. In order to investigate this, a Monte Carlo model was developed which could simulate broadband and spectral flux in an atmosphere consisting of a heterogeneous cloud field and variable gas profiles. This in itself is a major advancement in the utility of the Monte Carlo method. After the model was constructed, experiments were performed to provide insight into the effect of cloud heterogeneity on atmospheric radiative fluxes, albedo, and absorption. Once this was completed, simulations of two ARESE cases were compared to observations to try and determine the nature of the discrepancy. The following sections provide summaries of and conclusions from each step in the above process. The final section discusses suggestions for future research.

9.1 Model Development

The Monte Carlo method is ideal for investigating the interaction of solar radiation with a heterogeneous cloud field. This results from its straightforward procedure of tracing

photon paths through the atmosphere. However, to this point Monte Carlo models were limited to broadband calculations which provided no spectral information or spectral calculations that only included very small portions of the spectrum. For studies that compare model results to observations, Hignett and Taylor (1996) state "greater spectral resolution in the broad-band Monte Carlo model will be necessary to compare with better spectrally resolved observations." The Monte Carlo model developed for the present research enabled broadband calculations with a theoretically unlimited spectral resolution for gas, cloud, and surface absorption. This was accomplished by modifying the Equivalence Theorem as introduced by Irvine (1964) to account for cloud heterogeneity and vertically variable gas profiles as well as deriving similar relationships which could account for cloud and surface absorption. By running the Monte Carlo model once, the probability density functions which described the photon path lengths and number of cloud and surface scatters were used to calculate high resolution fluxes assuming the scattering properties of the atmosphere remained constant over that interval. As a result of computer memory limitations, the full three-dimensional pdf that is required by the derived relationships could not be used. Instead, the assumption that photon path lengths were independent of cloud and surface scattering was invoked. This led to maximum spectral flux errors near 50 $Wm^{-2}\mu m^{-1}$ in bands where gas, surface, and cloud absorption are important.

For accuracy it was noted that the scattering properties of clouds and air molecules are not constant across the entire shortwave solar spectrum. To account for this variability, it was shown that Monte Carlo calculations at five different wavelengths or nodes in the spectrum were sufficient for this study. The locations of these nodes were primarily determined by the wavelength dependent Rayleigh scattering properties of air molecules. When compared to the 32-stream adding-doubling model run at full resolution, the Monte Carlo/Equivalence Theorem (MC/ET) model broadband errors were within 1.2% and spectral errors were no worse than those presented above.

9.2 The Effect of Cloud Heterogeneity on Flux, Absorption, and Albedo

By using the MC/ET model, the effects of cloud spatial distribution and internal heterogeneity were investigated for a ScI cloud (Stephens, 1979) between the altitudes of 1 and 2 km. Spatial distribution was studied in the form of cloud fraction when cuboidal clouds were "grown" from 0 to 4 km in width. At this point the cloud field became plane-parallel. Results from each model run were compared to results obtained when the equivalent plane-parallel cloud was used. For the parameters involved, it was shown that the plane-parallel approximation overestimates total absorption for cloud fractions less than 0.7 by as much as 3% because cloud and gas absorption is too large. The heterogeneous cloud results in a slightly higher absorption for cloud fractions above 0.7 because breaks in the cloud promote more gas absorption than the horizontally homogeneous cloud. Atmospheric albedo and radiative fluxes are significantly affected by cloud heterogeneity. The difference between broken and plane-parallel cloud fields is as much as 20%. The albedo and flux ratios were introduced to eliminate the effects of cloud thickness and morphology and show that spectral flux can be scaled to match VIS observations without invalidating the simulated flux at other wavelengths.

The effect of internal heterogeneity was investigated for a fractal cloud field. For a ScI cloud, the degree of internal heterogeneity simulated had a small effect on fluxes and an even smaller effect on absorption. However, the relative changes in gas and cloud absorption were consistent with the cloud fraction experiment. Similarly, Landsat data were used to simulate a cloud field which included both spatial and internal heterogeneity. The differences between plane-parallel and heterogeneous atmospheric absorption were larger for this case, primarily due to the effect of spatial distribution.

For clouds of this geometric and optical thickness located near the surface, cloud heterogeneity was shown to have a negligible effect on changing total absorption or lead to less absorption than simulations run with an equivalent plane-parallel cloud. These results were interpreted in terms of photon path length and cloud scattering differences. The most important conclusion from this section is that observations of absorption in

excess of model predictions by more than a few percent cannot be explained by the effects of heterogeneity.

9.3 ARESE Comparisons

In order to investigate the absorption discrepancies published by Valero et al. (1997) and Zender et al. (1997), two case studies were chosen from the ARESE IOP for comparison: clear sky (11 October 1995) and overcast (30 October 1995). For the clear sky day, the spectral and broadband fluxes measured by the aircraft compared favorably to model simulation results. The behavior of the simulated VIS region spectral fluxes was different from those that were observed, possibly due to differences in modeled and actual surface albedo. For this day, the difference in total absorption was 2%.

Simulation of the overcast case was more difficult because cloud macrophysical and microphysical observations were not made. Instead, cloud optical depth was adjusted until simulated fluxes were as close as possible to observed upwelling and downwelling spectral flux above and below the cloud. This was performed using a plane-parallel cloud field, the use of which was justified by the knowledge that heterogeneity would not bias absorption calculations. Therefore, any discrepancy would be due to other factors. Although the simulated fluxes were in relatively good agreement with the spectral observations of the TDDR and SSP instruments, the broadband fluxes, and therefore absorptions, were very different than those obtained by the RAMS instrument. The model underestimated total shortwave absorption by 18.52% and VIS absorption by 22.3%. Barring a serious gap in absorption theory, these differences are larger than any operational or theoretical error discussed in chapter 2 can explain.

Because observed and simulated spectral measurements were in good agreement, it was speculated that the large absorption difference might be due to instrument error. Consistency checks were performed to test this hypothesis. First, it was assumed that the TDDR and SSP results were correct and that no anomalous absorption was present within the SSP wavelengths. It was shown that all radiation outside of the SSP wavelengths must be absorbed in the atmospheric column between the Egrett and Otter aircraft in order

to match the results from RAMS. For the second experiment, it was assumed that the RAMS results were correct. When modeled spectral flux was adjusted until the simulated broadband fluxes matched those from the RAMS instrument, it was shown that in this case the TDDR, SSP, and model results must all be incorrect. It is probable that the largest source of the absorption discrepancy reported from the ARESE IOP are the RAMS measurements and not an unknown atmospheric absorption process. This result is similar to one seen in Li et al. (to be submitted) in which comparisons of RAMS to ScaRaB and GOES satellite data are presented. When the TDDR, SSP, and model were used in the present study to obtain broadband fluxes for the entire flight on 30 October 1995, the total absorption difference between model and observation is reduced from 16% to 5%.

9.4 Suggestions for Future Research

Although this study has not shown that the entire absorption discrepancy observed during ARESE is due to instrument error, it has highlighted the importance of accurate observations. It is very likely that theoretical inaccuracies exist. However, before these inaccuracies can be investigated by comparing observational data to theoretical results, uncertainties involving observations must be addressed. To accomplish this, broadband and spectral measurements must be made simultaneously so that one can be explained in terms of the other. The TDDR and SSP measurements from ARESE represent the minimum information required to perform comparisons to the broadband RAMS instruments. Ideally, spectral measurements of upwelling and downwelling flux above and below cloud at SSP resolution for the entire shortwave spectrum is required to provide the most accurate spectral and broadband datasets for model comparison.

Once measurements are as accurate as possible, the quantity and quality of model inputs can be called into question through studies such as this one. Even though plane-parallel model results were accurate enough to show that theoretical absorption for the overcast ARESE case was near 20%, more information about the morphology and microphysics of observed cloud fields are required to decrease model error. This is especially true for cloud fractions less than 0.7%. The MC/ET model is ideal for studies of this

nature. For this method, the resolution of cloud field geometry as well as gas, cloud, and surface absorption is only limited by computer memory. Further improvements can be made to make the model even more representative of the real atmosphere. By converting the MC/ET model to use line-by-line gas absorption information instead of the present k-distribution method, assumptions about the transmission of radiation through gas are reduced. The inclusion of aerosol into the model is straightforward and similar to that described for cloud and Rayleigh optical depth integration. In the present model, Rayleigh optical depth and gas amount is assumed constant in discrete layers. However, the use of an analytic integration of the Rayleigh optical depth equation and the retainment of a continuous path length-layer pdf in the Monte Carlo model will enable continuous variability of Rayleigh scattering and gas absorption profiles in the model atmosphere. As noted by Hignett (1987), more computational effort leads to better agreement between simulations and observations in any particular case. Because the MC/ET method is theoretically exact, the utility of a line-by-line version of this model will be explored in future research for performing benchmark calculations under heterogeneous cloud conditions.

The tasks proposed are quite complex. The determination of observational and theoretical uncertainty bounds for all possible cloud conditions is impossible. However, an understanding of these bounds will be important to obtain before it can be proven that present solar radiative transfer theory has not left anything out.

REFERENCES

Ackerman, S. A. and S. K. Cox, 1981: Aircraft observations of shortwave fractional absorptance of non-homogeneous clouds. sl J. Appl. Meteorol., **20**, 1510–1515.

Ackerman, S. A. and G. L. Stephens, 1987: The absorption of solar radiation by cloud droplets: An application of anomalous diffraction theory. *J. Atmos. Sci.*, **44**, 1574–1588.

Arking, A., 1996: Absorption of solar energy in the atmosphere: Discrepancy between model and observations. *Science*, **273**, 779–782.

Byrne, R. N., R. C. J. Somerville and B. Subasilar, 1996: Broken-cloud enhancement of solar radiation absorption. *J. Atmos. Sci.*, **53**, 878–886.

Cess, R. D., M. H. Zhang, P. Minnis, L. Corsetti, E. G. Dutton, B. W. Forgan, D. P. Garber, W. L. Gates, J. J. Hack, E. F. Harrison, X. Jing, J. T. Kiehl, C. N. Long, J.-J. Morcrette, G. L. Potter, V. Ramanathan, B. Subasilar, C. H. Whitlock, D. F. Young, Y. Zhou, 1995: Absorption of solar radiation by clouds: Observations versus models. *Science*, **267**, 496–499.

Chandrasekhar, S. 1960: *Radiative Transfer*, Dover, New York.

Chou, M.D., 1990: Parameterizations for the absorption of solar radiation by O_2 and CO_2 with applications to climate studies. *J. Clim.*, **3**, 209–217.

Chou, M.D. and A. Arking, 1980: Computation of infrared fluxes in the water vapor bands. *J. Atmos. Sci.*, **37**, 855–867.

Chou, M.D. and A. Arking, 1981: An efficient method for computing the absorption of solar radiation by water vapor. *J. Atmos. Sci.*, **38**, 798–807.

Davies, R., 1978: The effect of finite geometry on the three-dimensional transfer of solar irradiance on clouds. *J. Atmos. Sci.*, **35**, 1712–1725.

Davis, J. M., S. K. Cox and T. B. McKee, 1979: Vertical and horizontal distributions of solar absorption in finite clouds. *Journal Atmos. Sci.*, **36**, 1976–1984.

Drummond, A. J. and J. R. Hickey, 1971: Large-scale reflection and absorption of solar radiation by clouds as influencing earth radiation budgets: new aircraft measurements. Pp. 267-276 in *Preprints Int. Conf. on Weather Modification, Canberra*, American Meteorological Society.

Foot, J. S., 1988: Some observations of the optical properties of clouds. I: Stratocumulus. *Q. J. R. Meteorol. Soc.*, **114**, 129–144.

Fu, Q. and K.N. Liou, 1992: On the correlated k-distribution method for radiative transfer in nonhomogeneous atmospheres. *Journal Atmos. Sci.*, **22**, 2139–2156.

Grassl, H., 1975: Albedo reduction and radiative heating of clouds by absorbing aerosol particles. *Contrib. Atmos. Phys.*, **48**, 199–210.

Harshvardhan and D. A. Randall, 1985: Comments on "the parameterization of radiation for numerical weather prediction and climate models". *Monthly Weath. Rev.*, **113**, 1832–1833.

Hasayaka, T., N. Kikuchi and M. Tanaka, 1995: Absorption of solar radiation by stratocumulus clouds: Aircraft measurements and theoretical calculations. *J. Appl. Meteorol.*, **34**, 1047–1055. Herman, G. F., 1977: Solar radiation in summertime arctic stratus clouds. *J. Atmos. Sci.*, **36**, 1423–1432.

Herman, G. F. and J. A. Curry, 1984: Observational and theoretical studies of solar radiation in arctic stratus clouds. *J. Climatol. Appl. Meteorol.*, **23**, 5–24.

Hignett, P., 1987: A study of the short-wave radiative properties of marine stratus: aircraft measurements and model comparisons. *Q. J. R. Meteorol. Soc.*, **113**, 1011–1024.

Hignett, P. and J. P. Taylor, 1996: The radiative properties of inhomogeneous boundary layer cloud: Observations. *Q. J. R. Meteorol. Soc.*, **122**, 1341–1364.

Irvine, W. M., 1964: The formation of absorption bands and the distribution of photon optical paths in a scattering atmosphere. *B. A. N.*, **17**, 266–279.

King, M. D., 1981: A method for determining the single scattering albedo of clouds through observation of the internal scattered radiation field. *J. Atmos. Sci.*, **38**, 2031-2044.

King, M. D., L. F. Radke and P. V. Hobbs, 1990: Determination of the spectral absorption of solar radiation by marine stratocumulus clouds from airborne measurements within clouds. *J. Atmos. Sci.*, **47**, 894–907.

Lacis, A. A. and J. E. Hansen, 1974: A parameterization for the absorption of solar radiation in the Earth's atmosphere. *J. Atmos. Sci.*, **31**, 118–133.

Lacis, A. A. and V. Oinas, 1991: A description of the correlated k distribution method for modeling nongray gaseous absorption, thermal emission, and multiple scattering in vertically inhomogeneous atmospheres. *J. Geophys. Res.*, **96**, 9027-9063.

Li, Z. and L. Moreau, 1996: Alteration of atmospheric solar absorption by clouds: Simulation and observation. *J. Appl. Meteorol.*, **35**, 653–670.

Li, Z., A. Trishchenko, H. W. Barker, G. L. Stephens, P. T. Partain and P. Minnis, 1998: Consistency analyses of ARESE measurements for studying cloud absorption. To be submitted to *J. Geophys. Res.*

Liou, K. N., 1992: *Radiation and Cloud Processes in the Atmosphere*, Oxford University Press, 487 pp.

Liou, K. N. and G. D. Whitman, 1979: Parameterization of the radiative properties of clouds. *J. Atmos. Sci.*, **36**, 1261–1273.

Marchuck, G. I., G. A. Mikhailov, M. A. Nazarailiev, R. A. Darbinjan, B. A. Kargin and B. S. Elepov, 1980: *The Monte Carlo Methods in Atmospheric Optics*, Springer-Verlag, 208 pp.

McClatchey, R. A., R. W. Fenn, J. E. A. Selby, F. E. Voltz and J. S. Garing, 1971: Optical properties of the atmosphere. *Environ. Res. Pap.*, No. 354, AFCRL.

McKee, T. B. and S. K. Cox, 1974: Scattering of visible radiation by finite clouds. *J. Atmos. Sci.*, **31**, 1885–1892.

Pilewski, P. and F. P. J. Valero, 1995: Direct observations of excess solar absorption by clouds. *Science*, **267**, 1626–1629.

Ramanathan, V., B. Subasilar, G. J. Zhang, W. Conant, R. D. Cess, J. T. Kiehl, H. Grassl and L. Shi, 1995: Warm pool heat budget and shortwave cloud forcing: A missing physics? *Science*, **267**, 499–503.

Rawlins, F., 1989: Aircraft measurements of the solar absorption by broken cloud fields: a case study. *Q. J. R. Meteorol. Soc.*, **115**, 365–382.

Reynolds, D. W., T. H. Vonder Haar and S. K. Cox, 1975: The effect of solar radiation absorption in the tropical atmosphere. *J. Appl. Meteorol.*, **14**, 433–444.

Slingo, A. and H. M. Schrecker, 1982: On the shortwave radiative properties of stratiform clouds. *Q. J. R. Meteorol. Soc.*, **108**, 407–426.

Slingo, A., S. Nicholls and J. Schmetz, 1982: Aircraft observations of marine stratocumulus during JASIN. *Q. J. R. Meteorol. Soc.*, **108**, 833–856.

Stephens, G. L., 1978a: Radiation profiles in extended water clouds. I: Theory. *J. Atmos. Sci.*, **35**, 2111–2122.

Stephens, G. L., 1988a: Radiative transfer through arbitrarily shaped optical media. Part I: A general method of solution. *J. Atmos. Sci.*, **45**, 1818–1836.

Stephens, G. L., 1979: Optical properties of eight water cloud types. *CSIRO Aust. Div. Atmos. Phys. Tech. Paper No. 36* , 35 pp.

Stephens, G. L. and T. J. Greenwald,1988: Application of a doubling-adding radiation model to visibility problems. *CIRA Tech. Paper*, 89 pp.

Stephens, G. L. and C. M. R. Platt, 1987: Aircraft observations of the radiative and microphysical properties of stratocumulus and cumulus cloud fields. *J. Climatol. Appl. Meteorol.*, **26**, 1243–1269.

Stephens, G. L. and S.-C. Tsay, 1990: On the cloud absorption anomally. *Q. J. R. Meteorol. Soc.*, **116**, 671–704.

Stephens, G. L., G. W. Paltridge and C. M. R. Platt, 1978: Radiation profiles in extended water clouds, III. Observations. *J. Atmos. Sci.*, **35**, 1837–1848.

Taylor, J. P., J. M. Edwards, M. D. Glew, P. Hignett and A. Slingo, 1996: Studies with a flexible new radiation code II: Comparisons with aircraft short-wave observations. *Q. J. R. Meteorol. Soc.,* **122**, 839–861.

Twomey, S., 1972: The effect of cloud scattering on the absorption of solar radiation by atmospheric dust. *J. Atmos. Sci.,* **29**, 1156–1159.

Twomey, S. and T. Cocks, 1982: Spectral reflectance of clouds in the near-infrared: comparison of measurements and calculations. *J. Meteorol. Soc. Japan*, **60**, 583–592.

Van de Hulst, H. C., 1980: chap. 17, *Multiple Light Scattering; Tables, Formulas, and Applications*, Academic Press.

Valero, F. P. J., R. D. Cess, M. Zhang, S. K. Pope, A. Bucholtz, B. Bush, and J. Vitko, Jr. , 1997: Absorption of solar radiation by the cloudy atmosphere: interpretations of colocated aircraft measurements. *J. Geophys. Res.,* **102**, 29,917–29,927.

Weinman, J. A. and Harshvardhan, 1982: Solar reflection from a regular array of horizontally finite clouds. *Appl. Optics*, **21**, 2940–2944.

Welch, R. M., S. K. Cox and J. M. Davis, 1980: Solar radiation and clouds. *Meteorol. Monogr.,* **39**, American Meteorological Society.

Wiscombe, W. J., R. M. Welch and W. D. Hall, 1984: The effects of very large drops on cloud absorption, Part I: parcel models. J. Atmos. Sci., **41**, 1336–1355.

Zender, C. S., B. Bush, S. K. Pope, A. Bucholtz, W. D. Collins, J. T. Kiehl, F. P. J. Valero and J. Vitko, Jr. , 1997: Atmospheric absorption during the Atmospheric Radiation Measurement (ARM) Enhanced Shortwave Experiment (ARESE). *J. Geophys. Res.,* **102**, 29,901–29,915.

Appendix A

FORMULATION OF THE TOTAL FLUX EQUATION FOR VARIOUS COMBINATIONS OF ATMOSPHERIC ABSORBERS

The power of the probability distribution $p(l,s,r)$ is the fact that the flux including gas, cloud, and surface absorption or any subset of these absorbers can be calculated. The following list explains how the pdf for each possible combination is created and how the corresponding flux is calculated.

- all absorbers:

$$p(l,s,r)$$

$$F_{tot} = F_o \cdot \int_0^\infty \left(\sum_{s=0}^{\infty} \left(\sum_{r=0}^{\infty} p(l,s,r) \alpha^r \omega_o^s e^{-l \sum_{n=1}^{N} p(l,n) k_n} \right) \right) dl \tag{A.1}$$

- gas + cloud absorption:

$$p(l,s) = \sum_{r=0}^{\infty} p(l,s,r)$$

$$F_{gas,cld} = F_o \cdot \int_0^\infty \left(\sum_{s=0}^{\infty} p(l,s) \omega_o^s e^{-l \sum_{n=1}^{N} p(l,n) k_n} \right) dl \tag{A.2}$$

- gas + surface absorption:

$$p(l,r) = \sum_{s=0}^{\infty} p(l,s,r)$$

$$F_{gas,surf} = F_o \cdot \int_0^\infty \left(\sum_{r=0}^{\infty} p(l,r) \alpha^r e^{-l \sum_{n=1}^{N} p(l,n) k_n} \right) dl \tag{A.3}$$

- cloud + surface absorption:

$$p(s,r) = \int_0^\infty p(l,s,r) dl$$

$$F_{cld,surf} = F_o \cdot \sum_{s=0}^{\infty} \left(\sum_{r=0}^{\infty} p(s,r) \alpha^r \omega_o^s \right) \tag{A.4}$$

- gas absorption:

$$p(l) = \sum_{s=0}^{\infty} \left(\sum_{r=0}^{\infty} p(l,s,r) \right)$$

$$F_{gas} = F_o \cdot \int_0^{\infty} p(l) e^{-l \sum_{n=1}^{N} p(l,n) k_n} dl \tag{A.5}$$

- cloud absorption:

$$p(s) = \int_0^{\infty} \left(\sum_{r=0}^{\infty} p(l,s,r) \right) dl$$

$$F_{cld} = F_o \cdot \sum_{s=0}^{\infty} p(s) \omega_o^s \tag{A.6}$$

- surface absorption:

$$p(r) = \int_0^{\infty} \left(\sum_{s=0}^{\infty} p(l,s,r) \right) dl$$

$$F_{surf} = F_o \cdot \sum_{r=0}^{\infty} p(r) \alpha^r \tag{A.7}$$

- no absorption: $F_{noabs} = F_o$

A multipurpose spectrally scanning polarimeter (SSP): Instrument description and sample results

Graeme L. Stephens, Robert McCoy, Renata McCoy, Philip Gabriel and Philip Partain

Colorado State University, Department of Atmospheric Science

Ft. Collins, CO 80523

Abstract

This paper descirbes

1. Introduction

The transfer of solar radiation in the Earth's atmosphere is important for a number of reasons. Differential absorption of solar radiation at the surface fuels the circulation of the oceans and absorption of solar radiation in the atmosphere is likewise an important source of energy for the large-scale circulation of the atmosphere. The variation of the fluxes of solar radiation are primarily affected by clouds and the detailed nature of the transfer of solar radiation in clouds has recently been called into question (e.g. Cess et al., 1995, Pilewskie and Valero, 1995, Valero et al., 1996). These studies are based on the interpretation of heterogenous data sets and debate about the validity of these interpretations lingers (e.g. Stephens, 1995; Barker et al., 1998 among several others). One reason this debate endures is that there is a general lack of high quality observations in and around clouds. This lack of data was one of the main motivations for the development of a spectrometer more than a decade ago by the present author (Stephens and Scott, 1984; Scott and Stephens, 1985). The instrument described in this paper, the scanning Spectral Polarimeter (SSP), is a third generation version of this earlier instrument.

This paper describes the design of the instrument, including the optical lay-out which is based on use of a circular variable filter to measure the spectral region from 400 nm through 4000 nm with Half Bandwidths (HBW) of l ess than 17 nm to 60 nm. The version of the SSP described

in this paper has six channels. four devoted to measurement of linear and circular polarization. one to spectral (unpolarized radiance) and another to spectral flux. The instrument characteristics are described. procedures to calibrate the instrument are discussed along with detailed error assessments of this calibration. Example measurements obtained from the instrument flown in experiments carried out by the U.S Departmant of Energy Unmanned Aerospace Vehichle (UAV) program (Ellingson and Vitko, 1998) are described.

2.Intrument Design and Characteristics

The instrument is designed in a modular fashion consisting of 3 main components – the motor drive assembly (A), a filter wheel and detector assembly (B), and the optics assembly (C) (refer to Fig. 1). The optical assembly is held in a vacuum to reduce the hazard of thermal shock and condensation problems. The modular feature of the instrument design offers a number of advantages, including the ability to use different optical assemblies (such as with or without polarization optics) or different filter arrangements. A more detailed discussion of each of these main components is now presented.

(a)The Optical Assembly

The version of the SSP described in this paper has six different optical channels as shown in Fig. 1. Radiation enters the instrument through one of 6 windows which are more clearly shown in Fig xx. After passing through the window. radiation is it is focused onto the Circular Variable Filter (CVF) wheel. then through the field stop. and onto the detector assembly. The field stop is designed to underfill the detectors. The polarization and achromatic focusing optics are held in an optical tower. which allows each of the optics to be individually positioned. Glan-Taylor polarization cubes are used in an effort to minimize the effects of thermal shocks to the optics.

The two circular polarization channels were not assembled in the instrument configured for the experiments reported in this paper. The optics of the linear polarization channels (channels 2 and 4) are defined by entering a fused silica window and a Glan-Taylor polarization cube so aligned to allow only perpendicular or parallel polarized light to pass. The latter is achieved by

rotating the Glan-Taylor polarizing cube 90°. Radiation then travels through a BK7 achromatic focusing lens, through a second fused silica window to exit the vacuum chamber, is focused on the CVF and then through the aperture and onto the detector.

The radiance channel (3) has a multi-spectral Zinc Sulfide (ZnS) window as the entrance port to the instrument. radiation then passes through a ZnS focusing lens at the bottom of the vacuum chamber and exits through a second ZnS window, focuses on the CVF, then through the aperture and onto a detector. Multi-spectral ZnS windows and lens are used for the path of this channel due to its flat transmission curve (approximately 70% transmission) from 400 nm - 9000 nm. The hemispheric flux channel (1) is similar to the radiance channel except that radiation enters through a flashed opal diffuser window. The entrance and exit windows are made of fused silica and the achromatic focusing lens is made of BK7.

The radiance and polarization channels (channels 2 to 6) all have narrow fields of view with a viewing half angle of approximately 20mRad. The diffuser in channel 1 provides a full hemispheric view.

(b)The Filter and Detector Assembly

The CVF vis a commercially available filter and is composed of four 90° section bandpass filters with a total bandpass of 400 nm - 4000 nm. Table 1 shows the nominal spectral region covered by each section of the wheel although only measurments in sections 1 and 2 are reported in this study. Variance between the nominal and actual wavelengths is as much at 15%, and variance between individual filters with the same nominal spectral range can be as much as 5% of the central wavelength.

The CVF sections are mounted on an aluminum wheel with a 0.040 inch space between each segment. The space provides a clear aperture for the broadband measurements. Index holes located on the outside rim of the aluminum wheel. as shown in Fig. ?, define the locations on the filter wheel where radiation data are read by the data acquisition system. Thes holes are a custom optical encoder and are placed at set intervals around this wheel defining the central wavelengths

of each data point. These wavelengths are listed in Table as a function of index hole number and position around the filter wheel. Bandwidths for each channel have not been measured. but are estimated at less than or equal to 4% of the central wavelength for sections 1 and 2. and less than 1.5% of the central wavelength for sections 3 and 4.

(c)Detectors

BOB to UPDATE

The detectors. shown in Fig. ?. are hybrid two color detectors with built in pre-amplifiers. A Silicon (Si) element is mounted over a Lead Selenide (PbSe) element. The Si element is used in the photovoltaic mode and the PbSe element is used inthe photoconductive mode. The detector windows are also made of multispectral zinc sulfide (ZnS). The Si detector has a spectral range of 400 nm to 1100 nm with an 8 nano-second response time. The Si element has a 50% transmission at wavelengths greater than 1100 nm. This allows radiation to pass through the element onto the PbSe detector below. The PbSe detector has a spectral range of 1000 nm to 5200 nm witha response time of 1-3 micro-seconds. The upper wavelength limit of the PbSe element is temperature dependent.

(d)Sensor Head Electronics and data aquisition

Bob fix up

Figure shows a block diagram of the SSP sensor head electronics. The circular variable filter is driven by a computer controlled stepper motor. The rotation rate can be varied from 0.1 revolution/second to 30 revolutions/second. Two optical switches are used, one to determine the start of a new scan and the second that generates data valid signals from the index holes on the rim of the CVF. Signals from each of the 2 color detectors (one for each channel) are amplified so the resulting analog signal sent to the data acquisition system varies from 0 volts/32500 counts (no signal) to -10 volts/0 counts (max signal). Temperature is monitored at four locations: the polarization and focusing optics, the CVF air chamber. the detector block, and the motor.

The SSP is designed to use two different data acquisition systems (DAS) to collect information from the sensor head. Both systems use a micro controller that runs all timing and data handling issues. Analog signals are received from the sensor head on 16 different channels. Descriptions of the 16 data channels are listed in Table. Each of the 16 data channels has its own sampling, 16 bit analog to digital converter. After the A-D conversion. digital data is put into two parallel first in first out (FIFO) outputs. Two FIFO ports are provided to allow two computer systems to read the same data from the SSP data acquisition system without rewiring. A real time clock is used to flag each data scan with the acquisition time.

The first DAS is rack mounted and was designed for manned airborne platforms, calibration, and ground testing. A block diagram of this system is shown in Fig. This system has full diagnostic outputs, real time graphical display. and large datastorage capacity.

The second DAS, a small footprint system, was designed for unmanned aerospace vehicles (UAV) or experiments where unattended operation is required. This system provides no graphical output, storage capacity, or input voltage. The user must provide the input voltage. download data from the FIFO ports, and transmit or store data from the sensor head. A block diagram of this system is shown in Figure. This small footprint version does provide diagnostic output for an external computer to aid in debugging.

3.Intrument Characteristics

3.1Field of View

TBD

The equipment setup used to determine the field of view for channels 2 - 4 is illustrated in Figure NFOVsetup. This experiment was conducted in a hallway where the distance between the SSP and the light source was 20 feet. The SSP was set on a leveling bench which consisted of a thick aluminum plate with a height adjusting screw in each corner. The light source is on scissors jack that allows the height of the bulb to be easily adjusted. The light source and jack are on a rolling bench with the wheels locked so the bench will only roll in a straight line. All equipment

is leveled and aligned down the center of the hallway using the Helium-Neon laser. A cardboard screen with a 5 by 7 inch hole was attached to the rolling table. This screen moves with the light source and stops most of the reflection from the walls. To reduce reflections further, two black felt curtains were hung across the hallway with a hole cut into each curtain to allow the light from the source to reach the SSP. A black felt curtain is also hung behind the SSP to reduce the reflection from the back wall. The source light is moved perpendicular to the experiment centerline as shown in Figure NFOVsetup. The distance from the center line and the signal intensity received at the SSP are recorded. The exact procedure used for this exercise is described further in Appendix B.

Results of measured intensity versus light source position for the radiance channel (3), are shown in Figures nfovch3r. This graph shows the relative power received (digital counts) versus the light source position and the measured wavelength. As the position of the source is changed we see a peak in the received power at the experiment centerline with the power falling off rapidly as the light source is moved off center. Looking at increasing wavelengths, we see an increase in the power received from 400 nm through 700 nm. At 700 nm there is a large jump in the power received. followed by a steady increase to the received power maximum at 900 nm. Beyond 1000 nm the power received falls off rapidly.

The jump in received power at 700 nm is a factor of two effects: the second CVF section is physically thinner and therefore has a higher transmission. it also has a steeper wavelength gradient and each reading will have a wider bandwidth. The rapid decrease in received power beyond 1000 nm is a combined factor of the lamp emitting less in this spectral region and approaching the effective range of the silicon detector. Figure nfovch2r shows the corresponding graph for the parallel polarization channel (2). Features of the parallel polarization are similar to the radiance channel. except the power received is approximately half that of the radiance channel.

The field of view is determined by finding the two positions where the received power is $\frac{1}{2}$ the maximum. The width between these two positions and the distance between the light source and the SSP are then used to calculate the viewing angle. To automate the process. the data were first normalized as shown in Figure ch3nor for the radiance channel. Note how the constant distant

lines roll over the top of the curve at the near infra red wavelengths. This is due to the longer wavelength light being 'bent' as is passes through the optics. In effect the SSP looks in slightly different direction at the longer wavelengths.

The data for each wavelength are now fit to a gaussian curve of the form:

3.2Cosine Response of Diffuser

The object of this exercise is to measure how the transmission of the flashed opal diffuser in channel 1 varies as a function of the incident angle of incoming radiation. Flashed opal is the only commercially available material that allows the transmission of radiation from any angle. The diffuser is made by bonding a thin layer of diffusing glass to a supporting clear glass substrate. The diffusing glass causes multiple scattering of light. By nature, the shorter wavelengths scatter more. which also means transmission losses are greater. Flashed opal diffusers work well through visible wavelengths and the transmission curve is close to that shown in Figure opal, however, at longer wavelengths a directed component is superimposed at the forward direction. Part of this exercise is to define the extent of this forward transmission lobe.

A schematic of the diffuser response setup is shown in Figure cosset. Setup is similar to that for the narrow field of view exercise. however. the distance between the SSP and the light source is only 53.3 cm. The lamp was calibrated by Eppley Labs at a distance of 50 cm, they recommend use of the lamp only for distances between the lamp and detector in excess of 45 cm. The SSP was set as close as it could be to the lamp and still have room for the screens to reduce reflections. Once the SSP and light source were aligned, the SSP was rotated and the received intensity was measured as the angle between the SSP and light source was varied. The procedure used is described in detail in Appendix B.

Results of the measured intensity versus the incident angle are shown in Figure cosraw. Data were not recorded when angles exceeded 80° because the front of the SSP vacuum chamber blocked all light from reaching the diffuser lens. In general, power increases as the source angle is decreased to 0. From 400 nm through 800 nm there is a gradual increase, although the received power is

so low it is difficult to see. From 800 nm through 1100 nm there is an extreme increase in power received at angles less than 3°. this is the strong forward transmission lobe mentioned previously. The maximum power received is shifted slightly to 1000 nm instead of 900 nm. Beyond 1100 nm the signal falls off sharply as this is beyond the range of the silicon detector.

To further explore how the flashed opal diffuser transmits radiation, the data were normalized so the maximum signal received is equal to unity as shown in Figure cosnor. Three distinct areas of diffuser transmission are evident. From 500 nm through 750 nm the transmission curve is roughly a cosine curve. However, between 500 and 600 nm the received signal is weak enough that instrument noise distorts the curve. Below 500 nm, the data were to noisy too define a curve. From 850 nm through 1100 nm the transmission curve has a very strong peak between 0° and 2°. At 1000 nm the power received drops to less than 85% of the maximum by 3°. Between 750 nm and 850 nm there is a rapid transition from a cosine transmission curve to a curve with the strong forward transmission lobe.

The forward transmission lobe was removed by normalizing the data between 3° and 80° to unity as shown in Figure cosnor3. Even at the longer wavelengths, the transmission curve approximates a cosine curve once the forward transmission lobe is removed.

To allow the calculation of diffuse light, a formula for the transmission curve is needed. For this purpose a curve of the form:

$$\frac{ReceivedPower(\theta)}{ReceiverPower(\theta = 0)} = a\theta^2 + b\theta + c + d(exp[-e\theta])$$

where the parameters $a, b, c, d,$ and e are all adjusted to fit the data. The first three terms of the right hand side will approximate the cosine transmission curve. The exponential term accounts for the forward transmission lobe. The parameter e is adjusted to cut off the effects of the forward transmission lobe at the proper angle. Figure cosfit shows an example curve fit for both 521 nm and 918 nm. The parameters for all the diffuse wavelengthsare tabulated in Appendix C.

4.Intrument Calibration

The instrument has undergone extensive calibration both at the Sandia National Laboratory (SNL) and the Los Alamos National Laboratory (LANL) Optical and Infrared Laboratory. This Laboratory provides calibration services to the ARM/UAV program as well as participates in other programs (add LANL homepage address).

Radiance Calibration

A 12 inch Labsphere integrating sphere was used to calibrate the spectral radiance channels of the SSP. The sphere is tracable to a NIST standard. The proceedure involved placing the sensor a short distance (say 1 meter) from the sphere. The distance is unimportant as long as the field of view (FOV) is within the aperature of the sphere and there is no stray light entering the instrument from sources other than the spehere. Data for a given channel is averaged for 5 minutes which is about 500 spectral scans of the instrument at all the gain settings. The sensor response is then obtained by equating the sesenor output to the known radiance output of the sphere I_λ (e.g. see refs here). The instrument response is thus

$$C = \frac{V}{I_\lambda(1)}$$

which has units of $Vm2srmicronW^{-1}$ where V is the voltage output of the intrument.

Temperature procedure ...

Figure xa presents the calibration factors C as a function of wavelength for a number of temperatures. Figure xb presents the spectra of C obtained from this procedure carried out over the course of 2 years (1995 - 1996). The folllowing remarks are offered in relation to the results shown. Firstly the dectector has a very small temperature response especially in the region between 0.4 μm and 0.75 μm. Furthermore, the instrument over these two years remained stable with C varying by no more than xof the sensor in the nir was less with C varying by y

Flux Calibration

Two different approaches were used to calibrate the flux channel of the instrument. In the first approach carried by LANL. the SSP was mounted on a rotary stage and illuminated by a

standard 1000W NIST lamp. The instrument was rotated in the five degree steps to 65 degrees with respect to the instrument axis and was in one degree steps to 90 degrees. Several minutes of data were taken at each angular position. before rotating to the next position. At each angle θ_i, the calibration factor $c_{\lambda,i}$ is obtained by

$$V_{\lambda,i} = c_{\lambda,i} F_{\lambda,i} cos\theta_i \tag{2}$$

where F_λ is the known spectral flux from the lamp. We obtain a single calibration coefficient by summation of all observations at all angles, namely

$$\bar{c_\lambda} = \frac{\sum_i \frac{V_{\lambda,i}}{F_{\lambda,i} \cos\theta_i}}{\sum_i \cos\theta_i} \tag{3}$$

For an instrument that obeys a perfect cosine response, then

$$\bar{c_\lambda} = c_{\lambda,i} \quad i \tag{4}$$

However. the angular response of the flux channel deviates from the cosine response especially when $\theta_i 70^o$ inwhich case $\bar{c_\lambda}$ is now interpreted as a weighted coefficient.

Figure a shows the spectrum of the coefficient $\bar{c_\lambda}$ obtained using this procedure. Figure xb is the percentage change in c_λ for a range of temperatures (realtive to a temperaure of ..) to indicate the extent of the instrument response to temperature. Figure xa also shows the calibration of the flux cahnnel obtained from the calibration procedure carried out at SNL. This procedure involved placing the instrument in a 48 inch integrating sphere. The advantage of this appraoach over that described above is that the radiance field incident on the sensor is isotropic and small mislalignements of the sensor do not affect the calibration. The flux F_λ illuminating the instrument is known and the calibration factor then becomes

$$c_\lambda = \frac{V_\lambda}{F_\lambda} \tag{5}$$

The calibration factors shown on Fig. xa present the closeness of both calibration proceedures in the visible portion of the instrument (up to about 0.75 mum with a deviation between the two

approaches that grow as the wavelength increases from that point. The calibration implemented in data analysis is the SNL calibration since the SSP exhibits hot spots in the forward direction (refer Fig. xx) at these longer wavelengths making calibration sensitive to slight errors in the lamp-instrument alignment (discussed below). These undesirable features of the diffusing optics also means that the accuracy of the calibration estimated below in principle can only be taken relative to the isotropic light source of the integrating sphere. Thus uncertainties will be introduced as the light source geometry varies from isotropy as it does in the real atmosphere. However, comparisons with other instruments of different optical design and different cosine characteristics suggests that this uncertainty is relatively small.

Estimation of Calibration accuracy

There are a number of sources of calibration error. For the sake of discussion. consider () from which we can write the uncertainty of c_λ as

$$\partial c_\lambda{}^2 = \sum_i \frac{\delta c_\lambda}{k_{\lambda,i}}{}^2 (\partial k_{\lambda,i})^2 + \sum_i \frac{\delta c_\lambda}{\theta_i}{}^2 (\partial \theta_i)^2 + \sum_i \frac{\delta c_\lambda}{T}{}^2 (\partial T)^2 \tag{6}$$

where $\partial k_{\lambda,i}$ represent the calibration source errors. instrument noise and error in wavelength assignment. The second term of (6) reprenets error in the angular position of lamp relative to instrument (this factor disappears in the SNL flux calibration) and the thrid factor includes errors associated with improper account of temperature response of the instrument.

Comparison with the TDDR

The calibration accuracies quoted above for the flux channel are only strictly relevant for isotropic sources of light. In the applications described in the following section . the instrument was mounted on an aircraft and pointed downwards to measure reflected radiances and fluxes. Measurements were made in this fashion during a series of flights conducted as part of experiemnts carried out in the period from 1995-1997. The .... also flew on the same research aircraft along with the SSP during these experiments. Although details of the experiments are given below. it is worth mentioning that the scenes viewed by both sets of instruments varied from thick overcast clouds to

broken clouds. to thin cirrus to clearsky views of fields surrounding the Oklahoma CART site (ref here). These scenes provide a variety of different radiance configurations and thus a comparison between the two instruments provides a way of assessing the likely uncertainty that can be ascribed to the calibration of the SSP.

Results